



## Magnetic Sensing with Large Ensembles of Nitrogen-Vacancy Centers in Diamond

Clement, Joshua David

*Publication date:*  
2022

*Document Version*  
Publisher's PDF, also known as Version of record

[Link back to DTU Orbit](#)

*Citation (APA):*  
Clement, J. D. (2022). *Magnetic Sensing with Large Ensembles of Nitrogen-Vacancy Centers in Diamond*. Department of Physics, Technical University of Denmark.

---

### General rights

Copyright and moral rights for the publications made accessible in the public portal are retained by the authors and/or other copyright owners and it is a condition of accessing publications that users recognise and abide by the legal requirements associated with these rights.

- Users may download and print one copy of any publication from the public portal for the purpose of private study or research.
- You may not further distribute the material or use it for any profit-making activity or commercial gain
- You may freely distribute the URL identifying the publication in the public portal

If you believe that this document breaches copyright please contact us providing details, and we will remove access to the work immediately and investigate your claim.

Doctor of Philosophy  
Doctoral thesis in Physics

DTU Physics  
Department of Physics

---

# **Magnetic Sensing with Large Ensembles of Nitrogen-Vacancy Centers in Diamond**

Joshua Clement



**Supervisor:** Professor Ulrik Lund Andersen

**Co-supervisors:** Associate Professor Alexander Huck & Associate Professor Kirstine Berg-Sørensen

DTU Fysik  
Department of Physics  
Technical University of Denmark  
Fysikvej 307  
2800 Kongens Lyngby, Denmark

# Summary

---

Nitrogen-vacancy (NV) centers are crystal defects in diamond which, even unshielded at room temperature, are highly sensitive to magnetic fields. The biocompatibility of diamond makes for promising applications in biophysics, where nerve signals can be sensed and imaged at close range.

In this work, a practical, compact magnetic sensing device is presented, which contains the key elements of an NV sensor in a box that fits in the palm of one's hand.

Then, in exploration of the limits of its sensitivity, improvements are demonstrated with two approaches. First, optimal control methods are used to better manipulate the quantum spin state of diverse NV centers. Then laser beam shaping is used to improve the measurement of their spin states by the fluorescence they emit. These results indicate a promising approach for heightened sensitivity of future NV-based devices.



# Resumé

---

Nitrogen-vakance (NV) centre er defekter i diamant, der er meget følsomme til magnetfeltet, selv ved stuetemperatur. Da diamant er en hård, ugiftig materiale, findes der mange anvendelser i biofysik, hvor f.eks. nerve signaler kan måles.

I denne afhandling er en praktisk, kompakt magnetometer presenteret. Den indeholder de vigtige elementer af en NV sensor i en beholder der kan sidde i ens håndflade.

Næste, for at øge følsomheden i sådanne NV magnetometre, er der implementeret to fremgangsmåder. For det første er optimal kontrol metoder brugt til at bedre manipulere det kvante spin af diverse NV centre. For den anden er laser beam omformning brugt til at forbedre aflæsning af NV centrenes spin via deres fluorescens. Disse resultater indikerer en vej til dybere følsomhed af fremtidige NV-baseret anordninger.



# Acknowledgements

---

I'm thankful to Alex and Kirstine for answering my stupid questions and guiding me through these years.

Thanks to Ulrik for holding this crazy group together and tolerating when I forgot our meetings.

Oh, thanks also to Alex and Kirstine for tolerating when I forgot our other meetings.

Thanks to Jim for being interested in my production of scientific results.

Thanks to Luca for working hard enough to do a better PhD project than me.

Thanks to Andreas for actually understanding how this magnetometry business works.

I'm thankful to Leo for the great film recommendations.

Thanks, Marcus, David and Kasper for being pretty good students.

I'm thankful to all the interesting characters who make up the QPIT social fabric and made it such a joy to be back when COVID ended.

Thanks, Jens, for fighting to keep the fridge clean,  
and Maxime, for fighting to keep it full.

Thanks, Anna, for being horrified by my opinions but being nice to me anyway.

Thanks in advance for the cake, Theresa. I hope it's good.

There are too many to list by name, but you know who you are, and I'm sure you'll all make it, Angelo.

I'm still thankful to those of you who passed through QPIT before COVID, even though that was ages ago.

Thanks especially to Christian for not moving to Roskilde yet. Please never do.

Thanks, Erika, for getting people to talk at lunch.

Thanks, Sepehr, for paving the way.

I'm thankful to all my friends here for making Copenhagen my home.

Thanks, Peter, for grade A moral support.

I guess those of you who don't live here didn't help much, but I'm grateful anyway, and I miss you all.

Thanks, Ella, for being worth my time.



# Abbreviations

---

<b>AC</b>	Alternating Current
<b>AOM</b>	Acousto-optic modulator
<b>BS</b>	Beam-splitter
<b>CMR</b>	Common Mode Rejection
<b>DC</b>	Direct Current
<b>HWP</b>	Half-Wave Plate
<b>IQ</b>	In phase- / Quadrature- (modulation)
<b>MW</b>	Microwave
<b>NMR</b>	Nuclear Magnetic Resonance
<b>NV</b>	Nitrogen Vacancy
<b>PBS</b>	Polarizing Beam-splitter
<b>SNR</b>	Signal:Noise Ratio
<b>TEM</b>	Transverse Electric Magnetic
<b>ZFS</b>	Zero-Field Splitting



# Contents

---

<b>Summary</b>	<b>i</b>
<b>Resumé</b>	<b>iii</b>
<b>Acknowledgements</b>	<b>v</b>
<b>Abbreviations</b>	<b>vii</b>
<b>Contents</b>	<b>ix</b>
<b>Introduction</b>	<b>1</b>
0.1 Magnetic Sensing . . . . .	1
0.2 NV centers . . . . .	1
0.3 Thesis overview . . . . .	1
<b>I Background concepts</b>	<b>3</b>
<b>1 NV center properties</b>	<b>5</b>
1.1 Diamond . . . . .	5
1.2 Electronic structure . . . . .	6
1.3 Optically detected magnetic resonance . . . . .	7
<b>2 Coherent control</b>	<b>9</b>
2.1 Rabi oscillations . . . . .	10
2.2 Coherence times . . . . .	11
2.3 Experimental implementation . . . . .	12
2.4 Common control sequences . . . . .	12
<b>3 Magnetic sensing</b>	<b>15</b>
3.0.1 Continuous wave and pulsed measurement schemes . . . . .	15
3.0.2 Lock-in detection . . . . .	15
3.1 Sensitivity . . . . .	16

---

3.1.1	Shot noise . . . . .	16
3.1.2	Time scaling . . . . .	17
3.1.3	Common sensitivity definitions . . . . .	17
3.2	Laboratory implementation . . . . .	18
3.2.1	Optical excitation . . . . .	18
3.2.2	Laser beam shape . . . . .	18
3.2.3	Bias magnetic field . . . . .	19
<b>II</b>	<b>Experimental results</b>	<b>21</b>
<b>4</b>	<b>Compact NV Magnetometry</b>	<b>23</b>
4.1	Background . . . . .	23
4.2	Article . . . . .	24
<b>5</b>	<b>Optimal control of an NV ensemble</b>	<b>31</b>
5.1	Background . . . . .	31
5.2	Article . . . . .	32
5.3	Supplementary Information . . . . .	48
5.4	Revision . . . . .	64
<b>6</b>	<b>Beam shaping</b>	<b>65</b>
6.1	Background . . . . .	65
6.2	Article . . . . .	65
6.3	Supplementary Information . . . . .	74
	<b>Conclusion</b>	<b>81</b>
	<b>Appendices</b>	<b>83</b>
	<b>Appendix A Rabi oscillation animation</b>	<b>85</b>
	<b>Bibliography</b>	<b>87</b>

# Introduction

---

## 0.1 Magnetic Sensing

Wherever electric charge moves, magnetic fields are created. This occurs in familiar cases, like Earth's magnetic field created by currents of molten iron in its core, or in bar magnets via the alignment of the quantum motion of electrons and nuclei. But electric charge moves in all sorts of processes from the exotic flows of space plasma to the intimate muscular contractions of our hearts.

There are many niches for magnetism in modern technology, such as data storage in hard disk drives, but the area which most directly motivates this work is in medical imaging and diagnostics.

## 0.2 NV centers

Nitrogen Vacancy centers in diamond consist of a substitutional nitrogen atom and a lattice vacancy inside the carbon lattice of a diamond, as shown in Fig. 0.1. NV centers can be addressed by light and resonant microwaves to sense ambient magnetic fields as well as other environmental conditions. They are the workhorse of this project.

## 0.3 Thesis overview

This work is structured around three articles representing the main results of the project presented in Part II. In the first, a compact magnetometry setup was developed, with an aim to be used in the real-life settings that motivate the study of NV center magnetometry for biophysics and medical use. In the compact setup, we used continuous-wave magnetometry techniques, which are theoretically less sensitive than pulsed magnetometry techniques, but are nevertheless used for record-setting measurements with large ensembles of NV centers. The remainder of the project was aimed at alleviating the limitations of pulsed magnetometry for setups like our compact magnetometer which rely on addressing a large ensemble of NV centers. The second article focuses on the use of optimal control methods to improve the uniformity of the effect of the microwave pulses used to manipulate the spin states of many

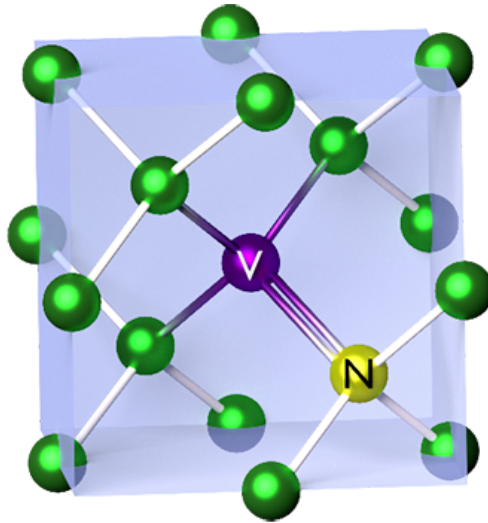


**Figure 0.1.** Nitrogen Vacancy center shown inside diamond lattice. Image from NIST, Public Domain, via Wikimedia Commons

diverse NV centers throughout the ensemble. The third article considers how the inhomogeneity of the laser beam used to address the ensemble impacts the sensitivity of the spin readout process. In all, substantial improvements in sensitivity with pulsed magnetometry schemes were measured by using the techniques explored in the second and third articles, which can be of use in a next iteration of an applied magnetometry device. Part I contains the background information that should contextualize the main results and serve as a useful reference while reading Part II.

# Part I

## Background concepts



# CHAPTER 1

## NV center properties

---

### 1.1 Diamond

Diamond, the host material for the nitrogen-vacancy center, consists of a crystal lattice of carbon atoms. It is very hard, nontoxic, thermally conductive, and transparent. It has an index of refraction of 2.417 for visible light.

Diamonds used in laboratory settings are typically synthetic and made through either high pressure high temperature (HPHT) fabrication or chemical vapor deposition (CVD). CVD allows for finer control of the diamond's composition of isotopes and impurity doping, and is therefore more commonly used in the field of quantum sensing [1]. The diamonds used in the work presented here were both synthesized by CVD. Briefly stated, the technique of CVD is to heat a plasma of carbon atoms and other gases over a substrate onto which the carbon binds in a diamond lattice.

The crystallographic structure of diamond (depicted in Fig. 0.1) has four axes along which any two nearest neighbors in the lattice can be separated. The vector from the nitrogen towards the vacancy determines the NV center's axis about which it has  $C_{3v}$  symmetry. It is the projection of environmental magnetic fields along the NV axis to which an NV center is sensitive. Under conventional irradiation and annealing techniques, the axes of the created NV centers are randomly distributed between the four diamond crystallographic axes with equal probability. The vector magnetic field can be sensed by using NV centers in all four crystallographic orientations simultaneously [2], though typically only those aligned along one axis are used for ensemble sensing [3].

The most common carbon isotope is  $^{12}\text{C}$ , representing 99% of carbon atoms.  $^{13}\text{C}$  make up most of the remaining 1%. Diamonds can be synthesized via CVD from isotopically purified  $\text{CO}_2$ , and otherwise have roughly 1% of the lattice made of  $^{13}\text{C}$  atoms. This is relevant for magnetometry because, unlike the spinless  $^{12}\text{C}$ ,  $^{13}\text{C}$  have a spin of  $\frac{1}{2}$  which can add noise by magnetic coupling to the NV center spin [4, 5].

The density of NV centers in diamond is usually given in parts-per-billion/million (ppb/ppm), as in per C atom in the diamond lattice. 1 ppb is equal to  $176\ \mu\text{m}^{-3}$  at room temperature. Low concentrations of NV centers  $< 10$  ppb can be made during CVD by introducing  $\text{N}_2$  during growth [1]. This also creates nitrogen defects in the diamond, roughly  $100\times$  as many as NV centers, and it is the deleterious effects of too much nitrogen on the growth of the diamond crystal that limits the possible density.

After diamond synthesis, nitrogen defects can be converted into NV centers by first creating lattice vacancies through high energy electron or ion irradiation, and then annealing the diamond at high temperature to let the vacancies diffuse and associate to the nitrogen. In this way,  $\sim 1$  ppm of NV centers has been demonstrated in a CVD diamond [6].

## 1.2 Electronic structure

The negatively charged NV center,  $\text{NV}^-$ , has six electrons forming a spin  $S = 1$  system [7]. It has a  ${}^3\text{A}_2$  ground state triplet with an allowed spin-conserving 1.945 eV optical transition to a  ${}^3\text{E}$  excited state triplet [8]. Typically, and exclusively in this work, this transition is driven by an off resonant 532 nm (green) optical field. The  ${}^3\text{E}$  state can decay radiatively to the  ${}^3\text{A}_2$  state [9] with zero-phonon emission [10], which perfectly matches the transition energy, at 638 nm (red) [11]. Typically this decay has a broad fluorescence spectrum due to phonon-assisted decay paths for mostly longer-wavelength photon emission. Two other states are permitted for the  $\text{NV}^-$ : the  ${}^1\text{A}_1$  and the  ${}^1\text{E}$  singlets [12], which together form an alternate decay path from  ${}^3\text{E}$  back to  ${}^3\text{A}_2$ , shown in Fig. 1.1. The  ${}^1\text{E}$  state is metastable, with a lifetime much longer than the other excited states [13]. Because the  ${}^1\text{A}_1$  and  ${}^1\text{E}$  states are not spin  $S = 1$  multiplets, the spin is not conserved in the  ${}^3\text{E} \rightarrow {}^1\text{A}_1 \rightarrow {}^1\text{E} \rightarrow {}^3\text{A}_2$  decay path [13, 14].

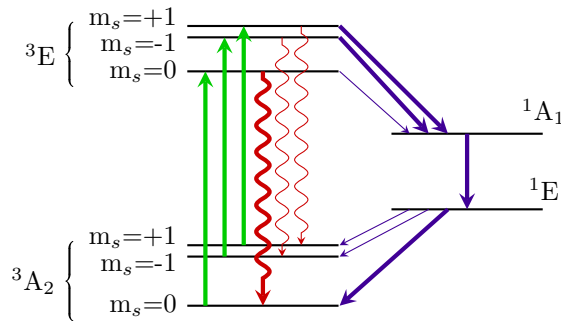


**Figure 1.1.**  $\text{NV}^-$  level diagram with labeled transitions. Green arrows are spin-conserving excitation by absorption of a green photon. Red arrows are spin-conserving decay with emission of a red photon. Purple arrows are non-spin-conserving decays which do not radiate visible light, where a thicker line indicates a relatively faster decay rate.

The neutral charge state  $\text{NV}^0$  has only five electrons, and the resulting allowed electron configurations are not magnetically sensitive [7]. Transitions are possible between the  $\text{NV}^0$  and  $\text{NV}^-$  when e.g. a green photon is absorbed from the optical excited state ( ${}^3\text{E}$  for the  $\text{NV}^-$ ), and an electron is excited into the conduction band of the diamond, from which it can rejoin with a nearby charge donor, such as a nitrogen defect [15].

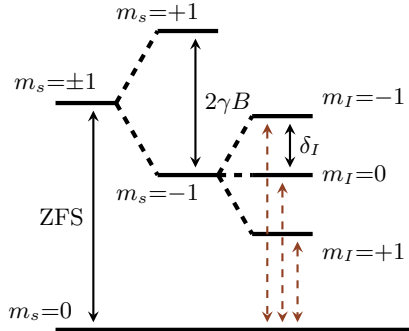


**Figure 1.2.** Level diagram of the splitting in the  $\text{NV}^- \ ^3\text{A}_2$  multiplet including the Zeeman effect and  $^{14}\text{N}$  hyperfine splitting. The brown dashed lines show the available MW transitions between the  $m_s=0$  and  $m_s=-1$  states addressed experimentally in this work.

The finer structure of the  $^3\text{A}_2$  multiplet is shown in Fig. 1.2. There is a temperature- [16,17] and pressure-dependent [18] zero field splitting (ZFS) of  $\approx 2.88 \text{ GHz} + 77 \text{ kHz/K} + 15 \text{ Hz/kPa}$  due to lattice strain, which raises the energy of the  $m_s=\pm 1$  spin states aligned along the NV crystallographic axes. The Zeeman effect raises/lowers the energy of electron spin aligned with/against a magnetic field, which splits the  $m_s=\pm 1$  levels [19]. The adjustment in energy follows from the electron gyromagnetic ratio  $\gamma = 28 \text{ GHz/T}$ , which for the  $\sim 3 \text{ mT}$  bias magnetic field used in this work corresponds to  $\sim 90 \text{ MHz}$ . The nitrogen nucleus has a  $S = 1$  or  $S = \frac{1}{2}$  spin for the  $^{14}\text{N}$  and  $^{15}\text{N}$  isotope respectively, which creates a local magnetic field in the vicinity of the NV electron, affecting its energy level [7]. For the more common  $^{14}\text{N}$  isotope in the diamonds used in this work, the hyperfine splitting by which the nuclear spin adjusts the NV electron energy is  $\delta_I = 2.16 \text{ MHz}$  [20].

### 1.3 Optically detected magnetic resonance

The ability to use NV centers as quantum sensing devices relies on the ability to translate the frequency difference between the  $m_s=\pm 1$  and  $m_s=0$  states, which depends on external parameters including the magnetic field, into a legible signal. When the spin is encoded into the optical signal of the NV centers' fluorescence to sense the magnetic field, the technique is called optically detected magnetic resonance (ODMR) [21].

The electron spin is converted into a fluorescence signal via the spin-selective decay through the singlet states  $^1\text{A}_1$  and  $^1\text{E}$ , which happens with about 15% probability for the  $m_s=0$  state and about 55% probability for the  $m_s=\pm 1$  states of the  $^3\text{E}$  excited state [13]. Because the optical excitation and radiative decay between the  $^3\text{A}_2$  and  $^3\text{E}$  states are spin conserving, we use the “ $m_s=0$  state” to refer to both the  $m_s=0$  state of the  $^3\text{A}_2$  and of the  $^3\text{E}$ . The  $m_s=0$  is the bright spin state and the  $m_s=\pm 1$

are the dark spin states, because the latter are less likely to emit a red photon after optical excitation.

In addition to being detectably darker, the  $m_s = \pm 1$  states have a greater propensity to non-spin-conserving decay via the singlet states [22], which polarizes the NV centers into the  $m_s = 0$  state. Every time the NV center electron decays through the singlet states, it gets a random new spin with somewhat higher probability of being  $m_s = 0$ , and the  $m_s = \pm 1$  states take that chance more often. Therefore, if the NV center is only driven optically, it reaches an equilibrium  $\sim 80\%$  polarization into  $m_s = 0$  [12, 14].

A resonant (i.e. frequency-matched) microwave (MW) control field can be used to drive the transition between the  $m_s = 0$  and  $m_s = \pm 1$  states [19]. There is some contrast between the fluorescence signal measured with or without a given MW control field, and this ODMR contrast is greater the better tuned the field is to the transition frequency [23]. There are many different protocols for applying MW control fields and reading out the spin, which will be elaborated in the next chapter. Here, it suffices to grasp that in all ODMR protocols, the fluorescence contrast indicates the detuning of the MW control field from the  $m_s = 0 \leftrightarrow m_s = \pm 1$  transition frequency, which is a function of the magnetic field.

## CHAPTER 2

# Coherent control

---

The ability to transfer population from the  $m_s=0$  state to the  $m_s=\pm 1$  states for performing ODMR is one specific case of the general ability to coherently control the quantum spin state in the  ${}^3A_2$  multiplet. When the spin is measured, the result must be in one of the three allowed  $m_s=\{-1,0,1\}$  levels, but between measurements, the spin state can be in a superposition of multiple levels. Commonly in NV sensing and exclusively in this work, only one of the  $m_s=\pm 1$  states is addressed, leaving a two-level system of, in our case, the  $m_s=0$  and  $m_s=-1$  states.

The quantum state of a two-level system is more than a distribution of probability between the two levels, say a 40% chance of having  $m_s=0$  spin and a 60% chance of having  $m_s=-1$  spin. It also contains a relative phase between the two levels. The full information of the state can be represented geometrically as a vector pointing somewhere on the surface of a Bloch sphere as shown in Fig. 2.1, where the value along the  $\hat{z}$  direction is the population in one or the other level, and the azimuthal angle is the quantum phase [24, 25].

As the system evolves, the quantum phase advances with the frequency that corresponds to the energy between the two levels; the vector precesses around the  $\hat{z}$  axis of the Bloch sphere at the transition frequency. Under the influence of the MW control field, the spin state vector is pushed counterclockwise about the direction the MW field's magnetic component points. The MW field's magnetic component oscillates along its axis at the frequency of the MW drive. If the MW drive frequency matches the transition frequency, then it will stay in sync with the spin state's precession and continue to rotate it in the same direction period after period as it oscillates. In such a case, the MW control field is resonant with the two-level system.

Coherent control allows for arbitrary rotation operations on the Bloch sphere via the adjustments accumulated period after period of the resonant control field's oscillation in a discrete control pulse. When describing the effect of a control pulse, a rotating frame can be used as the coordinate system on the Bloch sphere, where the  $\hat{x}$  and  $\hat{y}$  axes of the Bloch sphere rotate around with the frequency of the MW drive. If the MW pulse is in phase with the rotating frame (that is, if the timing of where it is in its oscillatory cycle matches the arbitrarily defined starting point), then it rotates the spin state vector about the  $\hat{x}$  axis, and if it is delayed or advanced by  $90^\circ$  (a quarter of an oscillatory period), it rotates the spin state vector about the  $\hat{y}$  axis on the Bloch sphere. In-phase/quadrature (IQ) modulation is a way of neatly shaping a MW control pulse according to these rotation operations about  $\hat{x}$  and  $\hat{y}$ . Where

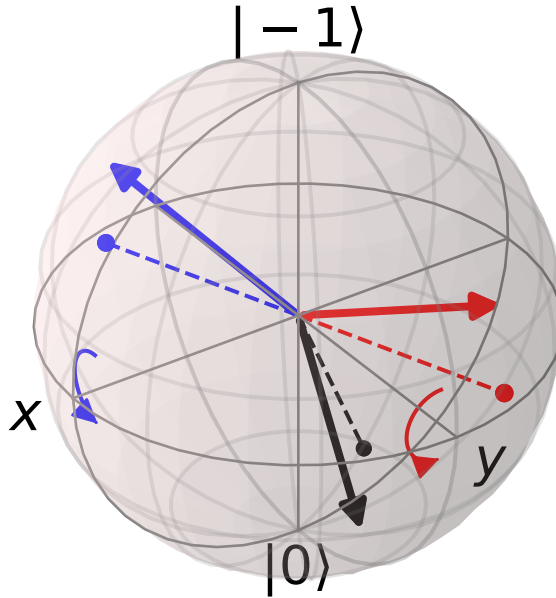


**Figure 2.1.** Bloch sphere of the  $m_s=0$  and  $m_s=-1$  two-level system with an example state shown in black and its projection onto the transverse plane shown by the black dashed line. The results of  $\pi$  rotations of the example state about the  $x$  and  $y$  axes in the rotating frame of reference are shown in blue and red.

the MW pulse is fully described by the in-phase amplitude  $I(t)$  and the quadrature amplitude  $Q(t)$  that are proportional to the rate of rotation about the  $\hat{x}$  and  $\hat{y}$  at each moment in time  $t$  [26].

## 2.1 Rabi oscillations

If a resonant MW pulse with constant amplitude and phase is applied, it will rotate the spin state on the Bloch sphere about an axis on the transverse plane from pole to pole on the Bloch sphere. This corresponds to oscillations in the  $m_s=0$  and  $m_s=-1$  state populations, known as Rabi oscillations. The Rabi frequency  $\Omega$  is the rate of these oscillations, or how fast the spin state is driven around the Bloch sphere, and it is quadratic with the applied MW power. [24]

If the frequency of the MW drive  $f_{\text{MW}}$  does not match the transition frequency of the NV center spin  $f_{\text{NV}}$ , then they drift out of sync during the application of a MW control pulse. In the rotating frame of the Bloch sphere, this is described as the spin state precessing at the frequency detuning  $\Delta = f_{\text{NV}} - f_{\text{MW}}$ . If the spin state begins

polarized in the  $m_s=0$  direction on the Bloch sphere, it cannot be rotated all the way to  $m_s=-1$  by an off-resonant MW pulse of constant phase and amplitude, because once it precesses out of phase with the MW drive, it is pushed in the wrong direction, following a smaller circle around the Bloch sphere and returning to  $m_s=0$  sooner than otherwise. The Rabi frequency  $\Omega$  is therefore faster for  $\Delta \neq 0$ , not because the MW pulse drives the spin state faster around the Bloch sphere, but because the path around the Bloch sphere is shorter. My animated illustration can be found via Appendix A.

## 2.2 Coherence times

The NV center spin state, like quantum systems in general, cannot be manipulated indefinitely. The quantum coherence (the property of there being a phase between level populations rather than merely a statistical mixture) decays over time. The decay is characterized by three different durations  $T_1$ ,  $T_2$  and  $T_2^*$  which correspond to the rates of different decay mechanisms.

The decay time  $T_1$  describes thermal relaxation, where the longitudinal component (along the  $\hat{z}$  axis) of the state on the Bloch sphere decays towards 0 [27, 28]. This is the result of decay towards thermal equilibrium via a net gain/loss of energy with the surrounding lattice. Generally this is by far the slowest decay mechanism, though  $T_2$  can be comparable in extreme cases [29, 30].

The decay time  $T_2$  characterizes the irreversible decay of the transverse component (the magnitude perpendicular to  $\hat{z}$ ) of the spin state, also called dephasing [21]. In this decay process, there is no change in energy; instead the system “loses track” of how much phase accumulated since initialization due to interaction with extraneous spins. The erasure of phase information is a decay towards an even probability distribution through the range  $[0, 2\pi]$ , in which case there is no net transverse component.

Closely related to the dephasing process characterized by  $T_2$  is the bulk field dephasing characterized by  $T_2^*$ . An ensemble of NV centers spread throughout a volume has an inhomogeneous transition frequency due to any inhomogeneities in the magnetic field or strain in the diamond. The ensemble gets out of sync as each individual NV center spin precesses at its own transition frequency, and this causes a decay of the net transverse component of the ensemble-averaged spin state.  $T_2^*$  is the characteristic time of the decay of the total ensemble-averaged spin state, from a combination of this effect and the  $T_2$  relaxation [31]. For the low frequency sensing with large ensembles that is the focus of this work,  $T_2^*$  is the limiting coherence time.

Typical values of the coherence times are on the order of  $\sim$ ms for  $T_1$ , 0.1-10 $\mu$ s for  $T_2^*$ , and roughly  $\sim 10\times$  larger for  $T_2$  than  $T_2^*$  [31], up to a record  $T_2 \approx 2.4$  ms [32], depending on the presence of  $^{13}\text{C}$  and other crystal defects in the diamond.

## 2.3 Experimental implementation

Coherent control allows for rotation operations to be applied to the spin, i.e. to transform initial spin states into final spin states by a user-selected function. It does not allow for an arbitrary spin state to be selected; without initial spin polarization in a given direction, it cannot produce a final spin state polarized in a new chosen direction. The spin state can be initialized with  $\sim 80\%$  polarization (as we show in Chapter 5) into  $m_s=0$  by application of an optical excitation laser pulse via the selective decay mechanism discussed in Section 1.2. In this work, and with few exceptions in NV magnetometry, the laser beam is blocked during application of MW control pulses so that the state can be manipulated without interruption by optical excitation (see [33] for a rare counterexample). After the MW control pulse sequence is complete, the projection of the final spin state onto the  $\hat{z}$  axis of the Bloch sphere (the probability of being in the  $m_s=0$  or  $m_s=\pm 1$  eigenstates) can be read out by applying another laser pulse and detecting the strength of the NV fluorescence. The general form of the sequence is shown in Fig. 2.2.

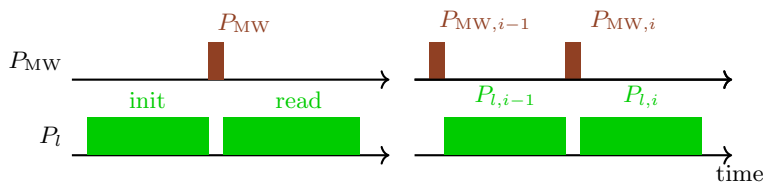


**Figure 2.2.** (left) example protocol for initialization, coherent control via the MW pulse, and spin state readout. (right) repeated control protocol, where the  $(i-1)^{\text{th}}$  readout pulse also serves as the  $i^{\text{th}}$  initialization.

The optical spin readout for an NV center is not deterministic [34]; it is necessary to repeat a spin readout measurement many times with identical state preparation (spin initialization and coherent control) in order to accumulate statistical information about the probability distribution of the spin state after the control sequence [35,36]. Because the spin readout and the initialization both rely on a laser pulse, repeated control sequences can use each optical excitation pulse for both purposes as shown in Fig. 2.2.

## 2.4 Common control sequences

A simple case of coherent control is pulsed ODMR [37], where the MW pulse sequence consists of a single  $\pi$ -pulse. When the pulse is perfectly resonant ( $\Delta = 0$ ), the  $\pi$ -pulse rotates the spin from the  $m_s=0$  to the  $m_s=\pm 1$  state, maximally reducing the NV center fluorescence. When off-resonant, the final spin state is farther from  $m_s=\pm 1$

the greater the detuning  $\Delta$  is, until the detuning is great enough that the MW control pulse has no effect. A pulsed ODMR spectrum is shown in Section 5.2 Fig 10.

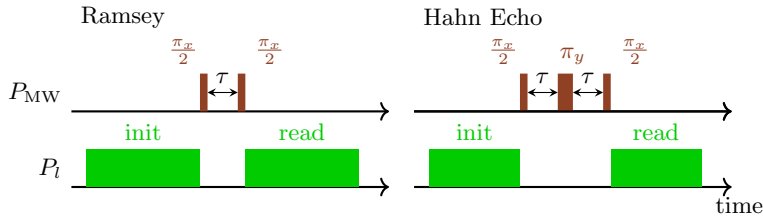


**Figure 2.3.** Illustrated Ramsey and Hahn echo measurement protocols.

The Ramsey sequence [38], shown in Fig. 2.3, has long been used in nuclear magnetic resonance (NMR) experiments and is applicable to low-frequency magnetic field sensing with NV centers [21, 39]. It begins with a pulse to rotate the spin state by  $\pi/2$  about the  $\hat{x}$  axis from  $m_s=0$  to the equator of the Bloch sphere. Then, the spin state precesses about the Bloch sphere in the rotating frame of the MW drive at the detuning frequency  $\Delta$  for a wait period  $\tau$ . Finally, a second  $\pi/2$  pulse rotates the spin state about the  $\hat{x}$  axis, projecting the amount of phase accumulated during the wait period ( $\Delta\tau$ ) onto the population along the  $\hat{z}$  direction. It is limited by the  $T_2^*$  coherence time because the NV centers with inhomogeneous  $\Delta$  precess at different rates and fall out of sync.

The Hahn echo sequence [40], shown in Fig. 2.3, is like the Ramsey sequence, but with the addition of a  $\pi$  rotation about the  $\hat{y}$  axis of the Bloch sphere half way through the waiting duration. The effect of this  $\pi$  pulse is to reverse the direction of precession, so that after an identical wait period  $\tau$  has elapsed, the fastest and slowest precessing NV center spins will have resynchronized [21]. It is therefore limited by the  $T_2$  coherence time instead of the shorter  $T_2^*$  [41]. However, the sequence is only sensitive to magnetic fields which reverse direction between the two waiting periods, i.e. high frequency AC fields [36]. Due to the fact that  $T_2 > T_2^*$ , AC measurements with Hahn- and other echo sequences are generally capable of greater sensitivity than DC measurements [42].



# CHAPTER 3

## Magnetic sensing

---

### 3.0.1 Continuous wave and pulsed measurement schemes

Pulsed ODMR [37], Ramsey magnetometry [39], and Hahn echo [42] sequences all require the ability to apply laser and MW pulses to the NV ensemble. This entails the use of a pulsed laser or an acousto-optic modulator (AOM) to switch a continuous wave (CW) laser, some fast hardware for MW switching, and likely some programmable hardware for generating modulation signals. Pulsed sensing also requires sufficient laser and MW intensity [43] to limit the measurement overhead (time spent not sensing during the measurement protocol), and as we explore in Chapters 5 and 6, sufficient homogeneity of control fields throughout the ensemble. Therefore, pulsed sequences have typically been limited to use in small ensembles or single-NV experiments.

NV ensemble magnetometry can also be performed with CW ODMR [20, 44–46], in which a laser beam is continually applied, and MW control fields drive the  $m_s=0 \rightarrow m_s=\pm 1$  transition during optical excitation. This approach suffers from broadening of the resonance linewidth [37, 47] which reduces the conversion of fluorescence into information about the magnetic field.

### 3.0.2 Lock-in detection

There is often a strong source of noise in the frequency range that a measurement needs to be taken. For example, the diode-pumped solid state lasers used to pump the NV centers in our measurements has substantial variations in power output in the frequency range  $< 100$  Hz. Because this overlaps with the frequency range of the signals we measure, it can be mixed up with the magnetic signal we are interested in. Lock-in detection is a method of shifting the frequency of a measurement into a less noisy region of the noise spectrum, i.e. where it can't be confused with the low frequency laser noise.

The technique consists of first modulating a parameter of the setup that correlates with the fluorescence signal (e.g. the MW amplitude or frequency, or the laser intensity) and then demodulating the detected signal by the same frequency. For example, in a CW ODMR scheme without lock-in detection, the voltage driving the antenna to produce the MW control field is  $V(t) = A \cos(\omega t)$  and the NV fluorescence signal

$S(t) = B(t)$  is linear with the low frequency magnetic field, ignoring noise. Now the MW field can be amplitude modulated by  $M(t) = 1 - \cos(2\pi ft)/2$ , so that  $V(t) = A \cos(\omega t)M(t)$ . The noiseless NV fluorescence signal is then  $S(t) = B(t)M(t)$ , so the part of the fluorescence signal which needs to be measured is also modulated at the frequency  $f$ . To demodulate the NV center fluorescence signal, it is multiplied by  $M(t)$ :

$$S_{\text{demod}}(t) = B(t)M(t)^2,$$

which is proportional to

$$S_{\text{demod}}(t) \propto B(t) \frac{1 + \cos(4\pi ft)}{2}.$$

With a low pass filter to remove the fast oscillating term,  $B(t)$  is recovered [20, 48].

This technique can be implemented in a hardware device, as in Chapter 4, or in software by digitally sampling  $S(t)$  and  $M(t)$ , as in Chapter 5.

## 3.1 Sensitivity

The signal:noise ratio (SNR) is a measure of how much a measured signal stands out from the uncorrelated noise in its measurement context. It is necessary to have a SNR of at least 1 to be able to detect that there is a signal at all. The sensitivity of a sensing device is defined as the magnitude of the signal for which there is a SNR of 1, i.e. the smallest possible to detect.

### 3.1.1 Shot noise

When the fluorescence of the NV centers is detected, it is turned into an electrical signal by a photodiode through absorption of discrete packets of optical energy, photons. There is no guarantee that photons are absorbed at a given rate; there is only a given probability per time for a single photon to be absorbed, and the noise that results from this probabilistic behavior is called shot noise. The shot noise of  $N$  discrete events (e.g. the absorption of  $N$  photons) has a standard deviation of  $\sqrt{N}$ .

Other sources of noise in a NV center magnetometry setup can often be ameliorated, for example by common mode rejection (CMR) of laser noise, lock-in detection to avoid low frequency thermal and mechanical noise, and higher-quality amplifiers and detectors to reduce electronic noise. Shot noise is fundamental to the detection of incoherent fluorescence from NV centers and cannot be reduced. It also increases with a larger fluorescence signal (with more photons  $N$  being collected per time), so in the regime of the large ensembles of NV centers used in this work, it is often the dominant source of noise. Achieving a shot noise-limited measurement means that sensitivity cannot be improved by further reducing other sources of noise.

### 3.1.2 Time scaling

The measurement context where the SNR is defined includes the bandwidth considered, where the contributing noise is integrated over the measured bandwidth. The consequence is that the noise can be decreased (and therefore the SNR increased) by restricting the measurement bandwidth. An intuitive example is the case of a DC (zero frequency) measurement. For a measurement taken in a finite amount of time  $t$ , there is a finite bandwidth from 0 Hz to  $\frac{1}{2t}$  Hz. The mean of the signal collected over a given duration includes less noise as the duration is extended because more low frequency noise is removed.

The noise term in the SNR is the standard deviation of the noise present, which for noise sources evenly distributed in frequency like shot noise, is proportional to the square root of the measurement's bandwidth. Because the bandwidth (or measurement duration) can be freely chosen and adjusted, sensitivity  $\eta$  is defined with a normalization over the bandwidth, in units of T/ $\sqrt{\text{Hz}}$  for measurements of the magnetic field. The reader should note that it would not be useful to measure for example the average magnetic field with very fine precision over the course of one year. The bandwidth of the measurement must match the bandwidth of the signal one wants to detect, and the sensitivity with that bandwidth must be below the signal's magnitude.

### 3.1.3 Common sensitivity definitions

The low frequency sensing protocol with the best per-NV center sensitivity scaling is Ramsey magnetometry, which has a shot noise limited sensitivity of

$$\eta \approx \frac{1}{\gamma C_R e^{-(\tau/T_2^*)} \sqrt{\mathcal{N}}} \frac{\sqrt{t_I + \tau + t_R}}{\tau}$$

for the electron gyromagnetic ratio  $\gamma$ , the readout contrast  $C_R$ , the wait period  $\tau$ , the dephasing time  $T_2^*$ , the photon count per readout  $\mathcal{N}$ , the readout duration  $t_R$  and the addition time for reinitializing the NV electron spin  $t_I$  [43]. Comparatively, the shot noise limited sensitivity of a CW ODMR scheme is

$$\eta \approx \frac{4}{3\sqrt{3}} \frac{1}{\gamma} \frac{\Delta\nu}{C_{\text{CW}} \sqrt{R}}$$

for the resonance linewidth  $\Delta\nu$ , the CW contrast  $C_{\text{CW}}$  which differs from  $C_R$ , and the photon count rate  $R$  [43]. The numerical factors have to do with the shape of the resonance in the ODMR spectrum.

Whether a given setup can produce more sensitive measurements with Ramsey or with CW magnetometry depends on the interrelated terms that appear in the above expressions and is therefore rather opaque. The important thing to understand when comparing them is the  $\frac{\sqrt{t_I + \tau + t_R}}{\tau}$  term of the Ramsey magnetometry sensitivity. In the small overhead limit, where  $\tau \gg t_I + t_R$ , this reduces to  $\frac{1}{\sqrt{\tau}}$ , and the optimal

waiting duration is  $\tau = T_2^*/2$ . With extended coherence times [5], the shot noise-limited sensitivity of Ramsey magnetometry can be continuously improved, while the CW ODMR linewidth would remain limited by other sources of broadening.

## 3.2 Laboratory implementation

### 3.2.1 Optical excitation

The NV center electron is excited from the  $^3A_2$  to the  $^3E$  states by absorption of a photon with a higher energy than the optical transition frequency. For this to occur, there must be an optical beam, e.g. from a laser, incident on the diamond with some intensity  $I$  in the vicinity of the NV center. Intensity has the units of  $\text{Wm}^{-2}$ , which for a given photon energy is proportional to the photons per area per time. This is converted to the optical pump rate  $\Gamma$ , the probability of absorption per time, by the absorption cross section  $\sigma$  of units  $\text{m}^2$ . That is,  $\Gamma = I\sigma$ , so with more optical intensity, the NV center will be excited faster into the  $^3E$  states [49, 50].

The NV center spin is initialized by optical excitation. That means that from an arbitrary state of the NV center spin, it decays towards the equilibrium  $m_s=0$  polarization [13, 14]. This occurs due to the probabilistic decay from  $^3E$  down to  $^3A_2$ , either by a direct spin-conserving radiative decay, or via the  $^1A_1$  and  $^1E$  states. This is a series of discrete excitation-decay events, and with each one, the probability distribution of the spin state becomes closer to the probability distribution of the equilibrium polarization, set by the relative rates of the decay paths. The lifetimes of the  $^3E$  states are on the order of  $\sim 1 \mu\text{s}$ , so for low optical pump rates  $\Gamma \ll 1 \text{ MHz}$ , the population of the  $^3A_2$  states dominates. In this low intensity regime, the rate of excitation-decay events is roughly linear with  $\Gamma$ .

### 3.2.2 Laser beam shape

The distribution of optical intensity is generally not uniform. The transverse electric-magnetic mode  $\text{TEM}_{00}$  is commonly produced by laboratory lasers. A beam with a dominant  $\text{TEM}_{00}$  mode is also called a gaussian beam, due to the gaussian distribution of intensity in its transverse plane. This shape is easy to produce with spherical mirrors in the laser cavity, and is useful because of its lower divergence than higher order  $\text{TEM}_{ij}$  modes. The intensity distribution of a  $\text{TEM}_{00}$  beam as a function of radial distance from the center of the transverse plane  $r$  and axial distance from the beam waist  $z$  is

$$I(r, z) = I_0 \left( \frac{r_0(0)}{r_0(z)} \right)^2 \exp \left( -\frac{2r^2}{r_0^2(z)} \right)$$

for the beam radius  $r_0$  [51].

### 3.2.3 Bias magnetic field

When sensing with an ensemble containing randomly oriented NV centers, it is important to apply a magnetic field along one of the crystallographic axes. This shifts its frequency away from the ZFS and distinguishes its resonance from the other NV centers in the ODMR spectrum [20, 52]. A strong field can be used as long as it is well aligned to the NV axis to avoid spin mixing due to the misaligned field components [53]. For our measurements, the strength of the field was chosen such that the NV electron resonance matched the resonance frequency of the MW antenna.



## Part II

# Experimental results



# CHAPTER 4

# Compact NV Magnetometry

---

## 4.1 Background

The value of NV ensemble sensing compared to other magnetic sensing techniques is that an NV ensemble is sensitive at room temperature with a high dynamic range without shielding from large static fields (such as Earth's magnetic field) in a solid state host material that can be very near to the target of sensing. The state of the art technology for high-sensitivity magnetic measurements has been superconducting quantum interference devices (SQUIDs) [54–56], which have reached  $fT/\sqrt{\text{Hz}}$  sensitivity and require large, magnetically shielded setups with cryogenic cooling. Another relevant technology for comparison is optically pumped magnetometers based on atomic vapor cells [57]. Optically pumped magnetometers can have also reached  $fT/\sqrt{\text{Hz}}$  near-zero field sensitivity at room temperature [58] and have been demonstrated in other operational modes in Earth's magnetic field without shielding [59].

The purpose of this work was to take NV ensemble magnetometry techniques that had been demonstrated in bulky laboratory setups and to implement them in a user-focused context, where the robustness of NV sensing in can be advantageous. We continued the work of [60,61] to build a second iteration of the compact sensing setup and took the measurements presented in this article. Our approach was to make all of the setup elements that must be near the diamond such as the MW antenna, bias magnets, laser beam delivery optics, and fluorescence detection optics into a box of a comfortable size to hold in one hand. The laser light was sent into the box by an optical fiber, the MW power was delivered via a coaxial cable, and the detected fluorescence signal was retrieved by another cable.

It is worth briefly comparing this work to [62], which was published while this work was in progress. They achieve slightly better sensitivity in a much smaller integrated device, which uses an LED to optically excite the ensemble rather than a fiber-coupled laser. This work should not be seen as presenting a competitive device, but as a proof of concept, where the magnetic sensitivity achieved in the sensor head was comparable to that achievable on a laboratory table given the same low NV density and isotopically unpurified diamond.

Where sensor size and spatial resolution are a premium, fiberized sensor heads such as [63,64] are a better approach, and they can benefit from efficient fluorescence collection and cavity enhancements [20,65] for CW magnetometry.

## 4.2 Article

This work resulted in a publication titled “Nanotesla Sensitivity Magnetic Field Sensing Using a Compact Diamond Nitrogen-Vacancy Magnetometer” in Applied Physics Letters, presented here.

# Nanotesla sensitivity magnetic field sensing using a compact diamond nitrogen-vacancy magnetometer



Cite as: Appl. Phys. Lett. **114**, 231103 (2019); doi: 10.1063/1.5095241

Submitted: 8 March 2019 · Accepted: 30 May 2019 ·

Published Online: 13 June 2019



View Online



Export Citation



CrossMark

James L. Webb, Joshua D. Clement, Luca Troise, Sepehr Ahmadi, Gustav Juhl Johansen, Alexander Huck, <sup>a)</sup> and Ulrik L. Andersen <sup>b)</sup>

## AFFILIATIONS

Center for Macroscopic Quantum States (bigQ), Department of Physics, Technical University of Denmark, Fysikvej 309, 2800 Kgs. Lyngby, Denmark

<sup>a)</sup>Electronic mail: alexander.huck@fysik.dtu.dk

<sup>b)</sup>Electronic mail: ulrik.andersen@fysik.dtu.dk

## ABSTRACT

Solid state sensors utilizing diamond nitrogen-vacancy (NV) centers are a promising sensing platform that can provide high sensitivity and spatial resolution at high precision. Such sensors have been realized in bulky laboratory-based forms; however, practical applications demand a miniaturized, portable sensor that can function in a wide range of environmental conditions. Here, we demonstrate such a diamond NV magnetic field sensor. The sensor head fits inside a  $11 \times 7 \times 7 \text{ cm}^3$  3D-printed box and exhibits sub-10 nT/ $\sqrt{\text{Hz}}$  sensitivity over a 125 Hz bandwidth. We achieve efficient fluorescence collection using an optical filter and diode in contact with the diamond, which is cut at the Brewster angle to maximize the coupling of 532 nm pump light. We discuss the potential of this flexible approach to achieve sub-nT/ $\sqrt{\text{Hz}}$  shot noise limited sensitivity suitable for detection of a wide range of low-level magnetic fields, particularly those from electrical power systems and from biological sources.

© 2019 Author(s). All article content, except where otherwise noted, is licensed under a Creative Commons Attribution (CC BY) license (<http://creativecommons.org/licenses/by/4.0/>). <https://doi.org/10.1063/1.5095241>

Quantum sensing using nitrogen-vacancy (NV) centers in diamond has attracted widespread interest in recent years due to the extraordinary high sensitivity and high precision sensory capability of materials under ambient conditions.<sup>1</sup> Sensing of electric fields,<sup>2</sup> temperature,<sup>3</sup> strain fields,<sup>4</sup> and pressure<sup>5</sup> has been demonstrated. In particular, research has focused on detection of magnetic fields with a high spatial resolution down to the nanoscale<sup>6–8</sup> and on samples in environmental conditions that cannot be addressed by alternative solid state magnetometers.

The sensing mechanism is based on electron spin resonance via optical detection of fluorescence from an ensemble of NV centers which is sensitive to local magnetic and electric fields, in addition to the background conditions (e.g., temperature). The sensor sensitivity depends on various parameters, in particular, the number of active NV centers and the spin coherence time  $T_2^*$ . These parameters depend on diamond type and the growth method: high pressure high temperature vs chemical vapor deposition, the isotopic composition of the diamond (purified  $^{12}\text{C}$  vs  $^{13}\text{C}$ ), and the defect nitrogen isotope.<sup>9</sup>

Numerous studies on NV based sensors have focused on increasing the sensitivity via higher photon collection efficiency,<sup>10–12</sup> using novel excitation schemes,<sup>13,14</sup> optimized measurement protocols,<sup>15</sup> and diamond structures.<sup>16</sup> Most realizations have been large, bulky setups allowing for maximum optimization and sensitivity in a fixed position. However, as sensor sensitivity now approaches a stage where new interesting applications become possible (e.g., in biodiagnostics), it is of great importance to design and develop miniaturized and movable versions. Recent work has been dedicated to the development of rugged, stable, transportable, and miniaturized diamond sensors to realize such applications.<sup>17–19</sup>

In this article, we present the design and construction of such a miniaturized, handheld diamond magnetic field sensor based on readily available off-the-shelf and 3D printed components. Using a specially cut and coated (but commercially available) diamond sample combined with a cheap microwave (MW) antenna, an optical filter, and a photodiode, we demonstrate a compact NV excitation and fluorescence collection strategy which in turn enables the construction of a

compact hand-held magnetometer head, coupled to an external microwave and laser source. We show that such a sensor can achieve  $7 \text{ nT}/\sqrt{\text{Hz}}$  sensitivity over a bandwidth of 125 Hz, highly suitable for low field, low frequency sensing applications. A NV magnetometer measures external magnetic fields through the Zeeman shift of its spin-triplet  ${}^3\text{A}$  ground state ( $m_s = 0, \pm 1$ ), as shown in Fig. 1. A magnetic field induces an energy shift in the ground triplet state of  $m_s \gamma_e B_z$ , where  $B_z$  is the magnetic field along an NV symmetry axis and  $\gamma_e$  is the gyromagnetic ratio (28 Hz/nT). A measurement of the  $m_s = \pm 1$  NV ground state energy shift thus reveals information about the strength of the magnetic field along an NV axis.

The field-induced energy shift in the triplet is measured using the technique of optically detected magnetic resonance (ODMR), where the NV centers are both optically excited and driven by a microwave (MW) source. When driven with MW frequency corresponding to the spin splitting of the triplet state, relaxation can occur via a singlet state, as shown in Fig. 1. This results in a detectable dip in red  $\approx 637 \text{ nm}$  fluorescence output at a frequency that depends on the Zeeman shift and hence the magnetic field. Intersystem crossing from the singlet shelving state to the  $m_s = 0$  triplet ground state polarizes the spins in the  $m_s = 0$  ground state. Under optical pumping with green laser light, this completes a loop that allows continuous detection of the ODMR fluorescence dip.<sup>20</sup> Detection of ODMR can be via a pulsed scheme, using a Ramsey or spin-echo sequence<sup>9</sup> or, as in this work, a simpler, robust continuous wave (CW) approach with constant laser and MW power.

There are two primary obstacles to achieving high sensitivity in an NV-based sensor. First, it is necessary to efficiently excite the NV centers. The low NV center absorption cross section requires a high

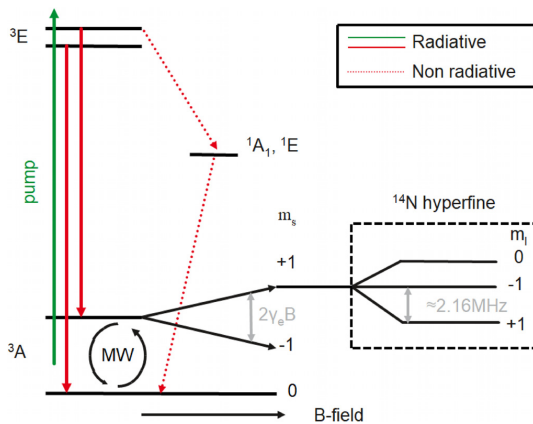


**FIG. 1.** NV energy level scheme. The NV center is optically pumped at 532 nm into the excited triplet state  ${}^3\text{E}$  and decays back into the ground state  ${}^3\text{A}$  with fluorescent red emission. For the  $m_s = 0$  sublevel, emission occurs within the triplet only. For the  $m_s = \pm 1$  levels, intersystem crossing into a singlet state  ${}^1\text{E}$  can lead to decay nonradiatively (or via 1042 nm infrared emission) via the singlet ground state  ${}^1\text{A}$ . This results in a dip in fluorescence output. By transferring the populations between  $m_s = 0$  and  $m_s = \pm 1$ , through absorption of resonant MWs at  $\approx 2.8 \text{ GHz}$ , dependent on the Zeeman shift of the  ${}^3\text{E}$  levels, this dip in fluorescence can be directly observed (ODMR). The electronic transitions are hyperfine split by the  ${}^{14}\text{N}$  nuclear spin.

power pump laser, pump trapping,<sup>13</sup> or an optical cavity.<sup>21</sup> Second, fluorescence light must be efficiently captured, despite the high refractive index of diamond meaning much of it is trapped by total internal reflection. Different schemes to maximize fluorescence collection include using a parabolic collection lens,<sup>12</sup> collection at the diamond edges,<sup>7</sup> and using a dielectric antenna.<sup>11</sup>

In this work, we have addressed these two challenges by using an approach with angled cut diamond end facets that allow a high power, tightly collimated pump beam to travel laterally through the entire diamond width. This is outlined schematically in Fig. 2(a). In addition, we maximize the collection of this light by attaching (using immersion oil) a photodiode to the front surface of the diamond after a thin optical filter while reflective coating the back.

The simplified and compact setup design is presented in Fig. 2(b). We used a commercially available single crystal diamond, grown via chemical vapor deposition with the natural  ${}^{13}\text{C}$  content, with dimensions of  $6 \times 6 \times 1.2 \text{ mm}^3$  from Element 6. The sample had  $[{}^{14}\text{N}] < 1 \text{ ppm}$ , and the natural  $[{}^{14}\text{NV}]$  concentration was determined to be  $\approx 0.2 \text{ ppb}$ .<sup>21</sup> We used a p-polarized pump laser (Cobolt 05-01) with a maximum power of 0.5 W at 532 nm, which can be fiber coupled into the sensor head. The pump beam was collimated to a mode field diameter of approximately  $45 \mu\text{m}$  and focused on one of the edge cut facets of the diamond. The two edge facets for the 532 nm pump beam were cut by Almax easyLab to the Brewster angle of  $67^\circ \pm 0.1^\circ$ , respectively, facilitating efficient entry of the pump beam into the

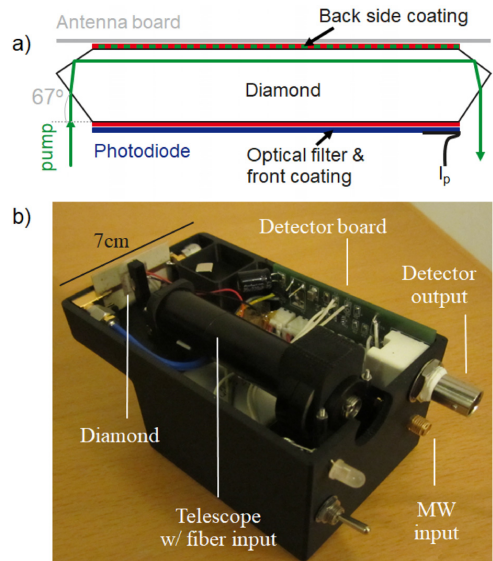


**FIG. 2.** (a) Schematic of the specially cut diamond crystal, optical coatings and filter, attached photodiode, and MW antenna. We use two cut surfaces, one at the diamond Brewster angle ( $67^\circ$ ) to ensure maximum transmission of a beam perpendicular to the diamond front surface and a second cut at  $22.7^\circ$  to direct the beam laterally through the entire width of the diamond, exciting the maximum number of NV centers as possible and exiting at an identically cut facet on the opposite side. (b) Labeled photograph of the opened handheld sensor head.

diamond. We estimate the pump beam to propagate inside at least the full width of the diamond ( $\approx 6$  mm). As indicated in Fig. 2, the back side of the diamond was coated with a highly reflective (HR,  $R > 99\%$ ) coating covering the spectrum 500–800 nm, while the front side was HR ( $R > 99\%$ ) coated for 532 nm and antireflective coated ( $R < 1\%$ ) for 600–800 nm. We attach a 550 nm long pass optical filter (Thorlabs FELH0550, cut to size) before the photodiode to reject stray pump light.

The diamond was mounted onto a printed circuit board with a MW split-ring resonator<sup>22</sup> with a diamond loaded design resonance frequency of 2.89 GHz confirmed by a  $S_{11}$  reflection measurement. Microwaves were delivered from an external source (Stanford SG380 with Minicircuits ZHL-16W-43+ amplifier) at a 500 kHz width frequency modulation at 33.3 kHz. For the magnetic field measurements, we applied a MW drive with three frequency components separated by the  $^{14}\text{N}$  hyperfine frequency of  $f_{\text{hf}} = 2.16$  MHz to boost sensitivity.<sup>21</sup>

For optical detection, we used photodiodes (PDB-C160SMCT-ND, Advanced Photonix), 15 V battery reverse biased. The photodiode responsivity was  $R_{532\text{ nm}} = 0.2$  A/W at 532 nm and  $R_{637\text{ nm}} = 0.37$  A/W at 637 nm. By using a small polarizing beam splitter and half-wave plate, we sampled a fraction of the 532 nm pump laser beam and directed this onto a secondary, identical photodiode in a balanced detection scheme in order to perform common mode rejection (CMR) of pump laser technical noise. The resulting signal was passed into a lock-in amplifier (Stanford Research 850), external to the sensor head, locked to the MW modulation frequency (33.3 kHz), with output digitized by an external analog-to-digital converter (NI-DAQ 6221) allowing precise detection of the ODMR spectrum. We consider that in an updated design, these components could be readily incorporated in the sensor head.

We optimized our setup by first measuring the DC photocurrent  $I_{\text{pc}}$  directly using an ammeter from the primary photodiode on the diamond as a function of pump laser power from 30 mW up to 0.5 W. We also measured the amplitude spectral density (ASD) of the detected modulated ( $f_m = 33.3$  kHz) fluorescence signal using only the primary photodiode and by CMR via balanced detection. This was done by a fast-Fourier transform of a 1 s signal digitized at 125 kSa/s, taking the average level up to the  $-3$  dB filter roll-off imposed by the lock-in time constant (1 ms). The ASD as a function of  $I_{\text{pc}}$  can be seen in Fig. 3 alongside the shot noise level, calculated from the DC photocurrent, and the electronic noise floor. We define the electronic noise floor as the noise level from the detection electronics with zero pump and ambient illumination. The single and balanced photodiode data therefore include this electronic noise. The measurements demonstrate the dominance of technical noise from the pump laser over all other sources of noise. CMR of technical noise was able to reduce the noise level by  $> \times 10$  vs single diode detection. Using CMR, we were able to obtain near shot noise limited fluorescence detection, the difference being due to the limitations of our manual (optical) balancing scheme. We measured photocurrent to scale linearly with pump power, indicating better photodetection sensitivity at high power (due to the scaling of shot noise with the root of laser power). Using maximum laser power (0.5 W), we then measured the ODMR spectrum from the diamond. In order to resolve the  $^{14}\text{N}$  hyperfine structure, we use a fixed offset field  $\approx 1$  mT from two rare earth magnets. The optical magnetic resonance spectrum was recorded by sweeping the MW frequency, measuring the modulated photovoltage using a lock-in amplifier. The

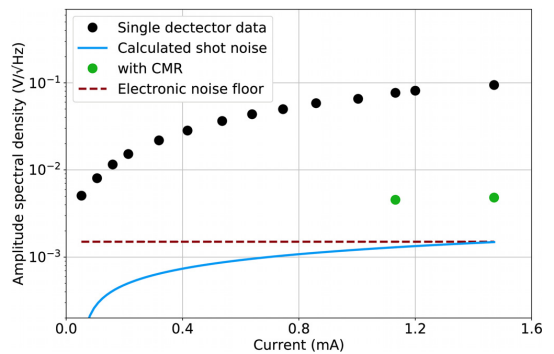


**FIG. 3.** Mean amplitude spectral density of the optical signal over the 125 Hz sensing bandwidth, plotted as a function of photocurrent,  $I_{\text{pc}}$  for a single photodiode (the primary photodiode on the diamond), at 330 mW and 0.5 W for two photodiodes in a balanced configuration to reject common mode noise (with CMR). We also plot the shot noise for a single detector calculated from  $I_{\text{pc}}$  ( $\times \sqrt{2}$  for CMR) and the electronic noise floor.

plotted spectrum in Fig. 4 arises from the deliberate permanent magnet alignment along one of the four (111) NV axes and clearly shows the  $^{14}\text{N}$  hyperfine splitting. By a linear fit to the ODMR spectrum, we determine a slope of  $25 \mu\text{V}/\text{Hz}$  corresponding to  $0.7$  mV/nT assuming a shift of  $28$  Hz/nT. This slope was optimized by repeating the ODMR spectrum as a function of MW drive power. The optimum power prior to amplification was 4 dBm and  $-2$  dBm for the main and 2.16 MHz drive, respectively, giving  $\approx 6$  W from the amplifier. We note importantly no saturation of the ODMR contrast with laser power, an issue that can limit NV sensor sensitivity.<sup>23</sup> With the sensitivity determined from the ODMR spectrum, we measured magnetic sensitivity as a function of magnetic field frequency, again by fast-

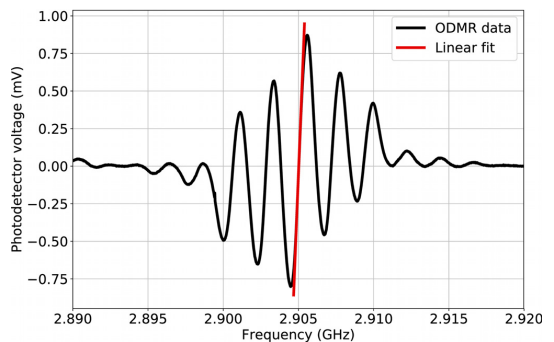


**FIG. 4.** Optically detected magnetic resonance (ODMR) spectrum, recorded as a function of MW drive frequency with CMR on. We observe the  $m_s = 0 \leftrightarrow +1$  electron spin transition and hyperfine splitting arising from  $^{14}\text{N}$ . By a linear fit to the slope of the ODMR spectrum, we determined the relation between signal voltage and frequency shift to be  $25 \mu\text{V}/\text{Hz}$ , from which we determined the magnetic field sensitivity using the relation  $\gamma_e B_z$ , assuming  $\gamma_e = 28$  Hz/nT.

Fourier transform of 1 s of digitized signal at 125 kSa/s. The magnetic noise density spectrum is plotted in Fig. 5. We compare sensitivity with CMR on and off and at MW drive frequencies of 2.905 GHz and 2.908 GHz, corresponding to the points of maximum (least) magnetic field sensitivity as determined from the maximum slope (peak) of the ODMR spectrum. We plot the ultimate electronic noise floor, defined by our amplifier and analog-to-digital converter, located at  $\approx 2 \text{ nT}/\sqrt{\text{Hz}}$ .

The amplitude spectrum shows a noise floor of  $\approx 150 \text{ nT}/\sqrt{\text{Hz}}$  without CMR and  $\approx 7 \text{ nT}/\sqrt{\text{Hz}}$  with CMR turned on. This highlights how essential rejection of laser technical noise is in diamond magnetometry. When magnetically sensitive, we observed peaks primarily at 50 Hz and 150 Hz. Such peaks were not observed when at a magnetically insensitive drive frequency (2.908 GHz). These frequencies correspond clearly to direct detection of the magnetic field produced by nearby electrical transformers: the strong 3rd harmonic at 150 Hz is a frequency component of the transformer magnetic field produced by magnetic hysteresis in the transformer core. Were we detecting spurious mains electrical noise, the 2nd harmonic at 100 Hz would also be strongly present. Peaks at 60 Hz and higher harmonics were traced to inbuilt components in United States-purchased equipment.

Based on the detected photocurrent, we calculate the total optical power detected by the primary photodiode to be 3.6 mW. This corresponds to an estimated shot noise limited sensitivity of  $\approx 3 \text{ nT}/\sqrt{\text{Hz}}$ . The absorption cross section at 532 nm for a single  $^{14}\text{NV}$  center is reported<sup>24</sup> to be  $\sigma_{\text{NV}} = 3.1 \times 10^{-15} \text{ mm}^2$ . Taking a NV density of  $6.4 \times 10^{13} \text{ cm}^{-3}$ , a NV quantum efficiency of  $\eta \approx 0.9$ ,<sup>25</sup> and a propagation length inside the diamond of 6 mm, the fluorescence power from the ensemble is 0.53 mW at the maximum pump power (0.5 W). This is significantly lower than the measured fluorescence power of 3.6 mW. This illustrates that the majority of the photocurrent is due to leakage of pump light past the filter and into the photodiode. It also highlights the minimal single pass absorption of the pump light by our diamond with this level of NV defects. Such absorption can be enhanced by

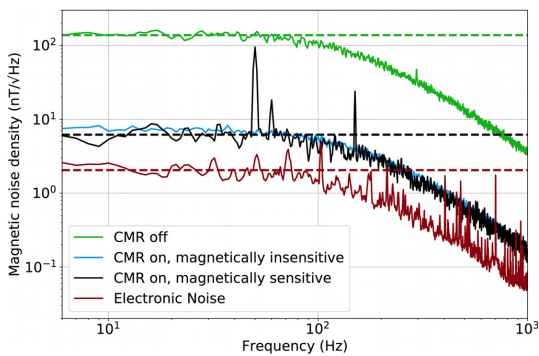


**FIG. 5.** Magnetic noise frequency spectrum at 0.5 W pump power, plotted as ASD in  $\text{nT}/\sqrt{\text{Hz}}$ . We show the noise density without balanced detection (CMR off), with CMR on and the detector magnetically sensitive (2.905 GHz) and insensitive (2.908 GHz). We also show the electronic limit (pump off). We observe a mean noise floor of  $7 \text{ nT}/\sqrt{\text{Hz}}$  when rejecting laser technical noise. We observe the same high frequency peaks at 400–1 kHz on all data, from the power supplies and cooling fans. Only when magnetically sensitive do we clearly observe 50/150 Hz peaks from mains transformer field.

boosting defect density via optimized doping, irradiation, and annealing or by use of an optical cavity around the diamond.<sup>25</sup>

Our current design has potential to be improved to subnanotesla sensitivity and in compactness and size. The primary limitation of our sensor head size was the internal focusing optics, which could be further miniaturized. Increasing the NV concentration in combination with  $^{12}\text{C}$  purification has been shown to improve ODMR contrast and reduce linewidth.<sup>9</sup> Leakage of pump light, in a wide range of incidence angles, proved difficult to fully reject in our sensor using available commercial filters. Further improvement in filter composition and structure is required in this geometry. Moving the filter away from the diamond surface to narrow the incidence angle of scattered pump light would help, but at the expense of sensor miniaturization. An ideal filter rejecting all pump light reduces the shot noise by approximately a factor of 2–3. Electronic balancing of the detection and CMR would reduce our electronic noise floor. In the shot noise limit, simply increasing laser power would improve sensitivity (3.3 W pump power has been demonstrated<sup>26</sup>). We note that our bandwidth is not imposed by the physics of our sensor and could easily be increased in order to detect higher frequency fields, limited only by relaxation time  $T_2^*$ . A noise source not considered here is temperature variation, dependent on heat dissipation and the local environment. It has been demonstrated that such temperature effects can be efficiently corrected by driving simultaneously at both the  $m_0 = \pm 1 \text{ MW}$  resonances.<sup>27</sup>

Several recent efforts have been made to produce a miniaturized NV magnetometer as an integrated package,<sup>18,19</sup> with onboard light and MW sources, of sensitivity in the 30–100  $\text{nT}/\sqrt{\text{Hz}}$  range. We show that to achieve subnanotesla level sensitivity may require pump power of the order of several Watts for a millimeter-scale diamond with a sufficiently large NV ensemble at currently achievable NV defect densities and levels of material strain. This factor suggests that having a sensor head(s) into which laser and MWs can be coupled (a setup common in, e.g., medical devices) may be preferable for high sensitivity operation, since it may be difficult to generate enough power at low electronic noise in an integrated package within the sensor head.

The level of sensitivity we demonstrate in this work should permit many new applications. We particularly highlight applications in sensing of weak (nanotesla, picotesla scale) magnetic fields from biological sources, such as living tissue or samples in solution. This can be difficult for alternative techniques, e.g., unencapsulated magnetoresistive sensors, relying on electrical readout. Biocompatibility of diamond allows high proximity with a sample, assisting field detection given the rapid (cubic) drop in field strength with distance. Competing techniques may need to be positioned relatively far (many millimeters) from the sample. Of particular interest is sensing of bioelectric signals by their magnetic field that cannot otherwise be easily accessed by electrical probes (for example, magnetoencephalography of the brain) where current magnetometers—superconducting quantum interference (SQUID) devices or recently demonstrated atomic vapor cells<sup>28</sup>—are expensive and cumbersome and have poor spatial resolution.

High spatial resolution in diamond NV sensors can be readily achieved by imaging fluorescence with a camera and has been demonstrated elsewhere in, e.g., geological samples<sup>29</sup> and magnetic bacteria to the micrometer scale.<sup>30</sup> Biological signals are typically observed in the hundreds of hertz to low-kilohertz frequency range, over which we demonstrate excellent sensitivity in this work. Other low frequency

magnetic signals of interest include diagnostics of mains power systems (transformers, motors) operating at DC or single/three phase 50/60 Hz.

In conclusion, we have developed a diamond magnetometer with a handheld sensing head, with a sensitivity of  $7 \text{ nT}/\sqrt{\text{Hz}}$  and an ultimate noise floor of  $3 \text{ nT}/\sqrt{\text{Hz}}$ . We demonstrate robust, flexible sensing using diamond NV centers which is not limited to fixed benchtop applications. We discuss a route to achieving sub-nT/ $\sqrt{\text{Hz}}$  sensitivity through improvements in the NV-concentration, optical filtering, and detection and by implementing pulsed measurement schemes.

We gratefully acknowledge Kristian H. Rasmussen and Aleksander Tchernavskij for support in fabrication and electronic design. This project was financially supported by the Innovation Fund Denmark (EXMAD project and Qubiz center) and the Novo Nordisk foundation (bioQ project).

## REFERENCES

- <sup>1</sup>J. M. Taylor, P. Cappellaro, L. Childress, L. Jiang, D. Budker, P. R. Hemmer, A. Yacoby, R. Walsworth, and M. D. Lukin, *Nat. Phys.* **4**, 810 (2008).
- <sup>2</sup>F. Dolde, H. Fedder, M. W. Doherty, T. Noebauer, F. Rempp, G. Balasubramanian, T. Wolf, F. Reinhard, L. C. L. Hollenberg, F. Jelezko, J. Wrachtrup, and T. Nöbauer, *Nat. Phys.* **7**, 459 (2011).
- <sup>3</sup>V. M. Acosta, E. Bauch, M. P. Ledbetter, A. Waxman, L.-S. Bouchard, and D. Budker, *Phys. Rev. Lett.* **104**, 070801 (2010).
- <sup>4</sup>M. E. Trusheim and D. Englund, *New J. Phys.* **18**, 123023 (2016).
- <sup>5</sup>M. W. Doherty, V. V. Struzhkin, D. A. Simpson, L. P. McGuinness, Y. Meng, A. Stacey, T. J. Karle, R. J. Hemley, N. B. Manson, L. C. Hollenberg, and S. Praver, *Phys. Rev. Lett.* **112**, 047601 (2014).
- <sup>6</sup>P. Maletinsky, S. Hong, M. S. Grinolds, B. Hausmann, M. D. Lukin, R. L. Walsworth, M. Loncar, and A. Yacoby, *Nat. Nanotechnol.* **7**, 320 (2012).
- <sup>7</sup>D. Le Sage, L. M. Pham, N. Bar-Gill, C. Belthangady, M. D. Lukin, A. Yacoby, and R. L. Walsworth, *Phys. Rev. B* **85**, 121202 (2012).
- <sup>8</sup>K. Jensen, V. M. Acosta, A. Jarmola, and D. Budker, *Phys. Rev. B* **87**, 014115 (2013).
- <sup>9</sup>L. Rondin, J.-P. Tetienne, T. Hingant, J.-F. Roch, P. Maletinsky, and V. Jacques, *Rep. Prog. Phys.* **77**, 056503 (2014).
- <sup>10</sup>L. Marseglia, J. P. Hadden, A. Stanley-Clarke, J. P. Harrison, B. Patton, Y.-L. D. Ho, B. Naydenov, F. Jelezko, J. Meijer, P. R. Dolan, J. M. Smith, J. G. Rarity, and J. L. O'Brien, *Appl. Phys. Lett.* **98**, 133107 (2011).
- <sup>11</sup>D. Riedel, D. Rohner, M. Ganzhorn, T. Kaldewey, P. Appel, E. Neu, R. Warburton, and P. Maletinsky, *Phys. Rev. Appl.* **2**, 064011 (2014).
- <sup>12</sup>T. Wolf, P. Neumann, K. Nakamura, H. Sumiya, T. Ohshima, J. Isoya, and J. Wrachtrup, *Phys. Rev. X* **5**, 041001 (2015).
- <sup>13</sup>H. Clevenson, M. E. Trusheim, C. Teale, T. Schröder, D. Braje, and D. Englund, *Nat. Phys.* **11**, 393 (2015).
- <sup>14</sup>L. Bougas, A. Wilzewski, Y. Dumeige, D. Antypas, T. Wu, A. Wickenbrock, E. Bourgeois, M. Nesladek, H. Clevenson, D. Braje, D. Englund, and D. Budker, *Micromachines* **9**, 276 (2018).
- <sup>15</sup>V. M. Acosta, E. Bauch, A. Jarmola, L. J. Zipp, M. P. Ledbetter, and D. Budker, *Appl. Phys. Lett.* **97**, 174104 (2010).
- <sup>16</sup>G. Balasubramanian, P. Neumann, D. Twitchen, M. Markham, R. Kolesov, N. Mizuochi, J. Isoya, J. Achard, J. Beck, J. Tissler, V. Jacques, P. R. Hemmer, F. Jelezko, and J. Wrachtrup, *Nat. Mater.* **8**, 383 (2009).
- <sup>17</sup>G. Chatzidrosos, A. Wickenbrock, L. Bougas, N. Leefer, T. Wu, K. Jensen, Y. Dumeige, and D. Budker, *Phys. Rev. Appl.* **8**, 044019 (2017).
- <sup>18</sup>F. M. Strner, A. Brenneis, J. Kassel, U. Wostradowski, R. Rlver, T. Fuchs, K. Nakamura, H. Sumiya, S. Onoda, J. Isoya, and F. Jelezko, *Diamond Relat. Mater.* **93**, 59 (2019).
- <sup>19</sup>M. I. Ibrahim, C. Foy, D. Kim, D. R. Englund, and R. Han, in *2018 IEEE Symposium on VLSI Circuits* (2018), pp. 249–250.
- <sup>20</sup>G. M. H. Thiering and A. Gali, *Phys. Rev. B* **98**, 085207 (2018).
- <sup>21</sup>S. Ahmadi, H. A. El-Ella, J. O. Hansen, A. Huck, and U. L. Andersen, *Phys. Rev. Appl.* **8**, 034001 (2017).
- <sup>22</sup>K. Bayat, J. Choy, M. Farrokh Baroughi, S. Meesala, and M. Loncar, *Nano Lett.* **14**, 1208 (2014).
- <sup>23</sup>A. Dréau, M. Lesik, L. Rondin, P. Spinicelli, O. Arcizet, J.-F. Roch, and V. Jacques, *Phys. Rev. B* **84**, 195204 (2011).
- <sup>24</sup>T.-L. Wee, Y.-K. Tzeng, C.-C. Han, H.-C. Chang, W. Fann, J.-H. Hsu, K.-M. Chen, and Y.-C. Yu, *J. Phys. Chem. A* **111**, 9379 (2007).
- <sup>25</sup>S. Ahmadi, H. A. R. El-Ella, A. M. Wojciechowski, T. Gehring, J. O. B. Hansen, A. Huck, and U. L. Andersen, *Phys. Rev. B* **97**, 024105 (2018).
- <sup>26</sup>J. M. Schloss, J. F. Barry, M. J. Turner, and R. L. Walsworth, *Phys. Rev. Appl.* **10**, 034044 (2018).
- <sup>27</sup>A. M. Wojciechowski, M. Karadas, C. Osterkamp, S. Jankuhn, J. Meijer, F. Jelezko, A. Huck, and U. L. Andersen, *Appl. Phys. Lett.* **113**, 013502 (2018).
- <sup>28</sup>E. Boto, N. Holmes, J. Leggett, G. Roberts, V. Shah, S. S. Meyer, L. D. Muñoz, K. J. Mullinger, T. M. Tierney, S. Bestmann, G. R. Barnes, R. Bowtell, and M. J. Brookes, *Nature* **555**, 657 (2018).
- <sup>29</sup>D. R. Glenn, R. R. Fu, P. Kehayias, D. Le Sage, E. A. Lima, B. P. Weiss, and R. L. Walsworth, *Geochem., Geophys., Geosyst.* **18**, 3254, <https://doi.org/10.1002/2017GC006946> (2017).
- <sup>30</sup>D. Le Sage, K. Arai, D. R. Glenn, S. J. Devience, L. M. Pham, L. Rahn-Lee, M. D. Lukin, A. Yacoby, A. Komeili, and R. L. Walsworth, *Nature* **496**, 486 (2013).



# CHAPTER 5

## Optimal control of an NV ensemble

---

### 5.1 Background

At the stage of the project after completion of the compact magnetometry measurements presented in Chapter 4, we attempted to adapt the compact setup for magnetoneurography of a human median nerve to produce a proof-of-concept as earlier demonstrated with SQUIDs [66]. We were ultimately unable to detect a signal due to limited sensitivity, primarily because of the low NV concentration and poor coherence times (due to  $^{13}\text{C}$ ) of the diamond itself. Nevertheless, we were able to address a large enough volume in the diamond that the necessary sensitivity could have been in reach. In parallel with acquiring another diamond, we considered how to better utilize the sensing volume of the diamond we had.

Sensing with either Ramsey magnetometry (**cite**) or pulsed ODMR [37] should have a greater possible sensitivity than CW ODMR methods. Moreover, there are sensitivity-enhancing techniques only available to pulsed measurements schemes such as Double Quantum magnetometry [67] or other spin readout methods such as spin-charge state conversion [34, 35].

Pulsed sensing relies on discrete MW control pulses to apply  $\pi$  and/or  $\pi/2$  rotations around the Bloch sphere of the NV center electron spin as described in Chapter 2.4. Because the degree of rotation on the Bloch sphere for a MW pulse of fixed duration is a function of the MW power, the homogeneity of the MW field throughout the NV ensemble volume is more critical for pulsed sensing than for CW ODMR. The detuning  $\Delta$  can also vary throughout the ensemble in an inhomogeneous magnetic bias field [65] or with strain in the diamond [5]. This is a key reason why pulsed measurements are typically limited to smaller ensembles or single NV centers. In this work, we aimed to make pulsed sensing techniques applicable to large ensembles by using optimal control methods [26, 68, 69] to correct for the inhomogeneous application of MW power and the greater inhomogeneity of resonance frequency that followed from the large ensemble volume.

## 5.2 Article

This work resulted in the following article titled “Optimal control of a nitrogen-vacancy spin ensemble in diamond for sensing in the pulsed domain”, which we have submitted to Physical Review B. It is currently under review. The article is presented here as submitted followed by its Supplementary Information.

# Optimal control of a nitrogen-vacancy spin ensemble in diamond for sensing in the pulsed domain

Andreas F.L. Poulsen,<sup>1,\*</sup> Joshua D. Clement,<sup>1,\*</sup> James L. Webb,<sup>1,†</sup> Rasmus H. Jensen,<sup>1</sup> Kirstine Berg-Sørensen,<sup>2</sup> Alexander Huck,<sup>1,‡</sup> and Ulrik Lund Andersen<sup>1,§</sup>

<sup>1</sup>*Center for Macroscopic Quantum States (bigQ), Department of Physics,*

*Technical University of Denmark, Kgs. Lyngby, Denmark*

<sup>2</sup>*Department of Health Technology, Technical University of Denmark, Kgs. Lyngby, Denmark*

Defects in solid state materials provide an ideal, robust platform for quantum sensing. To deliver maximum sensitivity, a large ensemble of non-interacting defects hosting quantum states with long coherence is required. Control of such an ensemble under realistic conditions is challenging due to the spatial variation in both the defect energy levels and in any control field across a macroscopic sample. In this work, we experimentally demonstrate that we can overcome these challenges using Floquet theory and optimal control optimization methods to efficiently and coherently control a large defect ensemble, suitable for sensing. We apply our methods experimentally to a spin ensemble of up to  $1 \times 10^9$  nitrogen vacancy (NV) centers in diamond in a  $0.01 \text{ mm}^3$  sensing volume. By explicitly including the hyperfine interaction to the intrinsic  $^{14}\text{N}$  nuclear spin in the optimization, we design shaped microwave control pulses that can outperform conventional ( $\pi$ -) pulses when applied to sensing schemes, with a sensitivity improvement between 11 and 78%. Through simulation of the ensemble dynamics, we shed light on the bandwidth limitations of large-ensemble reinitialization and propose new routes for further improvement.

## I. INTRODUCTION

Solid state defects constitute a promising platform for quantum sensing, where purely quantum mechanical properties such as superposition and entanglement can be utilized to overcome the traditional limitations [1]. Particularly in semiconductors, where they can be controllably created and manipulated, solid state defects can host quantum states that are both long-lived and sensitive to the environmental parameters. A typical and extensively used defect system is the nitrogen-vacancy (NV) center in diamond. It consists of a substitutional nitrogen atom and an adjacent lattice vacancy, having discrete electronic and nuclear spin states with long coherence times at room temperature [2]. The optical and electronic properties of the negatively-charged NV center ( $\text{NV}^-$ ) are highly sensitive to a range of parameters including magnetic field [3–7], electric field [8], temperature [9, 10] and pressure (strain) [11], and applications include scanning-tip nano-microscopy [12, 13], nanoscale nuclear magnetic resonance (NMR) and electron spin resonance (ESR) [14, 15] and in detection of biophysical signals [16–19], where robustness and high biocompatibility of diamond makes it an ideal platform for sensing, even within biological samples [20, 21].

The level structure of the  $\text{NV}^-$ , illustrated schematically in Fig. 1(a) consists of electron spin triplet ground  $^3\text{A}_2$  and excited  $^3\text{E}$  states and metastable spin singlet levels [5, 22–25]. After absorbing a green pump pho-

ton, an NV center can emit red fluorescence in the radiative decay from  $^3\text{E}$  to  $^3\text{A}_2$ . Nonradiative decays may occur through non-spin-conserving singlet state transitions, and this is more likely from the  $m_s = \pm 1$  levels. Therefore, the (bright) maximally fluorescent  $|m_s = 0\rangle$  state can be distinguished from the (dark) minimally fluorescent  $|m_s = \pm 1\rangle$  spin states under green pump illumination, and the state is reinitialized into  $|m_s = 0\rangle$  in the readout process. In this work, we simplify the notation of these spin states to  $|0\rangle$  and  $|\pm 1\rangle$  respectively. The spin states can be controlled coherently by applying resonant microwaves (MW), where the resonance frequency depends on the external magnetic field via the Zeeman effect and on the hyperfine coupling to the  $^{14}\text{N}$  or  $^{15}\text{N}$  impurity atom's nuclear spin [26]. Together, this allows for optically detected magnetic resonance (ODMR) spectroscopy by sweeping the microwave frequency and noting the decrease in fluorescence output when more population is transferred to the dark  $|\pm 1\rangle$  states, yielding a typical contrast  $C$  of up to 30% for a single NV [25] or  $\sim 1$ -2% for a large ensemble without preferential NV alignment [27]. By fixing the microwave drive frequency on or close to one resonance, a level shift of  $m_s = \pm 1$  relative to  $m_s = 0$  caused by magnetic field, electric field or local temperature can be detected.

Sensing using NV centers can be performed with a variety of measurement protocols, the simplest being continuous wave (CW) with a constant intensity of microwave and laser irradiation [23, 28]. Alternatively, by treating one of the spin transitions (e.g.  $|0\rangle \leftrightarrow |\pm 1\rangle$ ) as a two-level quantized system [29], discrete laser and microwave pulses can be used to coherently control and read the spin state [25, 30], offering improvement over CW methods through increased contrast and reduced power broadening of the resonance frequency. More advanced techniques relying on coherent control such as Ramsey in-

---

\* These authors contributed equally to this work

† jaluwe@fysik.dtu.dk

‡ alexander.huck@fysik.dtu.dk

§ ulrik.andersen@fysik.dtu.dk

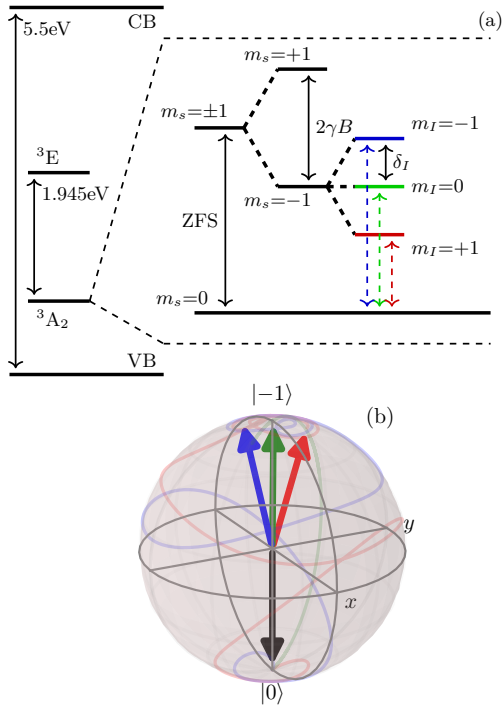


FIG. 1. Color online. (a) Simplified level diagram for a single  $\text{NV}^-$  center within the diamond bandgap, with the ground state levels shown in detail. At zero magnetic field there is a splitting of 2.87 GHz (ZFS) between the  $m_s=0$  and  $m_s=\pm 1$  states. At finite field  $B$ , the Zeeman effect shifts the  $m_s=\pm 1$  states in energy by  $\gamma B$ . The  $m_s=\pm 1$  states are further split into 3 hyperfine levels ( $m_I=0, \pm 1$ ) separated by  $\delta_I = 2.16$  MHz. (b) Bloch sphere representation depicting this  $m_s = \{0, -1\}$  two-level system and the time evolution and result vector for a shaped optimal control MW pulse applied to the initial ground state  $|0\rangle$ , (black arrow). Here we show the time evolution for each of the hyperfine resonances  $m_I$ .

terferometry [31, 32] and Hahn echo-type sequences have been demonstrated [33, 34], e.g. realizing single molecule sensitivity in nanoscale diamond NMR experiments [35–37].

Pulsed schemes are used in single- or few-NV systems mostly in confocal microscopy setups [38–40] as well as arbitrarily large macroscopic spin ensembles [41]. Large ensembles are necessary to maximize bulk sensitivity where spatial resolution is not required, since the shot noise-limited sensitivity scales as  $1/\sqrt{N}$ , with  $N$  the number of defect centers [3]. The simplest method to coherently control an NV ensemble for sensing is to use MW pulses with constant amplitude and phase, which we refer to in this work as flat pulses. Ensemble NV sensing performed with flat pulses suffers from nonuni-

form pulse operation. Due to differences in their local environment caused by e.g. strain, bias field gradients or the presence of  $^{13}\text{C}$  nuclear spins, different NV centers in an ensemble will have different resonance frequencies for the driven transition, resulting in a distribution of detuning from the ensemble mean, commonly referred to as inhomogeneous broadening. In addition, the near-field microwave drive can vary in intensity across the ensemble, depending on the antenna design and microwave coupling to the diamond [42]. These deviations in resonance frequency and field intensity respectively cause the microwave control pulse to be detuned for some of the NV centers and to over- or under-rotate spins with respect to a desired operation with a detrimental impact on the resulting ensemble-averaged spin state.

When sensing is limited by the negative impact of these ensemble inhomogeneities on flat microwave pulse performance, shaped microwave pulses with time-varying phase and amplitude can be used to compensate for the ensemble inhomogeneities. Optimal control methods have been used to select parameters for control pulses of various parameterizations to be maximally robust against these inhomogeneities [33, 43–45]. Such optimal control pulses have been used with an ensemble of NV centers in a  $\ll 1 \mu\text{m}^3$  volume for Hahn-echo measurements in a confocal setup [33, 46], for wide field MRI measurements applying an XY16 sequence to an ensemble in a volume of  $\sim 10 \mu\text{m}^3$  [47], to improve the robustness and temperature sensitivity of the D-Ramsey scheme in nanodiamonds [48], to extend the coherence time of a single NV by controlling the surrounding spins [49], and to improve the accuracy of entanglement operations between two proximal NV centers [50].

In this work, we demonstrate the use of shaped microwave pulses produced by optimal control methods combined with Floquet theory to improve coherent control of an ensemble of  $\sim \times 10^9$  NV centers in a volume of  $\sim 0.01 \text{mm}^3$ . This is a substantial increase compared to ensemble volumes in the  $\mu\text{m}^3$  range in previous demonstrations [47]. Our optimal control pulses are derived including the hyperfine interaction with  $^{14}\text{N}$  nuclear spins, and we experimentally show improved slope of the ODMR contrast by up to 11% compared to a conventional flat  $\pi$ -pulse sensing scheme. In the experiment, we used off-the-shelf, optical grade diamond material, and we demonstrate operation at low Rabi frequencies smaller than the  $^{14}\text{N}$  hyperfine splitting, typical of those achievable using low-power microwave amplification e.g. in a portable sensor device [51]. Though we used NV centers in diamond, our technique is widely adaptable to a range of solid state systems where large ensembles of two-level quantum systems can be realized.

The paper is structured as follows. In Section II, we outline the basic methodology we use to construct and generate our shaped microwave pulses using optimal control theory, including our derivation for explicitly including the hyperfine interaction in the optimization algorithm. We describe a number of key control parameters,

the limits of which we discuss in Section II B. In Section II C, we describe in detail our experimental setup and methodology. In Sections III A and III B, we demonstrate the use of optimized shaped pulses for ODMR spectroscopy, compare to a conventional  $\pi$ -pulse scheme using a flat microwave pulse, and analyze and discuss the optical behavior and how this relates to the physical dynamics of the NV ensemble.

## II. METHODS

### A. Optimal Control

Our optimal control algorithm maximizes a functional that describes the desired transfer of one quantum state to another [23, 33, 44, 45, 52]. We define our state transfer functional as:

$$\mathcal{F}_{\text{st}} = \left| \langle \psi_f | \hat{U}(t_p) | \psi_i \rangle \right|^2, \quad (1)$$

where  $\mathcal{F}_{\text{st}}$  is the fidelity, of value between 0 and 1, which describes how well the pulse transfers the system from an initial state  $|\psi_i\rangle$  to a final state  $|\psi_f\rangle$ . A fidelity of 1 represents a complete transfer to the desired state. The influence of the pulse is described by the unitary time evolution operator  $\hat{U}(t_p)$ , where  $t_p$  is the control pulse duration.

To represent the state transfer of an experimental ensemble, we calculate  $\mathcal{F}_{\text{st}}$  for each member of a representative ensemble of defects with a specified range of frequency detuning  $\hat{\Delta}$  and relative control amplitude  $\hat{\alpha}$ . These factors are set to be representative of the variation across a real ensemble. The relative control amplitudes  $\alpha_i$  represent the drive field inhomogeneity across the ensemble, and each value is the ratio between the Rabi frequency at which a given single defect is driven (due to drive field inhomogeneity) and the Rabi frequency at which the pulse is designed to drive the defects. The values of  $\alpha_i$  thus vary around unity across the representative ensemble. The relative control amplitude only relates to the changes in Rabi frequency caused by drive field inhomogeneity and does not include the effects of frequency detuning on the Rabi frequency. The detuning is included in the optimization separately via the  $\Delta_i$  values, which represent the inhomogeneous broadening. We thus assign each defect in the representative ensemble a value of  $\alpha_i$  and  $\Delta_i$  within the specified range  $\hat{\Delta}$  and  $\hat{\alpha}$  and seek a pulse that maximizes the average fidelity of the entire representative ensemble. Using this model assumes that interaction between defects is minimal, such that each defect can act as a single, isolated quantum system.

We assume our detunings  $\Delta_i$  follow a Gaussian distribution centered at zero. The full width at half maximum (FWHM) of this Gaussian distribution is set equal to half of the width of the considered detuning range  $\hat{\Delta}$ . The  $\alpha_i$  values are assumed to follow a flat distribution over the

considered range  $\hat{\alpha}$ . The weight of each defect in the representative ensemble is thus equal to the weight of its  $\Delta_i$  value. These are normalized such that the sum of the weights of all defects in the representative ensemble is equal to 1. We therefore also use a weighted average of the fidelity. For numerical optimization, we use throughout this work a representative ensemble of size 12x12 (12 values to cover the ranges  $\hat{\Delta}$  and  $\hat{\alpha}$ , respectively). This was based on a series of simulations of the performance of pulses transferring state  $|0\rangle$  to  $|-1\rangle$  (Fig. 1(b)) optimized using different representative ensembles. As shown in Fig. 2, 12x12 more than ensures convergence of the fidelity, while minimizing computational time.

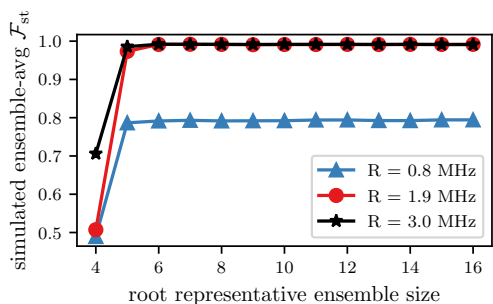


FIG. 2. Color online. The simulated weighted average fidelity of optimal control pulses,  $\mathcal{F}_{\text{st}}$ , optimized with different ensemble sizes as a function of representative ensemble size for three values of the maximum allowed Rabi frequency  $R_{\text{lim}}$ . The pulses were optimized for  $\hat{\Delta}/2\pi = \pm 1$  MHz detuning,  $\hat{\alpha} = 1 \pm 0.1$  amplitude variations and a duration of  $t_p = 1.85 \mu\text{s}$  with the indicated values of  $R = R_{\text{lim}}$ .

For the design of our shaped microwave pulses, we use smooth optimal control. Here we choose a basis of periodic functions with the same periodicity  $T$  and discretized frequency components, resulting in the shaped pulses becoming smooth in time [43]. In this work, we use a basis of sine functions with a fundamental frequency determined by the pulse duration  $t_p$  [33]. Smooth optimal control has the advantages over alternatives such as gradient ascent pulse engineering (GRAPE) [53] that the bandwidth and the individual frequency components are known in advance, and the number of high frequency components in the pulse Fourier spectrum is reduced, making modulation in experiments less technically demanding [43]. Our smooth optimal control pulse has the general form:

$$S(t) = I(t) \cos(\omega_D t) + Q(t) \sin(\omega_D t), \quad (2)$$

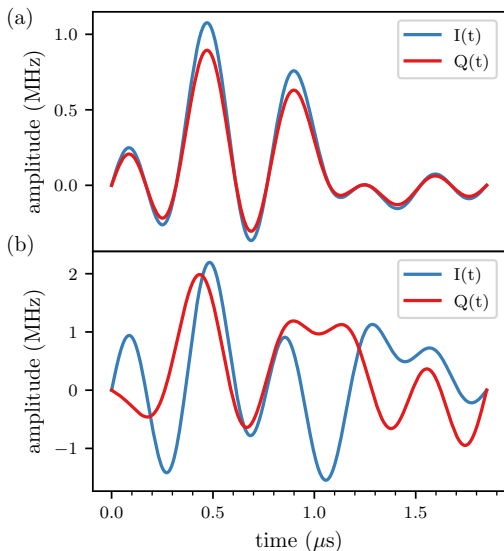


FIG. 3. Color online. Plot of  $I(t)$  and  $Q(t)$  in units of Rabi frequency for two optimal control pulses that were optimized by including state transfer using all three  $^{14}\text{N}$  hyperfine levels. The pulses were optimized for  $\Delta/2\pi = \pm 1$  MHz detuning and  $\hat{\alpha} = 1 \pm 10\%$  amplitude variations with a duration of  $t_p = 1.85 \mu\text{s}$  and a maximum allowed Rabi frequency  $R_{\text{lim}}$  of (a) 1.4 MHz and (b) 3.0 MHz.

where

$$\begin{aligned}
 I(t) &= \sum_{j=1}^{N_f} 2a_{jx} \sin(j\Omega_f t), \\
 Q(t) &= \sum_{j=1}^{N_f} 2a_{jy} \sin(j\Omega_f t).
 \end{aligned}
 \tag{3}$$

Here,  $\omega_D$  is the central driving frequency,  $\Omega_f = 2\pi/(2t_p)$  is the fundamental frequency,  $N_f$  is the number of frequency components, and the real  $a_{jk}$ -values are control amplitudes. The bandwidth of such a pulse is then  $N_f\Omega_f$ . The fundamental frequency is not related to the Rabi frequency and purely serves to enforce the desired periodicity of  $T = 2t_p$ . The  $a_{jk}$ -values are, defined in units of Rabi frequency  $R$  by which the  $j^{\text{th}}$  frequency component's  $k^{\text{th}}$  quadrature drives the spin. As an example, Fig. 3 shows the in-phase and quadrature components  $I(t)$  and  $Q(t)$  used to modulate the microwave carrier for two of the specific pulses that we designed. In our experiments, the microwave carrier has a frequency  $\omega_D/2\pi \approx 2.8$  GHz corresponding to the splitting between the  $m_s=0$  and  $m_s=-1$  levels of the NV center  $^3\text{A}_2$  ground state with an applied bias magnetic field.

It has been previously shown[46] that the performance of smooth optimal control pulses improves with increas-

ing  $N_f$  until it saturates for  $N_f \geq 7$ . We use  $N_f = 10$  for all of our pulses to ensure that we are in the saturated regime. This yields 20 different control amplitudes  $a_{jk}$  per shaped pulse, and these are the parameters that are optimized by the control algorithm. The optimization is carried out iteratively by stepping along the gradient of the fidelity with respect to the control amplitudes with a step size  $\beta$ . Starting with initial control amplitudes  $a_{jk} = a_{jk0}$ , we compute the resulting  $\hat{U}(t_p)$ ,  $\mathcal{F}_{\text{st}}$  and  $\frac{\partial \mathcal{F}_{\text{st}}}{\partial a_{jk}}$ , before updating each control amplitude by adding  $\beta \frac{\partial \mathcal{F}_{\text{st}}}{\partial a_{jk}}$ . This process is then repeated until  $\mathcal{F}_{\text{st}}$  converges. The choice of time-periodic basis functions yields a time-periodic Hamiltonian that can be solved using Floquet theory [43, 54, 55].

In this work, we extend previous methods to include the effects of hyperfine splitting during the optimization. Although we specifically calculate for diamond NV centers here, this method is generally adaptable and applicable to any such level structure. The goal is to create a shaped pulse that causes the state transfer  $|0\rangle$  to  $|-1\rangle$  simultaneously and with as high fidelity as possible for each of the  $m_I$  hyperfine levels. For an NV center ensemble, this results in a higher ODMR contrast than would be otherwise achievable by acting on only one  $m_I$  level. This approach is analogous to continuous wave methods driving multiple hyperfine lines previously described in the literature [56]. In order to explicitly account for the hyperfine splitting, it is necessary to modify the expression for the Fourier components of the Hamiltonian that make up the Floquet matrix. The Fourier components of the Hamiltonian are generally defined as

$$\hat{H}_n = \frac{1}{T} \int_0^T \exp(-in\Omega_f t) \hat{H}(t) dt,
 \tag{4}$$

where  $T = 2t_p$  is the periodicity of the Hamiltonian and  $\hat{H}(t)$  is the time-domain Hamiltonian that describes the system to be optimized. The nitrogen in an NV can be either  $^{14}\text{N}$  with  $I = 1$  (highest natural abundance) or  $^{15}\text{N}$  with  $I = 1/2$ , yielding either three or two hyperfine levels, respectively, as illustrated in Fig. 1(a). We assume hyperfine interaction between the  $^{14}\text{N}$  nuclear spins and the NV electron spins in the ensemble so that three hyperfine states are possible. The nuclear spins are assumed to be in a thermal state such that all  $m_I$  hyperfine levels are equally represented in the ensemble. The ODMR spectrum then contains three resonances separated by  $\delta_I = 2.16$  MHz, corresponding to the three hyperfine resonances  $m_I = -1, 0, 1$ . We also assume that the different NV electron spins do not interact and that the  $m_s = \pm 1$  levels are clearly split by a static magnetic bias field. A single set of three NV centers that each correspond to one of the hyperfine transitions can then be reasonably approximated as three independent two-level systems. The drift Hamiltonian thus has the form

$$\hat{\mathcal{H}}_0 = \sum_{k=1}^3 \frac{\omega_{0,k}}{2} \sigma_{z,k}, \quad (5)$$

where  $\hbar = 1$ ,  $\omega_{0,k}$  is the transition frequency of hyperfine transition  $k$ , and  $\sigma_{z,k}$  is a Pauli spin- $z$  matrix that is specific to transition  $k$ . Note that the above expression applies to any two-level defect with three equidistant hyperfine resonances that fulfills the underlying assumptions. The transition frequencies are related via  $\omega_{0,1} = \omega_{0,2} - \delta_I$  and  $\omega_{0,3} = \omega_{0,2} + \delta_I$ . Given that the states of the three two-level systems can be completely described by a single vector of length 6, the  $\sigma_{z,k}$ -matrices can also be represented by 6-by-6 matrices. (See Appendix A). The same is true of the  $\sigma_{x,k}$ - and  $\sigma_{y,k}$ -matrices. The control Hamiltonian describes the interaction between the control pulse of the form given in Eq. (2) and the three allowed transitions.

Assuming the control field is linearly polarized in the  $x$ -direction, which is perpendicular to the NV defect axis, the control Hamiltonian can be written in the form

$$\hat{\mathcal{H}}_c = \sum_{k=1}^3 \sigma_{x,k} [I(t) \cos(\omega_D t) + Q(t) \sin(\omega_D t)], \quad (6)$$

and the total Hamiltonian thus reads

$$\hat{\mathcal{H}}(t) = \sum_{k=1}^3 \left( \frac{\omega_{0,k}}{2} \sigma_{z,k} + \sigma_{x,k} [I(t) \cos(\omega_D t) + Q(t) \sin(\omega_D t)] \right). \quad (7)$$

We can simplify the rest of the calculations by working in a rotating frame given by the unitary rotation operator

$$\hat{R} = \exp \left( \sum_{k=1}^3 i\omega_D t \sigma_{z,k} / 2 \right), \quad (8)$$

which will commute with every term in  $\hat{\mathcal{H}}_c$  except for  $\sigma_{x,k}$ . More precisely,  $[\sigma_{z,k}, \sigma_{x,k'}] = 2i\sigma_{y,k}\delta_{k,k'}$  and  $[\sigma_{z,k}, \sigma_{y,k'}] = -2i\sigma_{x,k}\delta_{k,k'}$ .

The Baker-Campbell-Hausdorff lemma thus allows us to write

$$\hat{R}\hat{\mathcal{H}}_c\hat{R}^\dagger = \sum_{k=1}^3 (\sigma_{x,k} \cos(\omega_D t) + \sigma_{y,k} \sin(\omega_D t)) \times [I(t) \cos(\omega_D t) + Q(t) \sin(\omega_D t)]. \quad (9)$$

Using this expression and defining the detuning,  $\Delta = \omega_{0,2} - \omega_D$ , as the difference between the transition frequency of the central hyperfine transition,  $\omega_{0,2}$ , and the central driving frequency,  $\omega_D$ , we obtain the expression

$$\hat{\mathcal{H}}' = \sum_{k=1}^3 \left( \frac{\Delta + w_k \delta_I}{2} \sigma_{z,k} + (\sigma_{x,k} \cos(\omega_D t) + \sigma_{y,k} \sin(\omega_D t)) \times [I(t) \cos(\omega_D t) + Q(t) \sin(\omega_D t)] \right), \quad (10)$$

where  $w_1 = -1$ ,  $w_2 = 0$  and  $w_3 = 1$ . Expanding by using trigonometric relations, the above expression can be simplified by using the rotating wave approximation to eliminate the fast-oscillating terms

$$\hat{\mathcal{H}}' = \sum_{k=1}^3 \left( \frac{\Delta + w_k \delta_I}{2} \sigma_{z,k} + \frac{I(t)}{2} \sigma_{x,k} + \frac{Q(t)}{2} \sigma_{y,k} \right). \quad (11)$$

Combining Eq. (11) with Eq. (3) and inserted into Eq. (4), the Fourier components of the Hamiltonian become

$$\hat{\mathcal{H}}_n = \sum_{k=1}^3 \frac{1}{T} \int_0^T \exp(in\Omega_f t) \left( \frac{\Delta + w_k \delta_I}{2} \sigma_{z,k} + \sum_{j=1}^{N_f} [a_{jx} \sigma_{x,k} + a_{jy} \sigma_{y,k}] \sin(j\Omega_f t) \right) dt. \quad (12)$$

The above expression can be further simplified by using the exponential form of a sine and the integral form of a Kronecker delta. Doing so yields the final expression for the Fourier components of the Hamiltonian when the effects of hyperfine splitting are taken into account

$$\hat{\mathcal{H}}_n = \sum_{k=1}^3 \left( \frac{\Delta + w_k \delta_I}{2} \sigma_{z,k} \delta_{n,0} + \sum_{j=1}^{N_f} \frac{1}{2i} [a_{jx} \sigma_{x,k} + a_{jy} \sigma_{y,k}] \cdot [\delta_{n,j} - \delta_{-n,j}] \right). \quad (13)$$

We use Eq. (13) in the construction of the Floquet matrix for the computation of  $\hat{U}(t_p)$  and  $\frac{\partial \mathcal{F}_{\text{st}}}{\partial a_{j,k}}$  as part of the update step of the optimal control algorithm. We include the corresponding derivation for two hyperfine levels ( $^{15}\text{N}$  for NV centers) in the Supplementary Information. Control amplitude variations are included by multiplying the control amplitudes  $a_{jx}$ ,  $a_{jy}$  by the  $\alpha_i$ -value for the given defect in the representative ensemble.

In order to ensure the optimization of our control amplitudes converges while remaining within experimentally achievable limits, we include a penalty functional

$$\mathcal{F}_{\text{pen}} = -pt_p \sum_{j,k} a_{j,k}^2 \quad (14)$$

in our algorithm, applied at each update step. The penalty functional includes a specified penalty constant  $p > 0$  and scales with the control amplitudes. We optimize using the gradient of the sum of the penalty functional and the state transfer fidelity  $\mathcal{F}_{\text{tot}} = \mathcal{F}_{\text{pen}} + \mathcal{F}_{\text{st}}$ . After each update step, the maximum amplitude of the optimal control pulse is computed in units of Rabi frequency, and if it exceeds the maximum allowed Rabi frequency  $R_{\text{lim}}$ , the penalty constant is increased by a step

size  $\Delta p$ . If the maximum amplitude of the optimal control pulse does not exceed  $R_{\text{lim}}$ , the penalty constant is reduced by  $\Delta p$ .  $R_{\text{lim}}$  is one of the inputs to the algorithm and is limited by the maximum achievable experimental Rabi frequency  $R_{\text{max}}$ . This method also helps to prevent the algorithm from remaining in local maxima compared to optimizing without a penalty functional.

As a demonstration of the effect of explicitly including all three hyperfine levels in the optimization, Fig. 4 shows a series of simulated fidelity maps for a single NV subject to a flat  $\pi$ -pulse and optimal control pulses with and without including the hyperfine components. The fidelity of a  $|0\rangle$  to  $|-1\rangle$  state transfer is directly proportional to the resulting ODMR contrast  $C$  since the contrast will be maximal when all NV electron spins are transferred to the  $|-1\rangle$  state and minimal when left in the  $|0\rangle$  state. All three pulses are in the regime of  $R_{\text{lim}} < \delta_I$ . It is clear that the regular optimal control pulse has superior performance for a single hyperfine resonance. However, when considering the average of all three, the shaped pulse optimized while taking the effects of hyperfine splitting into account is significantly better, albeit within a narrower range of detuning. Fig. 4(f) indicates that the optimal control pulse including the hyperfine splitting in the optimization is capable of simultaneously performing state transfer using all three hyperfine levels with high fidelity. The narrow range of high fidelity dropping rapidly with detuning indicates that the optimal pulse will yield high contrast when applied with drive frequency  $\omega_D/2\pi$  close to any one of the three hyperfine resonances and low contrast when applied off-resonance. This behavior naturally translates to a high contrast and narrow resonance linewidth and thus higher sensitivity to magnetic field. As can be seen in Fig. 4(c,f), as  $\alpha_1$  is increased, the  $|0\rangle$  to  $|-1\rangle$  fidelity (i.e. ODMR contrast) further improves in the narrow range of high fidelity without significantly broadening the range of high fidelity. Therefore, we experimentally apply our optimal control pulses at higher MW power (i.e. greater  $\alpha$ ), selecting the power that results in the greatest ODMR slope.

## B. Optimization Details

All of our pulses were made using an initial value of the penalty constant  $p = 1$  and  $\Delta p = 0.05$ . They were optimized to perform a state transfer from  $|0\rangle$  to  $|-1\rangle$ . We used 150 update steps for all of the optimizations, as this was found to be sufficient to achieve convergence of  $\mathcal{F}_{\text{st}}$ . For the first 51 steps, the step size along the gradient was kept constant at  $\beta = 0.007$  and for the remaining steps, the optimal step size was determined using a line search. This was done to speed up the optimization without compromising the quality of the resulting optimal control pulses. We designed pulses using different values of  $R_{\text{lim}}$ ,  $t_p$  and the ranges  $\hat{\Delta}$  and  $\hat{\alpha}$  and tested them experimentally. We determined the maximum achievable experimental Rabi frequency in our

setup, i.e. the upper limit on the maximum allowed Rabi frequency  $R_{\text{lim}} \leq R_{\text{max}} = 3.2$  MHz. We therefore considered optimal control pulses generated within a range of  $0.8 \text{ MHz} \leq R_{\text{lim}} \leq R_{\text{max}}$ . The minimum value of  $t_p$  necessary to achieve improvements over a comparable flat pulse was limited by the need to apply sufficient energy to perform the desired state transfer. We set the lower limit of  $t_p$  to be at least twice the duration of a flat  $\pi$ -pulse with Rabi frequency equal to  $R_{\text{lim}}$ . The maximum value of  $t_p$  was limited by the  $T_2$  coherence time of a single NV. Based on this, we defined a range of  $t_p$  to generate testable optimized shaped pulses for as  $1.0 \mu\text{s} \leq t_p \leq 5.0 \mu\text{s}$ .

Although the possible values of detuning  $\Delta_i$  are in principle not limited, higher Rabi frequencies are required to compensate for higher levels of inhomogeneous broadening. Based on the considered values of  $R_{\text{lim}}$ , we therefore used  $\hat{\Delta}$  up to  $\pm 2$  MHz. The possible values of  $\alpha_i$  are similarly not limited in principle, but higher Rabi frequencies are required to compensate for higher levels of drive field inhomogeneity. We therefore chose to optimize up to  $\hat{\alpha} = 1 \pm 0.2$  relative control amplitude range.

Our initial  $a_{jk0}$  values were set using pseudorandom numbers within a range sufficient to yield a maximum Rabi frequency of the corresponding initial pulse  $R > R_{\text{lim}}$ . This was done in order to ensure that the optimization algorithm approached the region of allowed pulses from the outside, so that pulses utilizing  $R_{\text{lim}}$  were considered. For this work, the initial Rabi frequency was 2.8 times greater than the maximum allowed Rabi frequency.

## C. Experimental Setup

A schematic of our experimental setup is shown in Fig. 5(a). We used an off-the-shelf, optical-grade diamond (Element 6) with  $\sim 0.5$  ppb  $\text{NV}^-$  concentration, of dimensions  $5 \times 5 \times 1.2 \text{ mm}^3$ . For this diamond, we measured a  $T_2^*$ -limited linewidth of 0.75 MHz and determined  $T_1$ ,  $T_2$  and  $T_2^*$  times as 7.1 ms, 7.0  $\mu\text{s}$  and 0.44  $\mu\text{s}$  respectively, with a maximum achievable and ensemble-averaged Rabi frequency of  $R_{\text{max}} = 3.2$  MHz. A bias field of 2.9 mT aligned along one of the [111] crystallographic axes was applied by fixed permanent magnets in order to split the  $m_s = \pm 1$  levels. We addressed only the  $m_s = 0 \rightarrow m_s = -1$  transition to use an effective two-level system within the antenna's resonance linewidth of  $\sim 100$  MHz.

The diamond was optically pumped using a 532 nm solid state laser (DPSS, Cobolt Samba 1500). The linearly polarized beam was focused to a waist diameter of  $\approx 120 \mu\text{m}$  and coupled into the diamond at the Brewster-angle. We estimate a minimum ensemble size of  $1 \times 10^9$  NV centers in a volume of  $0.01 \text{ mm}^3$  within half of the  $1/e^2$  beam waist. The peak pump laser power we delivered to the diamond was 500 mW. This resulted in 84  $\mu\text{W}$  of red fluorescence escaping the front face of the diamond as measured by a large detector, of which we

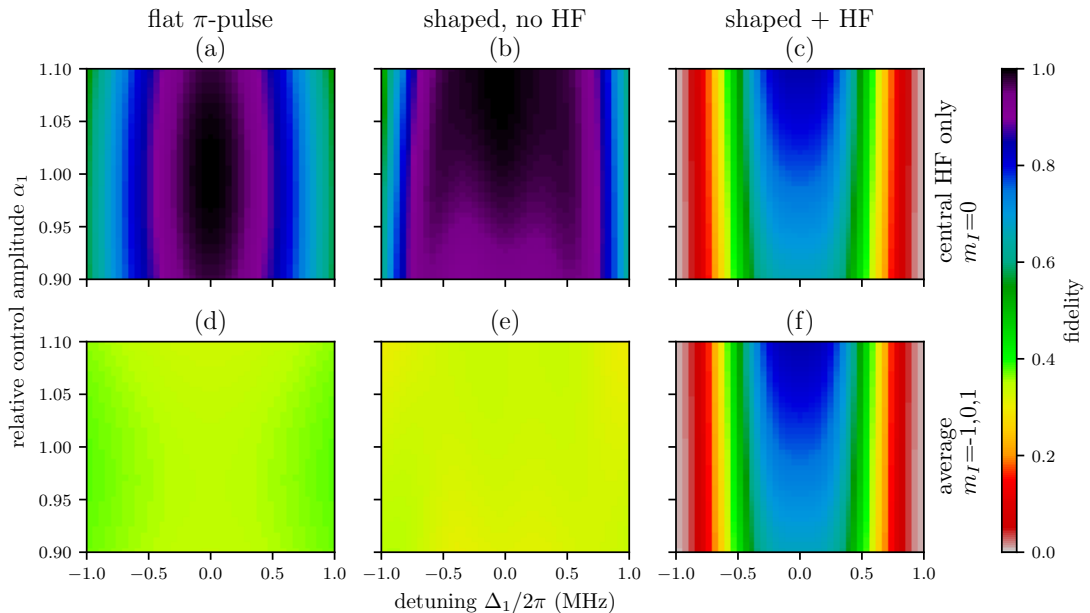


FIG. 4. Color online. Simulated maps of the state transfer fidelity (Eq. (1)) from  $|0\rangle$  to  $|-1\rangle$  for a single NV ( $i=1$ ) subject to (a,d) a flat ( $\pi$ -) pulse, (b, e) an optimized shaped pulse and (c, f) a shaped pulse optimized while taking all three hyperfine levels into account. The top plots (a, b, c) show the fidelity of the transfer experienced by the central hyperfine transition while the bottom plots (d, e, f) show the average of the transfer fidelities for each of the three hyperfine levels. Each point in the top plots is the fidelity for a single NV electron spin with the given values of  $\alpha_1$  and  $\Delta_1$ . Each point in the bottom plots is the average of the fidelities for three NV electron spins with the given value of  $\alpha_1$  and transition frequencies detuned by  $\Delta_1$ ,  $\Delta_1 + \delta_I$  and  $\Delta_1 - \delta_I$ , respectively, from the driving frequency. The flat pulse has a Rabi frequency of 1.4 MHz, and the optimal control pulses were both optimized using  $\hat{\Delta}/2\pi = \pm 1$  MHz detuning,  $\hat{\alpha} = 1 \pm 10\%$  amplitude variation,  $R_{\text{lim}} = 1.4$  MHz and a pulse duration  $t_p = 1.85 \mu\text{s}$ .

collected 9.1  $\mu\text{W}$  with the avalanche photodiode (Thorlabs APD120A) during measurement, producing an amplified analog voltage output  $V_{\text{fl}}$  sampled by an analog-to-digital converter (ADC, Gage Octopus CS8300) at 50 MHz. We amplitude-modulated our pump beam using an acousto-optic modulator (AOM, Isomet 532C-4) at  $f_{\text{AOM}} = 2.6$  MHz, allowing us to perform software lock-in detection to minimize noise in the electronic readout. A fraction of the pump beam was also sampled by a second detector (Thorlabs PDA10A) to provide a reference  $V_{\text{ref}}$  for common-mode noise rejection and spin readout, as described in the following section.

We generated the shaped optimal control MW pulses using an arbitrary waveform generator (AWG, Tektronix 5000), in-phase/quadrature (IQ) modulating a Stanford SG394 MW signal generator. The microwave output was amplified (Mini-Circuits ZHL-16W-43-S+) and delivered to the diamond using a near-field antenna based on a square split-ring design [57, 58]. This antenna was designed for uniformity of near-field intensity in a  $5 \times 5 \text{ mm}^2$  region centered on the diamond with a resonance at

approximately 2.8 GHz. Our AWG also controlled a switch (Minicircuits ZASWA-2-50DRA+) through which the AOM modulation drive was passed, allowing the pump laser beam to be both pulsed and amplitude modulated.

#### D. Pulse Sequencing and Readout

In our experiment, we measured the ODMR contrast  $C$ , which corresponds to the transfer of electron spin population from  $|0\rangle$  to  $|-1\rangle$  by the preceding MW control pulse.  $C$  is defined as the fractional change in fluorescence output in the initial period of a pump readout pulse [29, 34, 59] and was measured across an ODMR resonance feature by varying the microwave drive frequency  $\omega_D$ . We measured this change in fluorescence signal  $V_{\text{fl}}$  after application of either a shaped or flat microwave pulse, relative to the pump beam reference signal  $V_{\text{ref}}$ . We obtained  $C$  by integrating  $V_{\text{ref}} - V_{\text{fl}}$  over a time window  $t_w = [0.3, 2.7 \text{ ms}]$  from the start of each readout

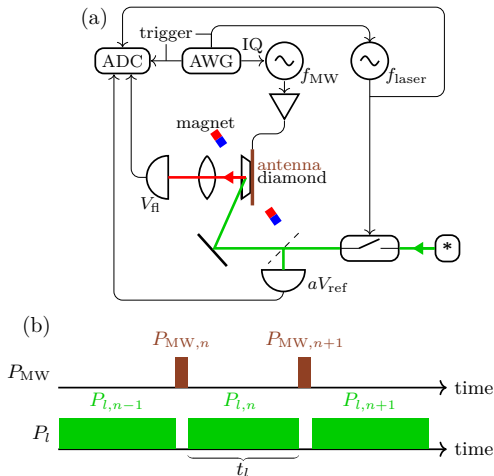


FIG. 5. Color online. (a) Schematic of our experimental setup. The pump laser was modulated by the AOM, at  $f_{\text{laser}} = 2.6$  MHz and controlled by the AWG. Microwave pulses were delivered to the diamond using a near-field antenna. The AWG provided IQ modulation to the signal generator to create the required control pulses. An ADC, synchronized with the AWG, digitized the analog AOM modulation signal, the signal from the APD that collected the diamond fluorescence  $V_{\text{fl}}$ , and the signal from an amplified photodetector that collected a small amount of the pump laser  $V_{\text{ref}}$  balanced with  $V_{\text{fl}}$ . (b) Pulsed ODMR sequence as applied in our measurements, showing the repeating sequence of pump laser pulses  $P_i$  and microwave pulses  $P_{\text{MW}}$ . This sequence was repeated continuously by the AWG.

pulse and converting the result into absolute units by a calibrated scaling factor (see Supplementary Information for full details). This subtraction method allowed us to reject both DC and higher-frequency ( $>$ kHz) common-mode noise originating from the laser on the readout signal within the integration window. Importantly, it also allowed us to measure the ensemble-averaged spin population transfer from every readout pulse, rather than measuring a reference with no microwave pulse on every second fluorescence readout, thus maximizing the detection scheme bandwidth. From  $C$  we also derived  $C' = 2\pi \frac{dC}{d\omega_D}$ , the change in contrast with microwave drive frequency, which provides a measure of the strength of response to environmental parameters, e.g. magnetic field or temperature.

Implementing the protocol shown in Fig. 5(b), we initialized the NV ensemble into the  $|0\rangle$  state using pump laser pulse  $P_{i,n-1}$  of duration  $t_i$ . The pump beam was then blocked by the AOM during application of microwave control pulse  $P_{\text{MW},n}$  of duration  $t_p$ . A subsequent pump pulse  $P_{i,n}$  of the same duration  $t_i$  was applied and the state read out via fluorescence emission. This pulse also acted to reinitialize the system back into

$|0\rangle$ , ready for the next  $P_{\text{MW},n+1}, P_{i,n+1}$  pulses to control, readout, and reinitialize the NV ensemble.

For direct comparison, we performed the same pulse sequence with the identical readout methods for  $C$  using either optimally shaped microwave pulses or standard flat pulses. We used the same method for calculating  $C$  throughout our measurements, to ensure accurate comparison between the different control pulses. To compare the optimal control pulse to the best possible flat pulse, we tested both single-frequency drive pulses of the form  $\cos(\omega t)$  and three-frequency drive pulses of the form  $\sum_{n \in \{0, \pm 1\}} \cos((\omega + n\delta_I)t + \phi_n)$  to drive multiple  $^{14}\text{N}$  hyperfine transitions [60]. The latter were generated using the AWG with randomized phases  $\phi_n$  for each ADC acquisition to eliminate time-dependent artifacts.

### III. RESULTS

#### A. Spin State Readout

Our previous measurements [61] demonstrated long optical reinitialization times, requiring tens of milliseconds of pump pulse duration to fully return the ensemble to the  $|0\rangle$  state along an approximately exponential decay. For the comparably sized ensemble in the experiments here, we observed similar exponential behavior with a time constant of  $\approx 1.4$  ms.

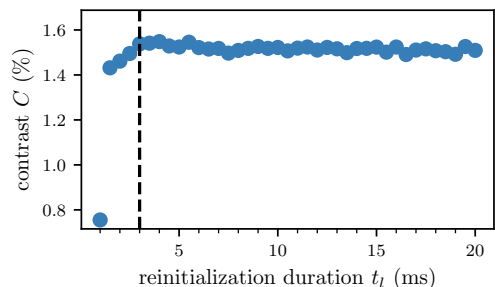


FIG. 6. Contrast as a function of pump laser pulse time  $t_i$ . Below 3 ms,  $t_i$  is too short to sufficiently reinitialize the ensemble, leading to a reduction in contrast  $C$  with shorter readout/reinitialization pump pulse duration  $t_i$ .

Waiting tens of milliseconds per readout would severely limit the bandwidth and sensitivity. We therefore first performed experiments varying the pump pulse duration to determine the shortest duration  $t_i$  necessary to avoid hysteresis effects, either from incomplete initialization or reionization delay during the series of readout pump pulses [62–64].

Fig. 6 shows the contrast  $C$  (recalibrated for each  $t_i$  as described in the Supplementary Information) as a function of pump readout/reinitialization pulse duration

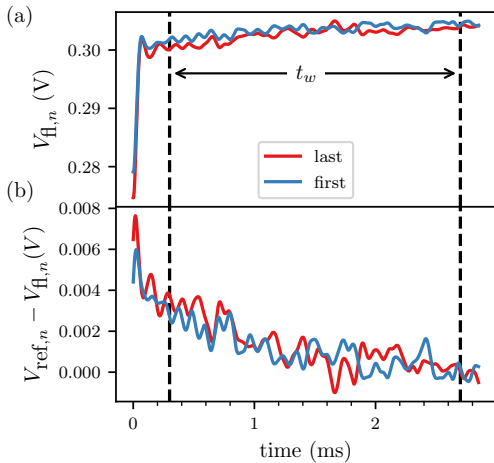


FIG. 7. Raw fluorescence readout signal  $V_{fl,n}$  and relative contrast  $C_{r,n}(t) = V_{ref,n} - V_{fl,n}$  for the first ( $n=1$ ) and last ( $n=110$ ) 3 ms readout pulse in a single acquisition of 110 readout sequences. No difference within the readout noise was observed at this readout duration, as would be expected from hysteresis effects arising from insufficient reinitialization of the ensemble. Note that the artifact due to AOM switch-on is not included in the integration window  $t_w$ .

$t_l < 20$  ms measured using an optimal control pulse. We observed  $C$  to increase with increasing  $t_l$  up to 3 ms, which corresponds to an increasing number of NV centers getting fully reinitialized into the  $|0\rangle$  state. For  $t_l > 3$  ms, we observed no further increase in  $C$  and negligible hysteresis effects in the fluorescence readout. The lack of hysteresis is supported by Fig. 7, comparing the raw fluorescence and relative contrast of the first and last individual readout pulses in a 110-pulse acquisition using  $t_l = 3$  ms.

We note that the fact we could achieve the same hysteresis-free behavior and similar contrast for a short 3 ms pump pulse as for one much longer is somewhat surprising given the Gaussian intensity profile of the pump beam. Due to the Gaussian pump beam profile, the NV centers at the low intensity periphery require more time to reinitialize back into the  $|0\rangle$  state. However, NV centers at the periphery also contribute far less to the overall fluorescence output and hence contrast  $C$  than those in the center of the pump beam. To demonstrate quantitatively how this mitigates hysteresis dynamics in our experiment, we implemented a simple physical model of the NV population dynamics.

Our model consists of a fixed NV density addressed by a radially (Gaussian-) varying laser beam intensity, with an NV at a distance  $r$  from the beam center receiving a pump intensity  $I(r)$ . We then solve a rate equation model for all NV centers [65, 66], from which we estimate

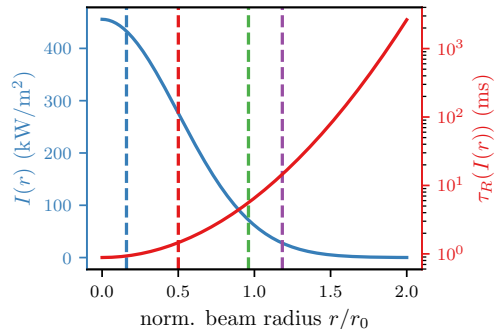


FIG. 8. Modelled variation in laser intensity  $I(r)$  and the exponential decay time  $\tau_R(I(r))$  of the spin polarization as a function of beam radius, relative to  $r_0$  the  $1/e^2$  beam width.  $\tau_R$  increases substantially in the lower intensity periphery of the beam. The four dashed lines show the profile radii chosen to represent different regimes of beam intensity for hysteresis simulation in Fig 9(a).

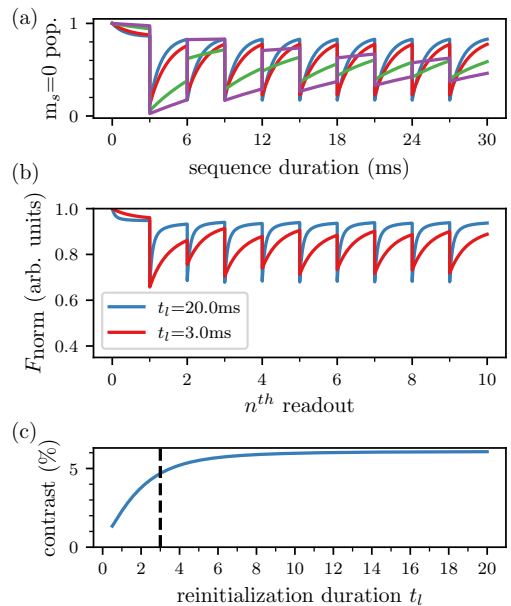


FIG. 9. (a) Simulated dynamics of the  $m_s=0$  population for NV centers receiving pump beam intensity  $I(r)$  at four different increasing values of  $r/r_0$  corresponding to Fig 8. The simulation is initialized in  $P(|0\rangle) = 1$  and evolved over ten sequences of reinitialization and ideal  $\pi$ -pulses as in Fig. 5(b). (b) The ensemble-averaged  $|0\rangle$  spin population from the simulation in (a), weighted by the radial distribution of fluorescence emission  $I(r)r$ . (c) The steady-state fluorescence contrast of the simulated ensemble as a function of  $t_l$ .

the relative fluorescence output and ensemble contrast  $C$ . We implement microwave pulses in the simulation as ideal  $\pi$ -pulses with instantaneous population transfer in the rate model between levels  $m_s=0$  to  $m_s=-1$ . Further details of the implementation of the model are given in the Supplementary Information.

In Fig. 8, we plot the estimated intensity  $I(r)$  and the simulated reinitialization time  $\tau_R(I(r))$ , the decay time of the electron spin polarization of the NV centers at  $r$ , as a function of beam radius  $r/r_0$ , where  $r_0$  represents the  $1/e^2$  beam width. From this simulation, it is clear that the pump duration used in our ODMR measurements  $t_l = 3$  ms corresponds to near complete reinitialization of the ensemble in  $r < 0.5r_0$ .

The simulated reinitialization behavior can be seen in Fig. 9(a), plotting the time evolution of the  $|0\rangle$  state population for the first 10 readout/MW pulses of length  $t_l = 3$  ms for 4 increasing values of  $r/r_0$ . The steady-state response to the microwave-laser sequence is reached when the pump is able to fully return the spin population to its value prior to the preceding microwave pulse. Below optical pump saturation, the amount by which the pump changes an NV center's spin population within  $t_l$  is linear with that NV center's contribution to the ensemble contrast  $C$ . For  $r/r_0 < 0.5$ , the steady-state response is reached immediately after the first microwave pulse, and contrast is negligibly reduced by the short reinitialization time  $t_l = 3$  ms. For  $r/r_0 > 0.5$ , hysteretic behavior is observed, where oscillations about the steady-state pulse response decay within the first  $\sim 10$  pulses. Once steady-state behavior is reached, the contribution to the ensemble contrast of these peripheral NV centers is reduced due to  $t_l$  being shorter than their reinitialization time  $\tau_R$ . Due to their weak fluorescence, the hysteretic behavior of the weakly-pumped NV centers outside of the  $r < 0.5r_0$  ensemble is a negligible part of the total signal, especially when considering averages of more than 100 recordings. This can be seen in Fig. 9(b), which shows the simulated total fluorescence emission within  $r < 2r_0$  as a function of time for readout pulses with duration  $t_l = 20$  ms and  $t_l = 3$  ms respectively. For the shorter pulse duration, the peripheral NV centers are not fully reinitialized, slightly reducing the total fluorescence emission at the end of a readout pulse and increasing the fluorescence at the beginning even after the steady-state response is reached. As the pump pulse duration  $t_l$  is reduced below 3 ms, the fraction of NV centers not fully reinitialized increases, resulting in a sharp reduction of the ensemble contrast. This behavior can be seen in Fig. 9(c) which qualitatively replicates our experimental data in Fig. 6.

The ability to rapidly read and reinitialize in this manner is an extremely useful result, since it gives a means to adequately control and read a large NV ensemble with pump pulses shorter than those required to fully reinitialize every fluorescing defect center. This significantly increases the measurement bandwidth for pulsed quantum sensing schemes, while still addressing a large number of defects as required to maximize sensitivity.

## B. ODMR Using Shaped Optimal Control Pulses

Using our optimal control algorithm including all 3 hyperfine levels for  $^{14}\text{N}$ , we first generated a series of shaped microwave pulses spanning the parameter space of  $\hat{\Delta}$  and  $\hat{\alpha}$ , the Rabi frequency limit  $R_{\text{lim}}$ , and the pulse duration  $t_p$ . Their performance was then tested experimentally to explore the limits of these parameters that yield high ODMR contrast  $C$ . We found that extending  $\hat{\Delta}$  and  $\hat{\alpha}$  beyond  $\pm 1$  MHz and  $\pm 10\%$  respectively had negligible impact, likely indicating that the real ensemble distribution in our setup was within these ranges. Having found that control pulses generated with parameters in the range of  $1.1 \text{ MHz} < R_{\text{lim}} < 2.4 \text{ MHz}$  and  $1 \mu\text{s} < t_p < 2 \mu\text{s}$  performed well, we experimentally searched the parameter space by measuring the ODMR spectrum using each shaped pulse and searching for the maximum slope  $C'$ . We also applied each optimal control pulse with experimental Rabi frequencies throughout the range  $R_{\text{lim}} \leq R_{\text{exp}} \leq R_{\text{max}}$ . We found the best-performing pulse generated with  $t_p = 1.85 \mu\text{s}$  and  $R_{\text{lim}} = 1.4 \text{ MHz}$ , with similar performance from larger  $R_{\text{lim}}$  up to 2 MHz at the same experimentally applied  $R_{\text{exp}}$ . The modulation components  $I(t)$  and  $Q(t)$  for this pulse are shown in Fig. 3(a), and the control amplitudes are given in the Supplementary Information.

The ODMR spectrum measured using our best-performing shaped control pulse is shown in Fig. 10(a). By differentiating the spectrum, we also show the ODMR slope  $C'$  in Fig. 10(b). Here, the largest possible slope is desired, since this produces the maximum response and highest sensitivity. For comparison, we plot in the same figure the ODMR spectrum obtained using the best-performing conventional flat three-frequency drive ( $\pi$ -) pulse. We found the maximum slope to be 11% higher for the shaped optimal control pulse than for this conventional flat pulse. Compared to the best-performing flat single-frequency drive ( $\pi$ -) pulse, we measured a significant improvement of 73%. This corresponds directly to the same factor of improvement in sensitivity.

We note that the durations of the flat and shaped pulses that delivered maximum slope were significantly different. This could potentially lead to the longer shaped pulse achieving higher performance simply by delivering more microwave energy over its duration. To ensure this was not the case, we compared the optimized pulse against single- and three-frequency drive flat pulses over an extended parameter space of pulse durations (up to  $t_p = 1.35 \mu\text{s}$ ) and applied Rabi frequency (up to  $R_{\text{exp}} = R_{\text{max}}$ ). This data is shown in Fig. 11 for single frequency drive and Fig. 12 for three-frequency drive. As can be seen from these figures, the shaped microwave pulse we generated using our optimal control methods always produced an ODMR slope far higher than that of any flat pulse. This was the case for any pulse length or microwave power, with the optima for the flat pulses reached well within experimental limits of  $R_{\text{max}}$  and  $t_p$ .

For our setup, we can estimate the shot-noise-limited

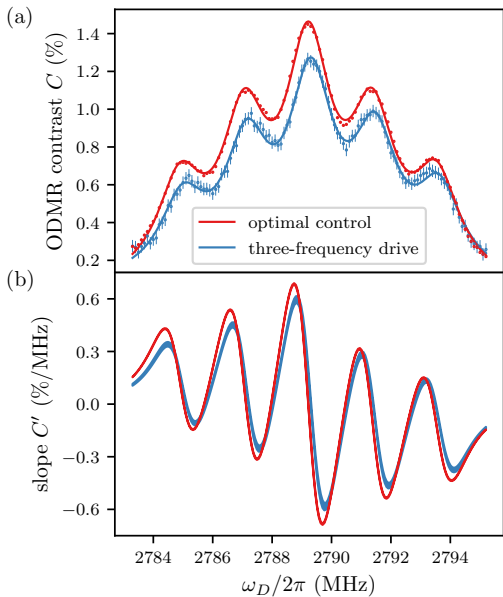


FIG. 10. Comparison of pulsed ODMR measurements using the most sensitive optimal control pulse and the most sensitive flat three-frequency drive pulse. The slope data shown in (b) is the slope of the fit to the ODMR data in (a) with uncertainty corresponding to drawn width.

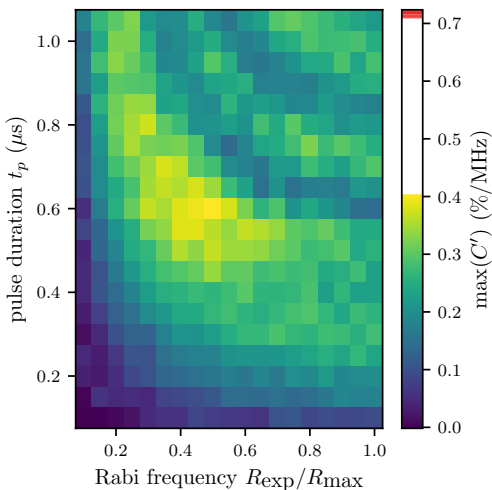


FIG. 11. The maximum ODMR slope  $C'$  measured for flat single-frequency drive pulses over the relevant parameter space of applied Rabi frequency  $R_{\text{exp}}$  and duration  $t_p$ . The red stripe in the colorbar shows the maximum ODMR slope of the best optimal control pulse from Fig. 10.

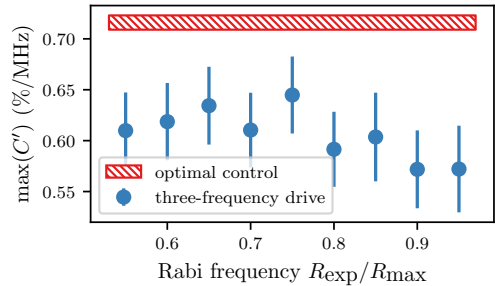


FIG. 12. Maximum ODMR slope  $C'$  for three-frequency drive pulses of the best-performing duration  $t_p$  for the given Rabi frequency  $R_{\text{exp}}$ , compared to the best-performing optimal control pulse. The error bars of the three-frequency drive data and the y-range of the optimal control pulse data represent  $1\sigma$  uncertainty. The data covering the full parameter space in duration  $t_p$  and Rabi frequency  $R_{\text{exp}}$  are shown in the Supplementary Information.

sensitivity using the expression derived in Appendix B:

$$\eta \approx \frac{\sqrt{2t_R t_l}}{\gamma_e C' \tau_R (1 - e^{-t_R/\tau_R}) \sqrt{R_0}}, \quad (15)$$

where we take into account the readout time  $t_R$  (the duration of the interval  $t_w$ , in our case  $t_w = [0.3, 2.7 \text{ ms}] \Rightarrow t_R = 2.4 \text{ ms}$ ), reinitialization time  $t_l$ , reinitialization decay constant  $\tau_R$ , photon detection rate  $R_0$ , electron gyromagnetic ratio  $\gamma_e$ , and measured contrast slope  $C'$ . For our setup applying the optimal control pulse, we estimate  $\eta \approx 10 \text{ nT}/\sqrt{\text{Hz}}$ . Although this is lower than state of the art figures reported elsewhere for magnetic field sensing with NV center ensembles, we note that our setup is not optimized for sensitivity due to the standard-grade diamond with low NV concentration we use and our APD detector with small detection area.

#### IV. CONCLUSION

In this work, we demonstrate that a large ensemble of solid state defects in a macroscopic sample can be manipulated and coherently controlled in a manner beneficial for quantum sensing. We demonstrate this for an ensemble of NV centers in diamond through the use of shaped microwave pulses generated using Floquet theory and optimal control methods. Due to the scaling of sensitivity with the number of defects, such large ensembles are key for quantum sensing applications, either using NV centers or other solid state defects. Our overall NV ensemble volume within half of the estimated Gaussian beam width ( $\approx 1 \times 10^9$  NV centers in a  $\approx 0.01 \text{ mm}^3$  volume) was much larger than NV ensembles previously studied and reported in the literature using optimal control methods [33, 43, 46–49].

By including the  $^{14}\text{N}$  hyperfine interaction in our optimization, we demonstrate an 11% enhancement in ODMR slope with an optimally shaped pulse when compared to the best alternative three-frequency drive flat ( $\pi^-$ ) pulses and a 78% improvement over standard single-frequency drive flat ( $\pi^-$ ) pulses most commonly used for coherent control in the literature. These enhancements in ODMR slope are directly equivalent to the same factor of sensitivity improvement when used in an applied sensing scheme. This significant improvement offers potential for wider impact for DC/low-frequency sensing, for example in precision measurement of slowly varying temperature where ensemble probe bandwidth limitations imposed by the shaped optimal control pulse and readout/reinitialization pulse durations would be less constraining.

We estimate a shot noise-limited sensitivity of  $10\text{nT}/\sqrt{\text{Hz}}$  using our setup, while noting that neither the diamond we use nor our detection apparatus were optimized for sensitivity at this time. Our method is not specific to the apparatus we used and could be applied equally well to a sensitivity-optimized setup, for example using an isotopically purified diamond with optimized density of NV centers. By measuring the ODMR contrast by referring to the signal from an additional photodetector, we were able to reject more of the laser technical noise while maximizing the number of contrast measurements we could achieve as compared to alternative time domain noise rejection methods [34].

Through simulation of the readout and reinitialization dynamics of the defect ensemble, we show that although tens of milliseconds are required to fully reinitialize all NV centers contributing to the fluorescence signal, a significantly shorter pump pulse can address and reinitialize the  $r < 0.5r_0$  ensemble which dominates the fluorescence. By demonstrating consistent contrast measurements free of hysteresis, we show that these NV centers can be addressed and controlled reliably. Further work is required to fully understand the dynamics of the system caused by the distribution of pump light in the diamond. However, our measurements suggest the primary limiting factor on the readout is the Gaussian shape of the pump beam, hinting at considerable future improvement using a non-Gaussian beam profile.

The shaped MW pulses we generate in this work likely represent local maxima of performance in a wide parameter space. We consider it very likely that advances in methods for optimization as well as experimental improvements could provide even better solutions in future. A particular flaw is the assumption of a Gaussian distribution for detuning and a flat distribution for control field intensity, which possibly are poor representations of the actual properties of our ensemble. A route forward may be to use experimental feedback in the optimization algorithm. This would be simplified by producing a more homogeneous microwave field, increasing the applied Rabi frequency, and using alternative pump beam profiles to improve uniformity of initialization and readout. Addi-

tionally, in this work we optimize for state transfer  $|0\rangle$  to  $|-1\rangle$ , which aims to maximize contrast  $C$ . By instead explicitly optimizing for the change in contrast in response to the control field (the slope  $C'$  in our results above), optimal control pulses with greater sensitivity could be generated.

Our work represents an important step in the direction of using optimal control and other techniques widely used in nuclear magnetic- and electron spin- resonance experiments to explore the physics of new systems suitable for quantum sensing. These techniques can be adapted not only to diamond but also to other defects in both bulk and 2D quantum materials [67]. Using control pulses shaped by optimal control methods, which could be either microwaves, optical fields or some other means, offers the best route to reach the ultimate  $T_2^*$ -limited sensitivity for any suitable quantum system.

## V. ACKNOWLEDGEMENTS

The work presented here was funded by the Novo Nordisk foundation through the synergy grant bioQ and the bigQ Center funded by the Danish National Research Foundation (DNRF).

### A. SPIN MATRICES

Below are shown the 6-by-6 matrix representations of the Pauli spin matrices that are each specific to one of the three nitrogen-14 hyperfine transitions.

$$\sigma_{z,1} = \begin{pmatrix} 1 & 0 & 0 & 0 & 0 & 0 \\ 0 & -1 & 0 & 0 & 0 & 0 \\ 0 & 0 & 0 & 0 & 0 & 0 \\ 0 & 0 & 0 & 0 & 0 & 0 \\ 0 & 0 & 0 & 0 & 0 & 0 \\ 0 & 0 & 0 & 0 & 0 & 0 \end{pmatrix}, \sigma_{z,2} = \begin{pmatrix} 0 & 0 & 0 & 0 & 0 & 0 \\ 0 & 0 & 0 & 0 & 0 & 0 \\ 0 & 0 & 1 & 0 & 0 & 0 \\ 0 & 0 & 0 & -1 & 0 & 0 \\ 0 & 0 & 0 & 0 & 0 & 0 \\ 0 & 0 & 0 & 0 & 0 & 0 \end{pmatrix} \quad (16)$$

$$\sigma_{z,3} = \begin{pmatrix} 0 & 0 & 0 & 0 & 0 & 0 \\ 0 & 0 & 0 & 0 & 0 & 0 \\ 0 & 0 & 0 & 0 & 0 & 0 \\ 0 & 0 & 0 & 0 & 0 & 0 \\ 0 & 0 & 0 & 1 & 0 & 0 \\ 0 & 0 & 0 & 0 & -1 & 0 \end{pmatrix}, \sigma_{x,1} = \begin{pmatrix} 0 & 1 & 0 & 0 & 0 & 0 \\ 1 & 0 & 0 & 0 & 0 & 0 \\ 0 & 0 & 0 & 0 & 0 & 0 \\ 0 & 0 & 0 & 0 & 0 & 0 \\ 0 & 0 & 0 & 0 & 0 & 0 \\ 0 & 0 & 0 & 0 & 0 & 0 \end{pmatrix} \quad (17)$$

$$\sigma_{x,2} = \begin{pmatrix} 0 & 0 & 0 & 0 & 0 & 0 \\ 0 & 0 & 0 & 0 & 0 & 0 \\ 0 & 0 & 1 & 0 & 0 & 0 \\ 0 & 0 & 0 & 0 & 0 & 0 \\ 0 & 0 & 0 & 0 & 0 & 0 \\ 0 & 0 & 0 & 0 & 0 & 0 \end{pmatrix}, \sigma_{x,3} = \begin{pmatrix} 0 & 0 & 0 & 0 & 0 & 0 \\ 0 & 0 & 0 & 0 & 0 & 0 \\ 0 & 0 & 0 & 0 & 0 & 0 \\ 0 & 0 & 0 & 0 & 0 & 0 \\ 0 & 0 & 0 & 0 & 1 & 0 \\ 0 & 0 & 0 & 0 & 0 & 1 \end{pmatrix} \quad (18)$$

$$\sigma_{y,1} = \begin{pmatrix} 0 & -i & 0 & 0 & 0 & 0 \\ i & 0 & 0 & 0 & 0 & 0 \\ 0 & 0 & 0 & 0 & 0 & 0 \\ 0 & 0 & 0 & 0 & 0 & 0 \\ 0 & 0 & 0 & 0 & 0 & 0 \\ 0 & 0 & 0 & 0 & 0 & 0 \end{pmatrix}, \sigma_{y,2} = \begin{pmatrix} 0 & 0 & 0 & 0 & 0 & 0 \\ 0 & 0 & 0 & 0 & 0 & 0 \\ 0 & 0 & -i & 0 & 0 & 0 \\ 0 & 0 & 0 & i & 0 & 0 \\ 0 & 0 & 0 & 0 & 0 & 0 \\ 0 & 0 & 0 & 0 & 0 & 0 \end{pmatrix} \quad (19)$$

$$\sigma_{y,3} = \begin{pmatrix} 0 & 0 & 0 & 0 & 0 & 0 \\ 0 & 0 & 0 & 0 & 0 & 0 \\ 0 & 0 & 0 & 0 & 0 & 0 \\ 0 & 0 & 0 & 0 & 0 & 0 \\ 0 & 0 & 0 & 0 & -i & 0 \\ 0 & 0 & 0 & 0 & i & 0 \end{pmatrix} \quad (20)$$

## B. ESTIMATION OF SHOT NOISE-LIMITED SENSITIVITY

Shot noise-limited sensitivity estimation is typically [29, 60] similar to

$$\eta \approx \frac{1}{\gamma_e \sqrt{RC'}}$$

with the electron gyromagnetic ratio  $\gamma_e$ , the photon detection rate  $R$  and the (in this case empirically measured) ODMR slope  $C' = 2\pi \frac{dC}{d\omega_D}$ . This assumes that each collected photon adds the same amount of information, which is the case in a typical pulsed detection setup where the readout time  $t_R$  is much shorter than the to-

tal reinitialization time  $t_l$ , and the contrast barely decays during  $t_R$ . We therefore include a factor representing the mean information collected per photon

$$\frac{1}{t_R} \int_0^{t_R} e^{-t/\tau_R} dt = \frac{\tau_R(1 - e^{-t_R/\tau_R})}{t_R}$$

with  $\tau_R$  as the decay time. We additionally modify  $R$  for clarity, in terms of the maximum photon collection rate at a peak of the pump beam modulation  $R_0$ ,  $R = R_0 t_R / 2t_l$ , where the duration of the MW pulse is neglected, and the 1/2 results from the amplitude modulation. In all, we obtain

$$\eta \approx \frac{\sqrt{2t_R t_l}}{\gamma_e C' \tau_R (1 - e^{-t_R/\tau_R}) \sqrt{R_0}}.$$

- 
- [1] T. Schröder, S. L. Mouradian, J. Zheng, M. E. Trusheim, M. Walsh, E. H. Chen, L. Li, I. Bayn, and D. Englund. Quantum nanophotonics in diamond. *J. Opt. Soc. Am. B*, 33(4):B65–B83, 2016.
- [2] J. H. N. Loubser and J. A. Van Wyk. Electron spin resonance in the study of diamond. *Rep. Prog. Phys.*, 41(8):1201–1248, 1978.
- [3] J. M. Taylor, P. Cappellaro, L. Childress, L. Jiang, D. Budker, P. R. Hemmer, A. Yacoby, R. Walsworth, and M. D. Lukin. High-sensitivity diamond magnetometer with nanoscale resolution. *Nat. Phys.*, 4(10):810–816, 2008.
- [4] Z.-H. Wang, G. de Lange, D. Risté, R. Hanson, and V. V. Dobrovitski. Comparison of dynamical decoupling protocols for a nitrogen-vacancy center in diamond. *Phys. Rev. B*, 85(15):155204, 2012.
- [5] D. Farfurnik, A. Jarmola, L. M. Pham, Z. H. Wang, V. V. Dobrovitski, R. L. Walsworth, D. Budker, and N. Bar-Gill. Improving the coherence properties of solid-state spin ensembles via optimized dynamical decoupling. *Proc. SPIE*, 9900:99000N, 2016.
- [6] D. Farfurnik, A. Jarmola, D. Budker, and N. Bar-Gill. Spin ensemble-based AC magnetometry using concatenated dynamical decoupling at low temperatures. *J. Opt. (United Kingdom)*, 20(2):024008, 2018.
- [7] G. T. Genov, Y. Ben-Shalom, F. Jelezko, A. Retzker, and N. Bar-Gill. Efficient and robust signal sensing by sequences of adiabatic chirped pulses. *Phys. Rev. Res.*, 2(3):033216, aug 2020.
- [8] F. Dolde, H. Fedder, M. W. Doherty, F. Rempp, G. Balasubramanian, F. Reinhard, F. Jelezko, and J. Wrachtrup. Sensing electric fields using single diamond spins. *Nat. Phys.*, 7(6):459–463, 2011.
- [9] P. Neumann et al. High-Precision Nanoscale Temperature Sensing Using Single Defects in Diamond. *Nano Lett.*, 13(6):2738–2742, 2013.
- [10] T. Delord, L. Nicolas, M. Bodini, and G. Hétet. Diamonds levitating in a Paul trap under vacuum : Measurements of laser-induced heating via NV center thermometry. *Appl. Phys. Lett.*, 111(1):013101, 2017.
- [11] M. W. Doherty et al. Electronic properties and metrology applications of the diamond  $\text{nv}^-$  center under pressure. *Phys. Rev. Lett.*, 112(4):047601, 2014.
- [12] I. Gross et al. Real-space imaging of non-collinear antiferromagnetic order with a single-spin magnetometer. *Nature*, 549(7671):252–256, 2017.
- [13] L. Thiel, Z. Wang, M. A. Tschudin, D. Rohner, I. Gutiérrez-Lezama, N. Ubrig, M. Gibertini, E. Gianini, A. F. Morpurgo, and P. Maletinsky. Probing magnetism in 2d materials at the nanoscale with single-spin microscopy. *Science*, 364(6444):973–976, 2019.
- [14] T. Staudacher, F. Shi, S. Pezzagna, J. Meijer, J. Du, C. A. Meriles, F. Reinhard, and J. Wrachtrup. Nuclear Magnetic Resonance Spectroscopy on a (5-Nanometer)<sup>3</sup> Sample Volume. *Science*, 339(6119):561–563, 2013.
- [15] I. Lovchinsky et al. Nuclear magnetic resonance detection and spectroscopy of single proteins using quantum logic. *Science*, 351(6275):836–842, 2016.
- [16] R. Schirhagl, K. Chang, M. Loretz, and C. L. Degen. Nitrogen-Vacancy Centers in Diamond: Nanoscale Sensors for Physics and Biology. *Annu. Rev. Phys. Chem.*, 65(1):83–105, 2014.
- [17] D. Le Sage, K. Arai, D. R. Glenn, S. J. DeVience, L. M. Pham, L. Rahn-Lee, M. D. Lukin, A. Yacoby, A. Komeili, and R. L. Walsworth. Optical magnetic imaging of living cells. *Nature*, 496(7446):486–489, 2013.
- [18] J. F. Barry, M. J. Turner, J. M. Schloss, D. R. Glenn, Y. Song, M. D. Lukin, H. Park, and R. L. Walsworth. Optical magnetic detection of single-neuron action potentials using quantum defects in diamond. *Proc. Nat. Acad. Sci. USA*, 113(49):14133–14138, 2016.
- [19] F. Gorrini, R. Giri, C. E. Avalos, S. Tambalo, S. Manucci, L. Basso, and N. Bazzanella. Fast and sensitive detection of paramagnetic species using coupled charge and spin dynamics in strongly fluorescent nanodiamonds. *ACS Appl. Mat. & Interfaces*, 11(27):24412–24422, 2019.
- [20] G. Kucsko, P. C. Maurer, N. Y. Yao, M. Kubo, H. J. Noh, P. K. Lo, H. Park, and M. D. Lukin. Nanometre-scale thermometry in a living cell. *Nature*, 500(7460):54–58, 2013.
- [21] M. Fujiwara et al. Real-time nanodiamond thermometry probing in vivo thermogenic responses. *Sci. Adv.*, 6(37):9636, 2020.

- [22] J. L. Webb et al. Optimization of a diamond nitrogen vacancy centre magnetometer for sensing of biological signals. *Frontiers Phys.*, 8:522536, 2020.
- [23] P. Rembold, N. Oshnik, M. M. Müller, S. Montangero, T. Calarco, and E. Neu. Introduction to quantum optimal control for quantum sensing with nitrogen-vacancy centers in diamond. *AVS Quant. Sci.*, 2(2):024701, 2020.
- [24] F. Jelezko, T. Gaebel, I. Popa, A. Gruber, and J. Wrachtrup. Observation of Coherent Oscillations in a Single Electron Spin. *Phys. Rev. Lett.*, 92(7):1–4, 2004.
- [25] F. Jelezko and J. Wrachtrup. Single defect centres in diamond: A review. *Physica Status Solidi A*, 203(13):3207–3225, 2006.
- [26] A. M. Wojciechowski, M. Karadas, C. Osterkamp, S. Jankuhn, J. Meijer, F. Jelezko, A. Huck, and U. L. Andersen. Precision temperature sensing in the presence of magnetic field noise and vice-versa using nitrogen-vacancy centers in diamond. *Appl. Phys. Lett.*, 113(1):013502, 2018.
- [27] Christian Osterkamp, Martin Mangold, Johannes Lang, Priyadharshini Balasubramanian, Tokuyuki Teraji, Boris Naydenov, and Fedor Jelezko. Engineering preferentially-aligned nitrogen-vacancy centre ensembles in cvd grown diamond. *Sci. Reports*, 9(1):1–7, 2019.
- [28] I. Fescenko, A. Jarmola, I. Savukov, P. Kehayias, J. Smits, J. Damron, N. Ristoff, N. Mosavian, and V. M. Acosta. Diamond magnetometer enhanced by ferrite flux concentrators. *Phys. Rev. Res.*, 2(2):023394, 2020.
- [29] A. Dréau, M. Lesik, L. Rondin, P. Spinicelli, O. Arcizet, J. F. Roch, and V. Jacques. Avoiding power broadening in optically detected magnetic resonance of single NV defects for enhanced dc magnetic field sensitivity. *Phys. Rev. B*, 84(19):1–8, 2011.
- [30] M. Alkahtani, J. Lang, B. Naydenov, F. Jelezko, and P. Hemmer. Growth of high-purity low-strain fluorescent nanodiamonds. *ACS Photonics*, 6(5):1266–1271, 2019.
- [31] J. F. Barry, J. M. Schloss, E. Bauch, M. J. Turner, C. A. Hart, L. M. Pham, and R. L. Walsworth. Sensitivity Optimization for NV-Diamond Magnetometry. *Rev. Mod. Phys.*, 92(1):015004, 2020.
- [32] K. Arai, J. Lee, C. Belthangady, D. R. Glenn, H. Zhang, and R. L. Walsworth. Geometric phase magnetometry using a solid-state spin. *Nat. Comm.*, 9(1):4996, 2018.
- [33] T. Nöbauer, A. Angerer, B. Bartels, M. Trupke, S. Rotter, J. Schmiedmayer, F. Mintert, and J. Majer. Smooth Optimal Quantum Control for Robust Solid-State Spin Magnetometry. *Phys. Rev. Lett.*, 115(19):190801, 2015.
- [34] T. Wolf, P. Neumann, K. Nakamura, H. Sumiya, T. Ohshima, J. Isoya, and J. Wrachtrup. Subpicotesla diamond magnetometry. *Phys. Rev. X*, 5(4):1–10, 2015.
- [35] D. Suter and F. Jelezko. Single-spin magnetic resonance in the nitrogen-vacancy center of diamond. *Prog. NMR Spectroscopy*, 98-99:50–62, 2017.
- [36] C. Müller et al. Nuclear magnetic resonance spectroscopy with single spin sensitivity. *Nat. Comm.*, 5(1):1–2, 2014.
- [37] D. Budker. Extreme nuclear magnetic resonance: Zero field, single spins, dark matter. . . . *Journal of Magnetic Resonance*, 306:66–68, 2019.
- [38] A. Gruber, A. Dräbenstedt, C. Tietz, L. Fleury, J. Wrachtrup, and C. von Borczyskowski. Scanning Confocal Optical Microscopy and Magnetic Resonance on Single Defect Centers. *Science*, 276(5321):2012–2014, 1997.
- [39] G. Balasubramanian et al. Ultralong spin coherence time in isotopically engineered diamond. *Nat. Mat.*, 8(5):383–387, 2009.
- [40] P. Balasubramanian, C. Osterkamp, Y. Chen, X. Chen, T. Teraji, E. Wu, B. Naydenov, and F. Jelezko. dc magnetometry with engineered nitrogen-vacancy spin ensembles in diamond. *Nano Lett.*, 19(9):6681–6686, 2019.
- [41] F. T. Charnock and T. A. Kennedy. Combined optical and microwave approach for performing quantum spin operations on the nitrogen-vacancy center in diamond. *Phys. Rev. B*, 64(4):041201, 2001.
- [42] A. Horsley, P. Appel, J. Wolters, J. Achard, A. Tallaire, P. Maletinsky, and P. Treutlein. Microwave device characterization using a widefield diamond microscope. *Phys. Rev. Appl.*, 10(4):044039, 2018.
- [43] B. Bartels and F. Mintert. Smooth optimal control with Floquet theory. *Phys. Rev. A*, 88(5):1–7, 2013.
- [44] N. Khaneja, T. Reiss, C. Kehlet, T. Schulte-Herbrüggen, and S. J. Glaser. Optimal control of coupled spin dynamics: Design of NMR pulse sequences by gradient ascent algorithms. *J. Magnetic Resonance*, 172(2):296–305, 2005.
- [45] C. Brif, R. Chakrabarti, and H. Rabitz. Control of quantum phenomena: past, present and future. *New J. Phys.*, 12(7):075008, 2010.
- [46] B. Bartels. *Smooth Optimal Control of Coherent Quantum Dynamics*. PhD thesis, Albert-Ludwigs-Universität Freiburg, 2015.
- [47] F. Ziem, M. Garsi, H. Fedder, and J. Wrachtrup. Quantitative nanoscale MRI with a wide field of view. *Scientific Reports*, 9(1), aug 2019.
- [48] P. Konzelmann et al. Robust and efficient quantum optimal control of spin probes in a complex (biological) environment. Towards sensing of fast temperature fluctuations. *New J. Phys.*, 20(12):1–29, 2018.
- [49] L. Dong, H. Liang, C. K. Duan, Z. Wang, Y. Li, X. Rong, and J. Du. Optimal control of a spin bath. *Phys. Rev. A*, 99(1):1–6, 2019.
- [50] F. Dolde et al. High-fidelity spin entanglement using optimal control. *Nat. Comm.*, 5(1):3371, 2014.
- [51] J. L. Webb, J. D. Clement, L. Troise, S. Ahmadi, G. J. Johansen, A. Huck, and U. L. Andersen. Nanotesla sensitivity magnetic field sensing using a compact diamond nitrogen-vacancy magnetometer. *Appl. Phys. Lett.*, 114(23):231103, 2019.
- [52] F. Poggiali, P. Cappellaro, and N. Fabbri. Optimal Control for One-Quibit Quantum Sensing. *Phys. Rev. X*, 8(2):021059, 2018.
- [53] T. E. Skinner, T. O. Reiss, B. Luy, N. Khaneja, and S. J. Glaser. Application of optimal control theory to the design of broadband excitation pulses for high-resolution NMR. *J. Magnetic Resonance*, 163(1):8–15, 2003.
- [54] G. Goelman, S. Vega, and D. B. Zax. Design of broadband propagators in two-level systems. *Physical Review A*, 39(11):5725–43, 1989.
- [55] T. E. Skinner and N. I. Gershenzon. Optimal control design of pulse shapes as analytic functions. *J. Magnetic Resonance*, 204(2):248–255, 2010.
- [56] H. A. R. El-Ella, S. Ahmadi, A. M. Wojciechowski, A. Huck, and U. L. Andersen. Optimised frequency modulation for continuous-wave optical magnetic resonance sensing using nitrogen-vacancy ensembles. *Opt. Express*, 25(13):14809–14821, 2017.

- [57] S. Ahmadi. *Continuous-Wave Magnetic Field Sensing with Nitrogen-Vacancy Centers in Diamond*. PhD thesis, Technical University of Denmark, 2018.
- [58] A. Genc and R. Baktur. A tunable Bandpass Filter Based on varactor loaded Split Ring Resonators. *Microwave Opt. Tech. Lett.*, 51(10):2394–2396, 2009.
- [59] E. V. Levine, M. J. Turner, P. Kehayias, C. A. Hart, N. Langellier, R. Trubko, D. R. Glenn, R. R. Fu, and R. L. Walsworth. Principles and techniques of the quantum diamond microscope. *Nanophotonics*, 8(11):1945–1973, 2019.
- [60] H. A. R. El-Ella, S. Ahmadi, A. M. Wojciechowski, A. Huck, and U. L. Andersen. Optimised frequency modulation for continuous-wave optical magnetic resonance sensing using nitrogen-vacancy ensembles. *Opt. Express*, 25(13):14809, 2017.
- [61] J. L. Webb et al. Optimization of a diamond nitrogen vacancy centre magnetometer for sensing of biological signals. *Frontiers Phys.*, 8:430, 2020.
- [62] R. Giri, F. Gorrini, C. Dorigoni, C. E. Avalos, M. Cazanelli, S. Tambalo, and A. Bifone. Coupled charge and spin dynamics in high-density ensembles of nitrogen-vacancy centers in diamond. *Phys. Rev. B*, 98(4):045401, 2018.
- [63] N. B. Manson and J. P. Harrison. Photo-ionization of the nitrogen-vacancy center in diamond. *Sci. Direct*, 14(10):1705–1710, 2005.
- [64] N. Aslam, G. Waldherr, P. Neumann, F. Jelezko, and J. Wrachtrup. Photo-induced ionization dynamics of the nitrogen vacancy defect in diamond investigated by single-shot charge state detection. *New J. Phys.*, 15(1):013064, 2013.
- [65] L. Robledo, H. Bernien, T. van der Sar, and R. Hanson. Spin dynamics in the optical cycle of single nitrogen-vacancy centres in diamond. *New J. Phys.*, 13(2):025013, 2011.
- [66] Y. Dumeige et al. Infrared laser magnetometry with a NV doped diamond intracavity etalon. *Opt. Express*, 27(2):1706.
- [67] A. Gottscholl et al. Initialization and read-out of intrinsic spin defects in a van der Waals crystal at room temperature. *Nat. Mat.*, 19(May):540–545, 2020.

## 5.3 Supplementary Information

## SUPPLEMENTARY INFORMATION

### A. Measurement of Readout Contrast

As shown in the main text Fig. 5, we recorded lock-in demodulated fluorescence  $V_{\text{fl}}(t)$  and balanced reference  $V_{\text{ref}}(t)$  signals with each readout sequence. The balancing of the reference signal was such that  $V_{\text{ref}}$  was rescaled to equal the fluorescence at the end of the laser readout pulse:  $V_{\text{ref}}(t_l) = V_{\text{fl}}(t_l)$ . We defined the readout contrast as  $C_r \equiv \sum_{t \in t_w} (V_{\text{ref}}(t) - V_{\text{fl}}(t))$  where the difference between the curves was summed over the samples in a window of time  $t_w$ , which is bounded by the black dashed lines in Fig. 1(a). The bounds of  $t_w$  were chosen to avoid the artifacts of the AOM switching on/off combined with the lock-in demodulation.

The contrast in a pulsed NV center readout scheme is generally defined as the difference in fluorescence output  $V_{\text{fl}}(t)$  with (MW on,  $V_{\text{fl,on}}(t)$ ) or without (MW off,  $V_{\text{fl,off}}(t)$ ) a preceding microwave pulse (for example, see main text ref [28]). It can be reported as the area between the fluorescence readout curves  $\int V_{\text{fl,off}}(t) - V_{\text{fl,on}}(t) dt$  in units that leave unclear the fractional change in fluorescence corresponding to the spin population transferred by the MW control pulse. The contrast can be reported in absolute units as the peak fractional

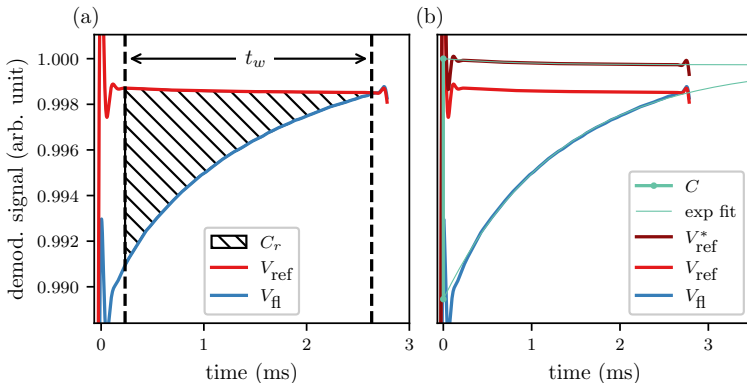


FIG. 1: Illustration of measurement protocol using  $\sim 10000$  readout sequences averaged after demodulation. We measure  $C_r$  as shown in (a) by summing over  $V_{\text{ref}} - V_{\text{fl}}$  within the window  $t_w$ . The calibration procedure for converting  $C_r$  to  $C$  is shown in (b). Exponential fits of  $V_{\text{ref}}$  and  $V_{\text{fl}}$  are used first to define  $V_{\text{ref}}^* = lV_{\text{ref}}$  with  $l$  such that  $V_{\text{ref}}^*$  and  $V_{\text{fl}}$  converge as  $t \rightarrow \infty$ . The fits are then used to evaluate  $C$ , the fractional difference at  $t = 0$ .

difference between the fluorescence curves  $C_{\text{abs}} \equiv \max_t \left( \frac{V_{\text{fl,off}}(t) - V_{\text{fl,on}}(t)}{V_{\text{fl,off}}(t)} \right)$ . We converted  $C_r$  into a quantity comparable to  $C_{\text{abs}}$  by a calibration procedure shown in Fig. 1 and justify this in the following steps.

Starting in the simpler case where  $t_l$  is long enough to completely reinitialize the ensemble, we take  $V_{\text{ref}}(t) = V_{\text{fl,off}}(t)$ . This is justified because the ensemble spin population is already at equilibrium at the start of the ideal  $V_{\text{fl,off}}(t = 0)$  and remains so throughout the readout, so the fluorescence measured in  $V_{\text{fl,off}}(t)$  is linear with the small fluctuations in pump power throughout the pulse duration:  $V_{\text{ref}}(t) = kV_{\text{fl,off}}(t)$ . If the pump pulse is sufficiently long, the ensemble is reinitialized into the equilibrium spin state population (see Wolf et al. 2015, citation in main text) by the time  $t = t_l$  when the reference scaling is defined:  $V_{\text{fl,off}}(t_l) = V_{\text{ref}}(t_l) \Rightarrow k = 1$ . For complete reinitialization of the ensemble as shown in Fig. 2, we can therefore use  $\frac{V_{\text{ref}}(0) - V_{\text{fl}}(0)}{V_{\text{ref}}(0)} = C_{\text{abs}}$ .

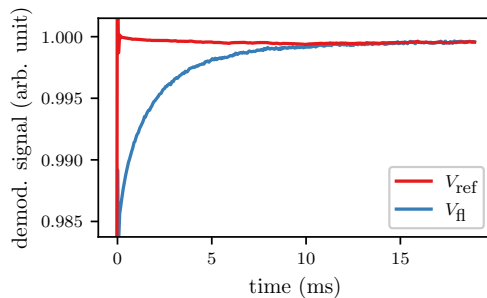


FIG. 2: Example measurement of reference and fluorescence readout with complete reinitialization of the ensemble using a long laser pulse  $t_l = 20$  ms.

With microwave pulses applied, we found our fluorescence signal  $V_{\text{fl}}$  to be dominated by a decay constant of  $\tau_R = 1.4$  ms (see Fig. 1(a)). To fully reinitialize the weakly-pumped peripheral NV centers with slower repolarization rates, a long readout time  $t_l = 20$  ms was necessary. These peripheral NV centers contribute a minority of the fluorescence and contrast, corresponding to a small contribution from the slower exponential decay terms present in  $V_{\text{fl}}$  in Fig. 2. With a large majority of the contrast information obtained in the first 3 ms, we used  $t_l = 3$  ms for a substantial improvement in bandwidth and sensitivity at the expense of a small reduction in contrast. As we argue in the main text and show again in Fig. 4, the peripheral NV centers contribute much less to  $C$  than their minority share

of  $V_{\text{fl}}$  for the short  $t_l = 3$  ms and can therefore be safely neglected. Because we neglect the peripheral NV centers, we consider only those within  $r < 0.5r_0$  to constitute the ensemble we address experimentally.

With the short  $t_l = 3$  ms, the strongly-pumped NV ensemble within  $r < 0.5r_0$  with  $\tau_R \approx 1.4$  ms was nearly but not fully reinitialized. In this case, our argument that  $V_{\text{ref}} = kV_{\text{fl,off}}$  holds, but  $k = 1$  can no longer be justified because the spin population is not at its equilibrium value at  $t = t_l$ . To approximate  $V_{\text{fl,off}}$ , we therefore fit  $V_{\text{fl}}$  and  $V_{\text{ref}}$  to single exponential decays and defined  $V_{\text{ref}}^* = lV_{\text{ref}}$ , with  $l$  such that the long-time limit of the fit of  $V_{\text{ref}}^*$  is equal to the long-time limit of the fit of  $V_{\text{fl}}$  as shown by the green traces in Fig. 1(b). With the reference value of  $V_{\text{ref}}^*$  set to the equilibrium value that  $V_{\text{fl}}$  decays towards, we have  $lk \approx 1 \Rightarrow V_{\text{ref}}^* \approx V_{\text{fl,off}}$  for the addressed ensemble. We defined the contrast  $C$  presented for all contrast data in this work as the peak fractional difference between the exponential fits of  $V_{\text{ref}}^*$  and  $V_{\text{fl}}$

$$C \equiv \frac{V_{\text{ref}}^*(t=0) - V_{\text{fl}}(t=0)}{V_{\text{ref}}^*(t=0)}.$$

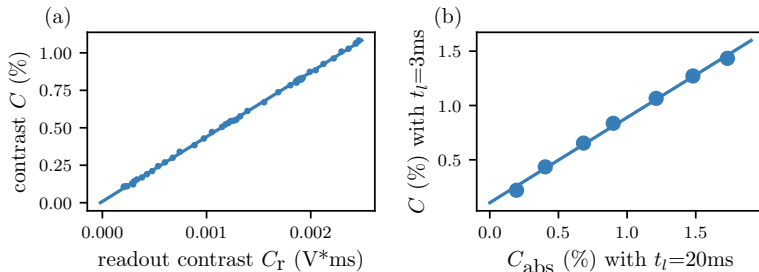


FIG. 3: (a) Calibration of scaling from  $C_r$  to  $C$ . The slope of this fit was used to scale all  $C_r$  measurements to the presented  $C$  values. (b) Demonstration of the linear relationship between the contrast  $C$  we present in all ODMR spectra measurements (using  $t_l = 3$  ms) and the absolute contrast  $C_{\text{abs}}$  obtained with a fully reinitialized ensemble ( $t_l = 20$  ms).

We measured  $C_r$  and extracted  $C$  across a broad range of experimental contrasts achieved by applying flat microwave pulses of varying power and length. All  $C$  values stated throughout this work are measurements of  $C_r$  scaled by the slope of the calibration fit in Fig. 3(a).

Finally, in Fig. 3(b), we compare the contrast  $C$  for  $t_l = 3$  ms with the absolute contrast  $C_{\text{abs}}$  obtained by using  $t_l = 20$  ms pulses sufficient to fully reinitialize the ensemble. We

find that our method results in a small, linear decrease of the measured contrast due to the loss of contrast from the beam periphery, making  $C$  a reliable comparative estimate of the absolute total ODMR contrast  $C_{\text{abs}}$ .

## B. Modelling of Readout Dynamics

Our model follows from these physically reasonable assumptions:

1. That there is a constant, fixed NV density spread throughout the diamond.
2. That our pump beam has a Gaussian lineshape and that it remains so during passage through the diamond.
3. That we can therefore model our incident beam intensity  $I(r)$  as a Gaussian function, scaled to the input laser power.
4. That we can use the same incident intensity throughout the diamond, by assuming our impurity density is sufficiently low such that absorption will not significantly reduce intensity deeper into the diamond (intensity constant with thickness).
5. Because we are interested in readout properties, coherences in the spin manifold can be ignored. Therefore, the preceding MW pulse can be modelled as a population transfer between the  $m_s=0$  and  $m_s=\pm 1$  states with fidelity  $F$ .
6. That this transfer occurs instantaneously, or on a timescale where the microwave pulse is significantly shorter than the laser readout pulse.
7. That the bias magnetic field is uniform, that the NV detuning varies spatially on a scale larger than the beam width, and that the MW field and therefore  $F$  does not vary significantly throughout the beam profile (it likely varies with the distance from the antenna, which is compatible with the model).

We modelled our ensemble by dividing the area of the pump beam cross section within our diamond into rings of radius  $r$  and width  $dr$ , with  $r=0$  in the center of the pump beam profile. We then considered all NVs within the volume contained in these rings  $N_r$  to experience a laser intensity  $I(r)$  with a Gaussian profile. We simulated the NV dynamics using an 8-level system (main text ref [65]), which contained the populations of the NV<sup>-</sup>  $m_s \in \{0, 1\}$  optical ground ( $N_1$  and  $N_2$ ) and excited ( $N_3$  and  $N_4$ ) states, the singlet shelving states ( $N_5$  and  $N_6$ ), and the NV<sup>0</sup> optical ground ( $N_7$ ) and excited ( $N_8$ ) states. The level model follows the differential equations:

$$\begin{aligned}
\frac{dN_1}{dt} &= -(W_g + W_{MW})N_1 + W_{MW}N_2 + k_{31}N_3 + k_{61}N_6 + W_rN_8/2 \\
\frac{dN_2}{dt} &= W_{MW}N_1 - (W_g + W_{MW})N_2 + k_{42}N_4 + k_{62}N_6 + W_rN_8/2 \\
\frac{dN_3}{dt} &= W_gN_1 - (k_{31} + k_{35} + W_i)N_3 \\
\frac{dN_4}{dt} &= W_gN_2 - (k_{42} + k_{45} + W_i)N_4 \\
\frac{dN_5}{dt} &= k_{35}N_3 + k_{45}N_4 - k_{56}N_5 \\
\frac{dN_6}{dt} &= k_{56}N_5 - (k_{61} + k_{62})N_6 \\
\frac{dN_7}{dt} &= W_iN_3 + W_iN_4 - W_{g0}N_7 + k_{87}N_8 \\
\frac{dN_8}{dt} &= W_{g0}N_7 - (k_{87} + W_r)N_8,
\end{aligned}$$

where  $k_{ij}$  are the decay rates given in the cited works. The green pump intensity  $I_g$  and the cross-sections  $\sigma_j$  determine the rates  $W_j = \sigma_j I_g \lambda_g / (hc)$  for the considered processes:  $W_g$  green excitation of the  $NV^-$ ,  $W_{g0}$  green excitation in the neutral charge state,  $W_i$  deionization to the  $NV^0$  state, and  $W_r$  reionization to the  $NV^-$  state. To simulate the reinitialization dynamics of the ensemble, we first allowed the system to evolve under constant pump illumination  $I(r)$  until population equilibrium was reached, starting from the arbitrary initial condition of  $P(N_1) = 1$  which did not affect the steady state. Then, relaxation was allowed to occur ( $N_3 \rightarrow N_1$ ,  $N_4 \rightarrow N_2$ ,  $N_5 \rightarrow N_6$ ,  $\frac{k_{61}}{k_{61}+k_{62}}N_6 \rightarrow N_1$ ,  $\frac{k_{62}}{k_{61}+k_{62}}N_6 \rightarrow N_2$ ,  $N_8 \rightarrow N_7$ ). To implement a microwave pulse of fidelity  $F$ , we instantaneously transferred NV spins between states  $N_1$  and  $N_2$ , with the output after the pulse  $N'_2 = FN_1 + (1-F)N_2$ ,  $N'_1 = FN_2 + (1-F)N_1$ . We then continued to calculate the time evolution with the applied pump laser intensity, up to a specified laser pulse length  $t_l$ .

Here, we supplement the results of the simulation presented in the main text with two findings. First, we consider how the ensemble behaves with realistic fidelity  $F < 1$ , since we concluded from the main text Fig. 9(a) that the hysteresis of the beam periphery was sufficiently small to be negligible in our measurements in the  $F = 1$  case. In Fig. 4, we compare the sequence behavior with ideal and sub-ideal fidelity. We find that for  $F < 1$ , the NV centers in the beam periphery reach their steady-state pulse response earlier. The decay

of the deviation from the steady-state response is hastened by the loss of information with each imperfect  $\pi$ -pulse, which means the results presented in the main text are a worst-case scenario for the hysteresis.

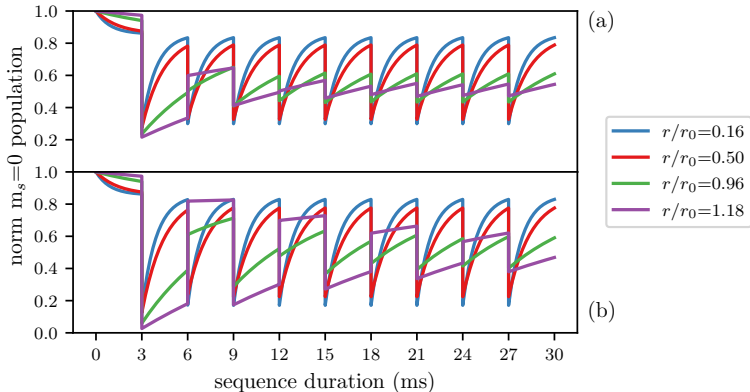


FIG. 4: Simulated time evolution showing the change in hysteresis effects with fidelity  $F = 0.8$  (a) and  $F = 1$  (b). Ten  $t_l = 3$  ms laser pulses separated by relaxation and microwave pulses of the respective fidelity are simulated.

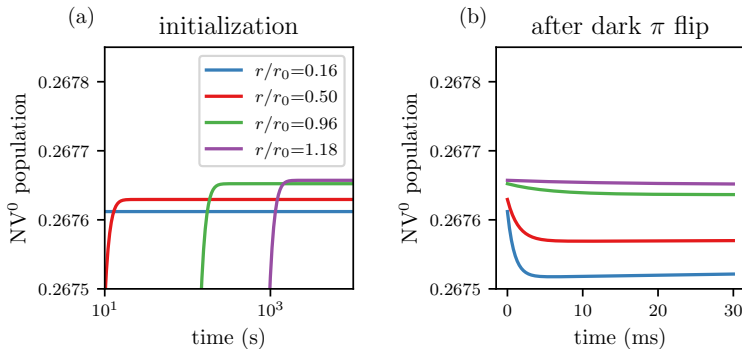


FIG. 5: Simulated charge state dynamics in intensity regime of our measurements, using the same color-matched  $r/r_0$  values as in the main text. In (a), the charge state is initialized, and in (b), it is observed after relaxation and an electron spin flip, demonstrating that charge state dynamics are negligible.

The last consideration explored with our model was whether the NV charge state could contribute to hysteresis effects. We performed two simulations and show their result in Fig. 5. First the  $NV^0$  state population was tracked during evolution from the  $N_1$  state towards equilibrium. Then relaxation and a  $F = 1$   $\pi$ -pulse was applied to represent the largest possible change typical during the dark time in our measurements. From here, the  $NV^0$  population was tracked under constant illumination. We found that the equilibrium  $NV^0$  population was nearly independent of the intensity within the beam profile, and that the deviations after changes in the spin state were only of the order 0.01% in amplitude. We also note that the long timescales necessary to reach charge equilibrium under low intensity are not predictive of slow effects in our measurements, because once the charge equilibrium is reached, it remains near  $P(NV^0) \approx 0.2676$  under all dynamics considered.

### C. NV ensemble characterization

We report the measured decay times of our NV ensemble to be  $T_1 = 7.1$  ms,  $T_2 = 7.0$   $\mu$ s, and  $T_2^* = 0.44$   $\mu$ s, from measurements shown in Fig. 6 and 7. The relationship between MW power and the ensemble-averaged Rabi frequencies we obtain is shown in Fig. 8.

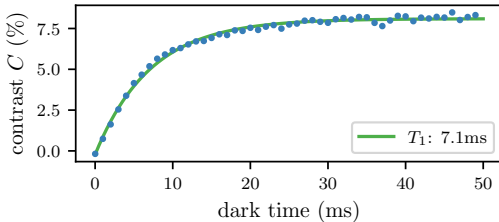


FIG. 6:  $T_1$  decay rate measurement. Instead of the MW pulse in the readout sequence (main text Fig. 5(b)), the laser was left off for a time represented by the x-axis in (b).

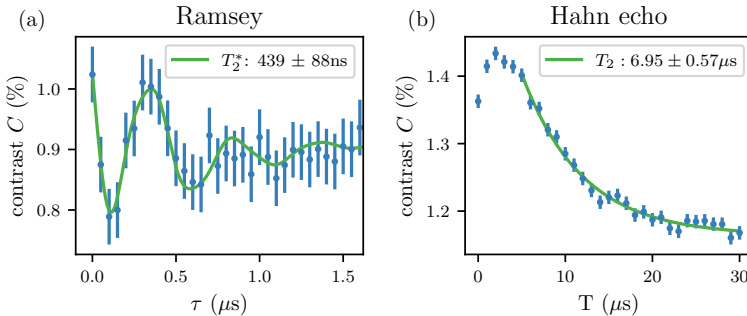


FIG. 7: Ramsey and Hahn echo measurements to retrieve the coherence times of  $T_2^* = 0.44$   $\mu$ s and  $T_2 = 7.0$   $\mu$ s. The Ramsey measurement (a) was fit to  $e^{-\tau/T_2^*} [\cos(2\pi f_1\tau + \phi_1) + \cos(2\pi f_2\tau + \phi_2) + \cos(2\pi f_3\tau + \phi_3)] + \text{DC}$  to account for the possible contribution of the three hyperfine resonances. The Hahn echo measurement (b) was fit to a single exponential decay. We note that the increase in contrast for  $T < 5$   $\mu$ s in (b) is typical of echo measurements we perform and exclude this region from the fit.

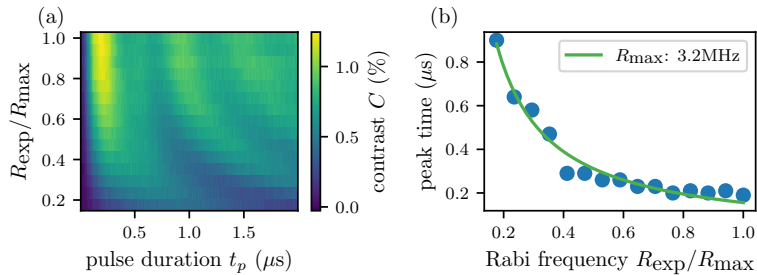


FIG. 8: (a) Rabi oscillation measurements from which we determine the scaling between the set power and ensemble average Rabi frequency. (b) Fit of the time to the initial peaks  $T_p$  for each  $R_{\text{exp}}$  in (a), used to estimate the scaling from the set MW power  $P_{\text{MW}}$  to  $R_{\text{exp}}$ ,

$$\text{where } R_{\text{exp}} = R_{\text{max}} \sqrt{P_{\text{MW}}/P_{\text{MWmax}}}, \text{ and } T_p = 1/2R_{\text{exp}}.$$

## D. ODMR measurement details

In the main text, the best-performing 3fd pulse is presented for each MW power setting (in terms of the Rabi frequency  $\Omega$ ). The full exploration of the measured parameter space is shown here in Fig. 9. For each 3fd pulse attempted, a 2 MHz section of the ODMR spectrum was measured, with an example shown in Fig. 10, where the error in the slope fit was propagated from the error statistics we measured for repeated acquisitions. 2 MHz is sufficient because the hyperfine resonances (separated by 2.16 MHz) are resolved, and the region of greatest slope is the  $< 1$  MHz range between the center resonance peak and the adjacent dip. We fit this data to a double-Lorentzian (ignoring the low-frequency hyperfine resonance peak outside of the measured spectral range)

$$C = \frac{a}{1 + \left(\frac{f-f_0}{\gamma/2}\right)^2} + \frac{b}{1 + \left(\frac{f-f_0-2.16\text{MHz}}{\gamma/2}\right)^2} + \text{DC}$$

and present the absolute maximum of the slope of the fit function  $C' = \frac{dC}{df}$ . The error propagation is performed by numerically calculating the Jacobian relative to the fit parameters  $\mathbf{J}(C') = \left[\frac{\partial C'}{\partial f_0}, \frac{\partial C'}{\partial \gamma}, \frac{\partial C'}{\partial a}, \frac{\partial C'}{\partial b}, \frac{\partial C'}{\partial \text{DC}}\right]$  at the frequency of the greatest slope, and multiplying by the fit parameter covariance matrix  $\Sigma_{\mathbf{C}}$ , yielding

$$\sigma = \mathbf{J}\Sigma_{\mathbf{C}}\mathbf{J}^T.$$

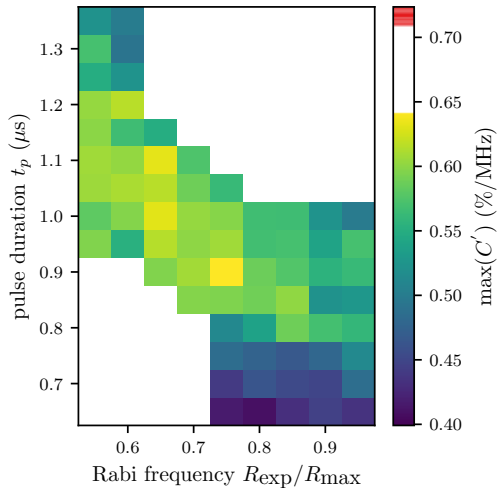


FIG. 9: Maximum ODMR slope of 3fd pulses across duration and power parameter space, determined by fitting the ODMR spectrum as described in Fig. 10. The 3fd sensitivity data shown in the main text are the most sensitive points for each column ( $\Omega$ ) shown here. The colorbar shows the mean value and  $\pm 1\sigma$  shaded of the best optimal control pulse sensitivity for comparison.

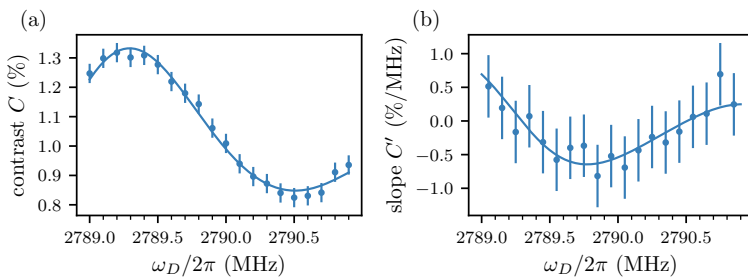


FIG. 10: Measurement and fits for the best 3fd flat pulse. The error bars on the ODMR data are the standard error of the mean for the number of acquisitions we average. The slope data are simply the discrete differential of the ODMR data with propagated error bars and are not used in fitting.

## Including the hyperfine transitions for $^{15}\text{N}$

The derivation of the Fourier components of the Hamiltonian for the two hyperfine levels of  $^{15}\text{N}$  is similar to the one for the three hyperfine levels of  $^{14}\text{N}$ . We assume that the  $m_s = \pm 1$  states are clearly split by a static magnetic bias field and no interaction between NV spins. A single set of two NV centers that each correspond to one of the hyperfine transitions can then be reasonably approximated as two independent two-level systems. The drift Hamiltonian thus has the form

$$\hat{\mathcal{H}}_0 = \sum_u \frac{\omega_{0,u}}{2} \sigma_{z,u}, \quad (1)$$

where  $\omega_{0,u}$  is the transition frequency of hyperfine transition  $u$ , and  $\sigma_{z,u}$  is a Pauli spin- $z$  matrix that is specific to transition  $u$ . We choose to denote the transitions  $l$  and  $r$  to avoid confusion with the terms used for the  $^{14}\text{N}$  hyperfine splitting. The states of the two two-level systems can be completely described by a single vector of length 4, and the  $\sigma_{z,k}$ -matrices can be represented by the following 4-by-4 matrices.

$$\sigma_{z,l} = \begin{pmatrix} 1 & 0 & 0 & 0 \\ 0 & -1 & 0 & 0 \\ 0 & 0 & 0 & 0 \\ 0 & 0 & 0 & 0 \end{pmatrix}, \quad \sigma_{z,r} = \begin{pmatrix} 0 & 0 & 0 & 0 \\ 0 & 0 & 0 & 0 \\ 0 & 0 & 1 & 0 \\ 0 & 0 & 0 & -1 \end{pmatrix} \quad (2)$$

We again assume a single-frequency control field that is linearly polarized in the  $x$ -direction, which is perpendicular to the NV axis, allowing the control Hamiltonian to be written in the form

$$\hat{\mathcal{H}}_c = \sum_j \sigma_{x,u} [I(t) \cos(\omega_D t) + Q(t) \sin(\omega_D t)], \quad (3)$$

where  $\sigma_{x,u}$  is a Pauli spin- $x$  matrix that is specific to transition  $u$ . Similarly to the  $\sigma_{z,u}$ -matrices, the  $\sigma_{x,u}$ -matrices can be represented by 4-by-4 matrices.

$$\sigma_{x,l} = \begin{pmatrix} 0 & 1 & 0 & 0 \\ 1 & 0 & 0 & 0 \\ 0 & 0 & 0 & 0 \\ 0 & 0 & 0 & 0 \end{pmatrix}, \quad \sigma_{x,r} = \begin{pmatrix} 0 & 0 & 0 & 0 \\ 0 & 0 & 0 & 0 \\ 0 & 0 & 0 & 1 \\ 0 & 0 & 1 & 0 \end{pmatrix} \quad (4)$$

The  $\sigma_{y,u}$  matrices, which are Pauli spin- $y$  matrices that are specific to transition  $j$  and will be used later, can also be represented by 4-by-4 matrices.

$$\sigma_{y,l} = \begin{pmatrix} 0 & -i & 0 & 0 \\ i & 0 & 0 & 0 \\ 0 & 0 & 0 & 0 \\ 0 & 0 & 0 & 0 \end{pmatrix}, \quad \sigma_{y,r} = \begin{pmatrix} 0 & 0 & 0 & 0 \\ 0 & 0 & 0 & 0 \\ 0 & 0 & 0 & -i \\ 0 & 0 & i & 0 \end{pmatrix} \quad (5)$$

The total Hamiltonian thus has the form

$$\hat{\mathcal{H}}(t) = \sum_u \left( \frac{\omega_{0,u}}{2} \sigma_{z,u} + \sigma_{x,u} [I(t) \cos(\omega_D t) + Q(t) \sin(\omega_D t)] \right). \quad (6)$$

We can simplify the rest of the calculations by working in a rotating frame at  $\omega_D$ . This is done via the unitary rotation operator

$$\hat{R} = \exp\left(\sum_u i\omega_D t \sigma_{z,u}/2\right) \quad (7)$$

and in this frame, the Schrödinger equation can be rewritten as  $i\frac{d}{dt}|\psi'\rangle = \hat{\mathcal{H}}'|\psi'\rangle$  with  $|\psi'\rangle = \hat{R}|\psi\rangle$  and the Hamiltonian

$$\hat{\mathcal{H}}' = \hat{R}\hat{\mathcal{H}}\hat{R}^\dagger + i\frac{\partial\hat{R}}{\partial t}\hat{R}^\dagger, i\frac{\partial\hat{R}}{\partial t}\hat{R}^\dagger = -\frac{\omega_D}{2}\sum_j \sigma_{z,j}. \quad (8)$$

The drift Hamiltonian is time-independent and the  $\sigma_{z,u}$  matrices all commute with each other, resulting in

$$\hat{R}\hat{\mathcal{H}}\hat{R}^\dagger = \hat{\mathcal{H}}_0 + \hat{R}\hat{\mathcal{H}}_c\hat{R}^\dagger. \quad (9)$$

The unitary rotation operator will also commute with every term in  $\hat{\mathcal{H}}_c$  except for  $\sigma_{x,u}$ . More precisely,  $[\sigma_{z,u}, \sigma_{x,u'}] = 2i\sigma_{y,u}\delta_{u,u'}$  and  $[\sigma_{z,u}, \sigma_{y,u'}] = -2i\sigma_{x,u}\delta_{u,u'}$ . The Baker-Campbell-Hausdorff lemma then allows us to write

$$\hat{R}\hat{\mathcal{H}}_c\hat{R}^\dagger = \sum_u (\sigma_{x,u} \cos(\omega_D t) + \sigma_{y,u} \sin(\omega_D t)) \cdot [I(t) \cos(\omega_D t) + Q(t) \sin(\omega_D t)]. \quad (10)$$

If we insert the above expression in Eq. (8) and furthermore define the detuning,  $\Delta = (\omega_{0,l} + \omega_{0,r})/2 - \omega_D$ , as the difference between the average of the two hyperfine transition frequencies and the central driving frequency,  $\omega_D$ , we obtain the expression

$$\hat{\mathcal{H}}' = \sum_u \left( \frac{\Delta + m_u \delta_I/2}{2} \sigma_{z,u} + (\sigma_{x,u} \cos(\omega_D t) + \sigma_{y,u} \sin(\omega_D t)) \right) \times [I(t) \cos(\omega_D t) + Q(t) \sin(\omega_D t)], \quad (11)$$

where  $\delta_I = 3.03$  MHz is the splitting between the hyperfine transitions,  $m_l = -1$  and  $m_r = 1$ . Expanding by using the trigonometric relations

$$\cos(\omega_D t)^2 = \frac{1}{2} [1 + \cos(2\omega_D t)], \quad (12)$$

$$\sin(\omega_D t)^2 = \frac{1}{2} [1 - \cos(2\omega_D t)] \quad (13)$$

and

$$\cos(\omega_D t) \sin(\omega_D t) = \frac{1}{2} \sin(2\omega_D t), \quad (14)$$

one finds

$$\hat{\mathcal{H}}' = \sum_u \left( \frac{\Delta + m_u \delta_I / 2}{2} \sigma_{z,u} + I(t) \left[ \sigma_{x,u} \frac{1}{2} [1 + \cos(2\omega_D t)] + \sigma_{y,u} \frac{1}{2} \sin(2\omega_D t) \right] + Q(t) \left[ \sigma_{x,u} \frac{1}{2} \sin(2\omega_D t) + \sigma_{y,u} \frac{1}{2} [1 - \cos(2\omega_D t)] \right] \right), \quad (15)$$

which can be simplified by using the rotating wave approximation to eliminate the fast oscillating terms  $\cos(2\omega_D t)$  and  $\sin(2\omega_D t)$ .

$$\hat{\mathcal{H}}' = \sum_u \left( \frac{\Delta + m_u \delta_I / 2}{2} \sigma_{z,u} + \frac{I(t)}{2} \sigma_{x,u} + \frac{Q(t)}{2} \sigma_{y,u} \right) \quad (16)$$

Combining these equations with those in the main text yields:

$$\hat{\mathcal{H}}_n = \sum_u \frac{1}{T} \int_0^T \exp(in\Omega t) \left( \frac{\Delta + m_u \delta_I / 2}{2} \sigma_{z,u} + \sum_{j=1}^{N_f} [a_{jx} \sigma_{x,u} + a_{jy} \sigma_{y,u}] \sin(j\Omega t) \right). \quad (17)$$

The above expression can be further simplified by using the exponential form of a sine and the integral form of a Kronecker delta. Doing so yields the final expression for the Fourier components of the Hamiltonian when both of the  $^{15}\text{N}$  hyperfine transitions are taken into account,

$$\hat{\mathcal{H}}_n = \sum_u \left( \frac{\Delta + m_u \delta_I / 2}{2} \sigma_{z,u} \delta_{n,0} + \sum_{j=1}^{N_f} \frac{1}{2i} [a_{jx} \sigma_{x,u} + a_{jy} \sigma_{y,u}] \cdot [\delta_{n,j} - \delta_{-n,j}] \right). \quad (18)$$

## E. Best Optimal Pulse Control Parameters

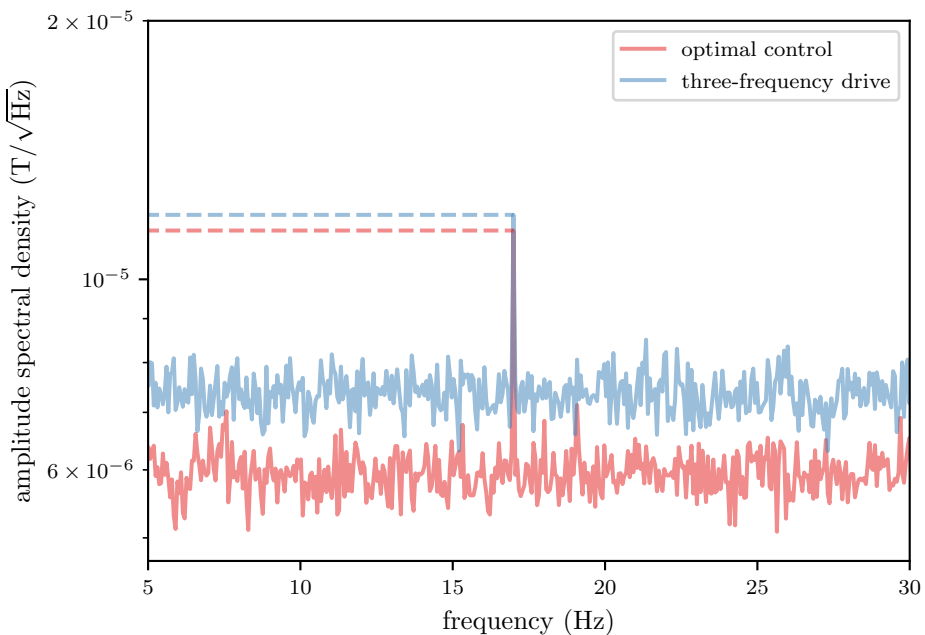
The control amplitudes,  $a_{jk}$ , that define our best optimal pulse are given (in MHz) in Table I. This pulse has a duration of 1.85  $\mu\text{s}$ .

TABLE I: The  $a_{jk}$ -values of our best optimal pulse in MHz.

$a_{1x}$	$a_{2x}$	$a_{3x}$	$a_{4x}$	$a_{5x}$
0.11388948	0.09884733	-0.00809110	-0.00177604	0.00918642
$a_{6x}$	$a_{7x}$	$a_{8x}$	$a_{9x}$	$a_{10x}$
-0.088628	-0.11101755	0.00940646	0.11946038	0.11709449
$a_{1y}$	$a_{2y}$	$a_{3y}$	$a_{4y}$	$a_{5y}$
0.09465327	0.08214617	-0.00670811	-0.00148568	0.00772306
$a_{6y}$	$a_{7y}$	$a_{8y}$	$a_{9y}$	$a_{10y}$
-0.07368535	-0.09219246	0.00782588	0.09930594	0.09733759

## 5.4 Revision

The only major issue raised by a reviewer was the lack of a field measurement to back up our claim to improved magnetic sensitivity. We have remedied this by rebuilding the setup and taking magnetic field measurements while applying a transient magnetic field via wire coils placed on either side of the diamond sensor along the axis of the bias magnetic field. A 17 Hz current was applied to the coils which produced a field with  $\sim 10 \mu\text{T}$  peak to peak amplitude. The MW drive frequency was set to the value corresponding to the greatest slope in the ODMR spectrum, and time series of the ODMR contrast were measured using both the optimal control pulse and the three frequency drive pulse. The amplitude spectral density is shown in Fig. 5.1, where the SNR is  $\sim 19\%$  greater with the optimal control pulse.



**Figure 5.1.** Amplitude spectral density for magnetic sensing with optimal control and three frequency drive MW pulses with 17 Hz test field applied.

# CHAPTER 6

# Beam shaping

---

## 6.1 Background

While investigating the use of optimal control methods for large ensembles, we collected light from the periphery of the ensemble illuminated by the weak tails of the laser beam's intensity distribution. We noticed that this distorted the shape of the fluorescence curve, which for a single NV center driven by low optical excitation intensity would be a single exponential decay [70]. The weakly excited NV centers in the beam periphery repolarized slowly enough that the time necessary to repolarize them fully was nearly an order of magnitude longer than the optimal laser pulse time for measuring the ODMR contrast [42]. Because they were polarized so little, those peripheral NV centers did not contribute to the signal to noise ratio of the ODMR measurement.

This led us to study how the intensity distribution of the laser beam could be shaped to repolarize the NV ensemble at a more homogeneous rate. We found both through measurements and through simulation that the SNR of the ensemble ODMR contrast measurement could be improved with simple beam shaping techniques. We used a different diamond for this work than for the previous two articles, which had NV centers distributed throughout the diamond volume, because the beam shaping optics we used only create a homogeneous intensity profile in an imaging plane. The diamond used for this work has a 25  $\mu\text{m}$  layer of NV centers with a higher but similar regime of NV density  $\sim 15$  ppb.

## 6.2 Article

This study resulted in the following article, which we will soon submit roughly as presented here and with the following Supplementary Information.

# Beam shaping for homogeneous ODMR contrast readout in large-ensemble nitrogen-vacancy sensing

Joshua D. Clement,<sup>1</sup> James L. Webb,<sup>1,\*</sup> Kirstine Berg-Sørensen,<sup>2</sup> Alexander Huck,<sup>1,†</sup> and Ulrik Lund Andersen<sup>1,‡</sup>

<sup>1</sup>*Center for Macroscopic Quantum States (bigQ), Department of Physics, Technical University of Denmark, Kgs. Lyngby, Denmark*

<sup>2</sup>*Department of Health Technology, Technical University of Denmark, Kgs. Lyngby, Denmark*

Quantum sensing with ensembles of solid-state defect centers such as Nitrogen-Vacancy (NV) centers in diamond relies on optical excitation to readout and to repolarize the ensemble spin. Due to ease of implementation, TEM<sub>00</sub> beams with a gaussian-distributed intensity profile are often used for optical excitation. We show in this work that the optical spin state readout of an NV center ensemble addressed by a conventional TEM<sub>00</sub> beam suffers from the inhomogeneity of beam intensity distribution. We find through simulation that in the ideal case, a 26% improvement in shot noise-limited readout of the ODMR contrast can be obtained with a homogeneous beam intensity distribution. We use a flat beam shaper to transform the TEM<sub>00</sub> mode into a beam with a more homogeneous intensity distribution in the NV ensemble and measure a 13% improvement in the shot noise-limited ODMR contrast SNR.

## I. INTRODUCTION

Nitrogen-vacancy (NV) centers in diamond are a promising and versatile platform for solid state quantum sensing at room temperature[1, 2]. They are sensitive to temperature[3–5], pressure[6], and electric[7] and magnetic[8–10] fields. Diamond is biocompatible, which makes NV sensing particularly interesting for biophysical measurements[11] such as magnetoneurography[12], biomagnetic imaging[13], and detection of metalloproteins[14].

Sensing with negatively charged NV centers can be performed via optically detected magnetic resonance (ODMR)[15]. After optical excitation, an NV center probabilistically fluoresces with a spin-dependent probability[16]. The nonradiative decay path is not spin-conserving, and this results in an equilibrium  $\sim 80\%$  spin polarization under continuous illumination by green light at moderate intensity[17]. An electron paramagnetic resonance can be driven by resonant microwave (MW) fields, transferring spin population from the bright spin state to the dark spin state, creating a contrast in the subsequent fluorescence in proportion with the population transfer[18].

For applications that can sacrifice spatial resolution, sensing can be performed with an ensemble of NV centers, to improve the shot noise-limited signal to noise ratio (SNR) of the combined fluorescence by scaling with  $\sqrt{N}$  for  $N$  the number of addressed NV centers[19, 20]. Laser beams with a dominant TEM<sub>00</sub> mode, which have a gaussian distribution of intensity in the beam's transverse plane, are commonly used to optically excite NV center ensembles, even in record-setting ensemble sensing experiments[12]. The inhomogeneity of the beam in-

tensity results in differences throughout the ensemble in the NV electron state dynamics during optical excitation, which impairs the SNR of the ensemble ODMR contrast readout by increasing measurement overhead[21].

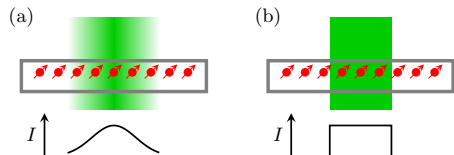


FIG. 1. Color online. Example ensembles of NV centers optically excited by (a) a laser beam with a gaussian intensity profile and (b) by a beam with a homogeneous intensity profile.

We simulated the readout and repolarization dynamics for a pulsed ODMR contrast measurement over a range of pulse duration and optical excitation intensity for both an ensemble optically driven by a beam with a homogeneous intensity distribution and one driven by a conventional TEM<sub>00</sub> beam with a gaussian intensity distribution. The result predicts a 26% improvement in ODMR contrast SNR with the homogeneous intensity distribution. We measured the ensemble ODMR contrast over a similar parameter range with both a conventional TEM<sub>00</sub> beam and with a shaped beam with relatively more homogeneous intensity as depicted in Fig. 1. There was a qualitative match to the simulated results and a 13% improvement with the more homogeneous beam shape.

## II. METHODS

### A. Setup

Our setup shown in Fig. 2 used a 532 nm 1.5 W laser to optically excite the NV center ensemble, both to readout

\* jaluwe@fysik.dtu.dk

† alexander.huck@fysik.dtu.dk

‡ ulrik.andersen@fysik.dtu.dk

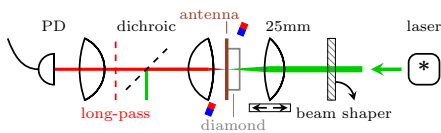


FIG. 2. Experimental setup for beam shaping and fluorescence collection in the measurement of ODMR contrast.

and to polarize the NV center spins. The laser beam was switched by an acousto-optic modulator (AOM) with the first order AOM mode selected by a pinhole. The pinhole also spatially filtered the transverse profile, leaving a beam dominated by the  $\text{TEM}_{00}$  spatial mode with a gaussian intensity profile in the far field transverse plane, throughout this work referred to as a gaussian beam.

After the pinhole, the beam was expanded and collimated with a 4 mm diameter. An Eksma Optics GTH-4-2.2FA flat-top beam shaper transformed the 4 mm  $\text{TEM}_{00}$  beam into one which created a more homogeneous intensity distribution in the image plane of a subsequent lens. The beam shaper was mounted in the beam path on a flip mount, allowing either the original gaussian beam or the flat shaped beam to be used. The beam was finally focused onto the diamond using a lens with a focal length of 25 mm, which was mounted on a translation stage to allow for adjustment of the gaussian profile spot size in the plane of the NV center layer in the diamond.

$\pi$  rotations of the NV center electron spins from the bright state to the dark state were induced by MW pulses delivered by a square split-ring resonator[22] designed to ensure uniformity of MW field intensity throughout the ensemble. Fluorescence was collected from the back of the diamond, separated from the laser beam by both a dichroic mirror and a long-pass filter. For ODMR contrast measurement, a photodiode (PD) was placed in the image plane of the focused fluorescence as depicted in Fig. 2. For spatially imaging the beam profile, a charge-coupled device camera (not shown) was used in place of the PD to image the NV center ensemble's fluorescence.

The diamond used in our setup has a 25  $\mu\text{m}$  layer with a  $\sim 15$  ppb density of NV centers. The diamond was grown by CVD and isotopically purified with  $^{12}\text{C}$ .

## B. Readout

The experimental goal of this study was to characterize the consequence that the optical excitation beam intensity distribution has on the readout of ODMR contrast in a finite measurement time. It was necessary to measure over a range of pulse duration  $t_l$  and intensity  $I$  regimes to ensure that the optimal parameters were used for each optical excitation beam shape and to validate that our simulation results describe the setup behavior across the parameter space.

We defined the measured ODMR fluorescence contrast

$C_{m,f}(t)$  in terms of the measured fluorescence signals  $V_b(t)$  and  $V_d(t)$  of the NV center ensemble prepared in the bright and dark spin state respectively. We used the protocol shown in Fig. 3(a) to measure  $V_b(t)$  and  $V_d(t)$  across regimes of  $t_l$  from much shorter to much longer than the repolarization time. We continuously applied readout cycles consisting of a (MW control pulse / equivalent delay) followed by a laser pulse of duration  $t_l$ , which produced the fluorescence measured in the signal ( $V_d / V_b$ ). For long  $t_l$ , the spin state can be considered well-initialized at the end of every laser pulse, having reached the equilibrium spin polarization into the bright state, which was then either rotated into the dark state by the MW control pulse or preserved during the equivalent delay. For short  $t_l$ , the ensemble-averaged spin polarization did not reach its equilibrium by the end of each laser pulse, leaving a partial memory of the previous spin state preparation. Therefore the spin initialization differed between  $V_b$  and  $V_d$  for short  $t_l$ . We included a renormalization in the definition of  $V_b$  such that  $V_b(t_l) = V_d(t_l)$  and waited for a sufficient number of readout cycles to reach the steady-state response (i.e. the fluorescence of the  $i^{\text{th}}$  readout differs from the  $(i-1)^{\text{th}}$  only by noise) before recording. The fluorescence contrast  $C_{m,f}(t) \equiv V_b(t) - V_d(t)$  therefore captured the difference in the fluorescence readout that followed from how much the ensemble-averaged spin state was changed by the MW control pulse immediately preceding the readout, which was diminished by the incomplete repolarization in the regime of short  $t_l$ .

## C. Ensemble repolarization model

We simulated NV center repolarization dynamics using an 8-level rate equation model adapted from [17, 23] with rates extracted from[24–27]. The model includes the  $^3\text{A}_2$  and  $^3\text{E}$  states for  $m_s=0$  and  $m_s=-1$ , the shelving states of the nonradiative decay path, and the  $\text{NV}^0$  ground and excited states. A level diagram depicting the model and technical details of the implementation are presented in the Supplementary Information. We used an ordinary differential equation (ODE) solver to solve the evolution of the level populations during optical excitation, and the resulting fluorescence was calculated from the populations of the fluorescing states. To simplify the simulations of readout and repolarization without loss of generality, the relaxation and the optional MW control pulse between laser pulses were implemented as single-step linear operations on the system level population vector  $\mathcal{N}$ . The relaxation operation transferred all population from the excited states to ground states in proportion with the relative decay rates of the available decay paths. The MW control pulse operation transferred population between the bright and dark spin states with a linear control pulse fidelity parameter  $F$ , where  $F = 1$  resulted in mirrored populations compared to the input, and  $F = 0$  resulted in unchanged populations.

We used the simulation protocol shown in Fig. 3(b) to

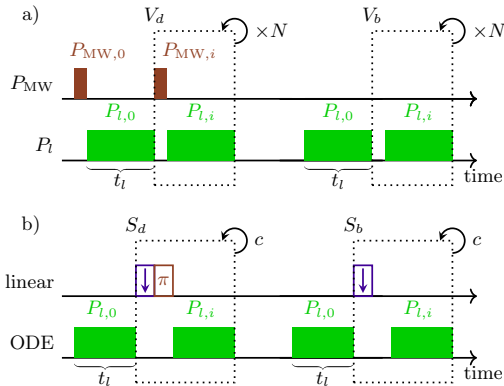


FIG. 3. (a) Measurement protocol for  $V_d$  and  $V_b$ . The time-resolved fluorescence output  $V_i(t)$  from laser pulses  $P_{l,i}$  were recorded and averaged, i.e.  $V_{(d,b)}(t) \equiv \sum_{i=1}^n V_i(t)/n$ . (b) Simulation protocol for  $S_d$  and  $S_b$ . The system level population vector  $\mathcal{N}(t)$  was evolved from arbitrary initial conditions by an ODE solver throughout the initial laser pulse  $P_{l,0}$ . Then a linear relax operation was applied, followed by a MW control pulse operation in the case of  $S_d$ . The subsequent evolution under optical excitation was solved, and the procedure was repeated until the condition  $c \equiv (\mathcal{N}_i(t) - \mathcal{N}_{i-1}(t))/\mathcal{N}_i(t) < 1\%$  was met for all  $t$ .  $S_{(d,b)}(t)$  is the simulated fluorescence output  $\mathcal{F}_i(t)$  of the last  $\mathcal{N}_i(t)$  with normalization such that  $S_b(t_i) = S_d(t_i)$ .

produce  $S_d(t)$  and  $S_b(t)$ , the simulated fluorescence signals after dark and bright spin state preparation respectively, analogous to  $V_d(t)$  and  $V_b(t)$ . Each NV center in the simulated ensemble was initialized with the equilibrium  $NV^0$  ground state population with the remainder in the  $NV^{-1} \ ^3A_2 m_s=0$  state[28, 29]. Then the ODE solver was used to evolve its level population vector  $\mathcal{N}$  under optical excitation with intensity  $I$  for a duration  $t_l$ . The relaxation operation (followed by the MW control operation for  $S_d$ ) was applied to the output  $\mathcal{N}$  at the end of the laser pulse. The resulting  $\mathcal{N}$  was taken as the initial condition for the ODE solver in a subsequent laser pulse, and the simulated readout cycle repeated until the steady-state was reached, defined by  $\mathcal{N}$  changing by less than 1% for all time steps. This eliminated dependence on the arbitrary choice of initial state and any potential spin memory due to short  $t_l$ . As with  $V_b$ ,  $S_b$  was defined with a renormalization such that  $S_b(t_i) = S_d(t_i)$  so that the contrast  $C_{s,f}$  would represent the change in fluorescence caused by the last MW control pulse, even for short  $t_l$ . Because the NV centers in our diamond are oriented evenly along the four crystallographic axes and we only apply MW control pulses those aligned along one axis[15], we included a factor of 4 in the definition of the simulated fluorescence contrast:  $C_{s,f}(t) \equiv (S_b(t) - S_d(t))/4$ .

#### D. Contrast figure of merit

We consider a general case where the goal is to maximize the signal to noise ratio (SNR) of a measurement of the ensemble spin state via the ODMR contrast with repeated readout sequences in a given total measurement time. The signal consists of the detected fluorescence  $V(t)$  which must lie between  $V_b(t)$  and  $V_d(t)$  and therefore has a dynamic range equal to  $C_{m,f}(t)$ . When shot noise-limited, the noise term is linear with  $\sqrt{V(t)} \approx \sqrt{V_b(t)}$ [19, 30], leading us to define the shot noise-scaled contrast  $\overline{C_{m,s}^*}(t) \equiv C_{m,f}(t)/\sqrt{V_b(t)}$ .

The SNR of the measurement over the entire pulse duration as a whole is linear with the total area encompassed by the contrast signal divided by the integrated noise. For a cumulative measurement over an integer number  $N$  of readout pulses with total duration  $t_f \approx nt_l$ ,

$$\text{SNR} \propto \frac{\int_0^{t_f} C_{m,f}(t) dt}{\sqrt{\int_0^{t_f} V_b(t) dt}} = \frac{t_f \frac{1}{t_l} \int_0^{t_l} C_{m,f}(t) dt}{\sqrt{t_f V_b(t_l)}} \quad (1)$$

where the measurement overhead for relaxation and application of MW control pulses is ignored. For a given  $t_f$ , the SNR is maximized by maximizing the shot noise-scaled mean contrast

$$\overline{C_{m,s}} \equiv \frac{\overline{C_{m,f}}}{\sqrt{V_b(t_l)}} = \frac{\frac{1}{t_l} \int_0^{t_l} C_{m,f}(t) dt}{\sqrt{V_b(t_l)}} \quad (2)$$

With limited laser power, there is a tradeoff between per-NV contribution to  $\overline{C_{m,s}}$  and the total number of NV centers  $N$  the beam is spread over. In the case of an ideal homogeneous beam profile, where each addressed NV center is optically driven with the same intensity, the shot noise-scaled mean contrast can be expressed in terms of the individual NV fluorescence contrast  $C_{m,f}^*(t)$  and individual NV contribution to fluorescence readout voltage  $V_b^*(t)$

$$\overline{C_{m,s}} = \frac{N \overline{C_{m,f}^*}}{\sqrt{N V_b^*(t_l)}} \quad (3)$$

We consider the approximation that the fluorescence intensity is linear with optical excitation intensity,  $N \approx \alpha/V_b^*(t_l)$ , for an arbitrary factor  $\alpha$  including laser power and various experimental efficiencies. Then we aim to maximize

$$\overline{C_{m,s}} \approx \frac{\overline{C_{m,f}^*} \sqrt{\alpha}}{V_b^*(t_l)} \propto \frac{\overline{C_{m,f}^*}}{V_b^*(t_l)} \quad (4)$$

In short, the best SNR of an ODMR contrast readout with a fixed laser power is achieved by maximizing the fractional (unitless) mean contrast of each NV center  $\overline{C_{m,u}^*} \equiv \overline{C_{m,f}^*}/V_b^*(t_l)$ .

We show in the Supplementary Information that the pulse duration and intensity which maximize  $\overline{C_{m,u}}$  also

maximize  $\overline{C_{m,s}}$  for optical excitation with the gaussian beam. We therefore use  $\overline{C_{m,u}}$  as the figure of merit to indicate performance of the ODMR contrast measurements, and the analogously defined  $\overline{C_{s,u}} \equiv \overline{C_{s,f}}/S_b(t)$  for ODMR contrast simulations throughout this work. The various defined contrast terms are summarized in Appendix A.

### III. RESULTS

#### A. Beam profile measurements

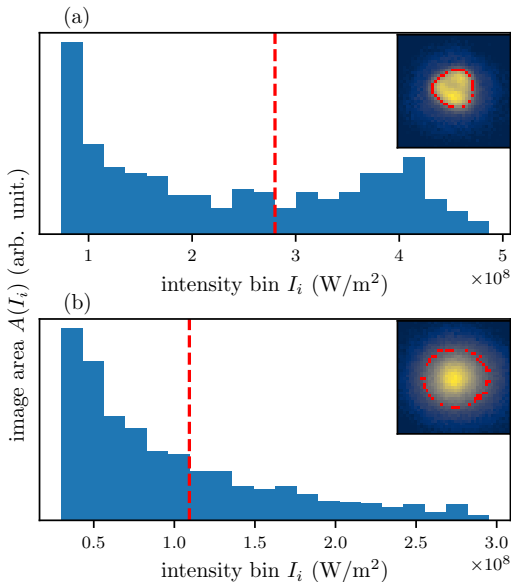


FIG. 4. Fluorescence intensity distribution for optical excitation with (a) a flat shaped beam and (b) a gaussian beam. The area  $A(I_i)$  is proportional to the number of pixels corresponding to the intensity bin  $I_i$ . The insets show the respective fluorescence images with the red boundary noting the ensemble size. The red dashed lines mark the ensemble cutoff intensity.

We characterized both the gaussian and flat shaped optical excitation beam profiles by imaging the ensemble fluorescence onto the camera. In Fig. 4, we show histograms of the distribution of the optical excitation beam intensity over the area in the NV center layer in the diamond. These were created from the ensemble fluorescence images shown in the insets of Fig. 4 taken with reduced laser power, under the assumptions that the fluorescence intensity was linear with the excitation beam intensity, and that the spatial distribution of excitation beam intensity was independent of the total set power.

We neglected the lowest intensity pixels in the fluorescence images due to weak background from stray light and ignored Fresnel reflections on the diamond surfaces.

To compare the sizes of the ensembles optically excited by different intensity profile shapes, we defined a metric for the intensity below which NV centers are driven weakly enough to be neglected. Using both intensity distributions shown in Fig. 4(a,b), we simulated the ODMR contrast measurement of a representative ensemble of NV centers with individual intensities  $I_i$  corresponding to the intensity bins, and we weighted their contribution to the ensemble fluorescence according to the area covered by the pixels in each intensity bin  $A(I_i)$ . The cutoff intensity was defined by starting with the fluorescence  $S_{(b,d)}(t)$  from the brightest intensity bin, then including the fluorescence from subsequently weaker intensity bins until the ODMR contrast of the included fluorescence reached above a threshold fraction of the total ODMR contrast  $\overline{C_{s,f}}$ . The intensity of the last included bin is the cutoff intensity, below which NV centers are not included in the ensemble. Further details of the ensemble size definition are available in the Supplementary Information. The areas of the NV center ensembles are  $630 \mu\text{m}^2$  and  $1600 \mu\text{m}^2$  respectively when optically excited by the flat shaped beam and by the gaussian beam with the spot size yielding the greatest  $\overline{C_{m,u}}$  at the maximum laser power.

#### B. Simulation

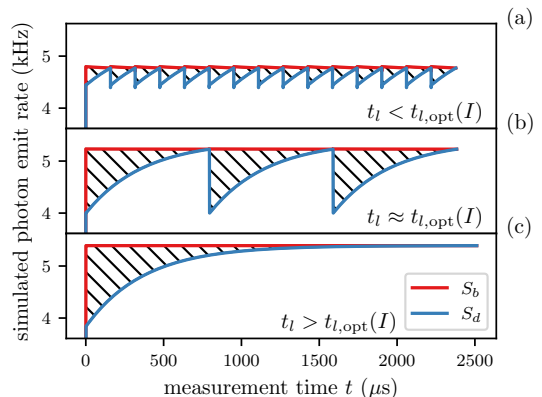


FIG. 5. Simulated fluorescence of an NV center prepared in the bright spin state  $S_b(t)$  and in the dark spin state  $S_d(t)$  with the fluorescence contrast  $C_{s,f}(t)$  shaded in black for (a) a short  $t_l$ , (b) the optimal  $t_l$ , and (c) a long  $t_l$  for the simulated intensity of  $1 \text{ MW/m}^2$ .

Through simulations of our readout protocol, we found two key ways that the inhomogeneous intensity profile of the gaussian beam impairs the ODMR contrast SNR.

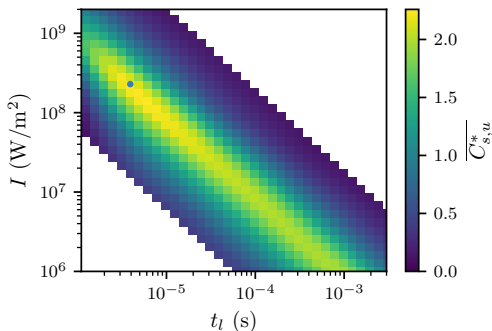


FIG. 6. Simulated mean contrast of a single NV center across multiple regimes of optical excitation intensity. The blue dot indicates the maximum  $\overline{C_{s,u}^*}$ .

The first is that for any given intensity  $I$ , there is an optimal pulse duration  $t_{\text{opt}}(I)$  to maximize a single NV center's mean fractional contrast  $\overline{C_{s,u}^*}$ . A given measurement uses the same  $t_l$  for the whole ensemble, so  $t_l$  differs from  $t_{\text{opt}}(I)$  for most NV centers in an ensemble optically driven by a beam with an inhomogeneous intensity profile. In Fig. 5, we illustrate how a suboptimal  $t_l$  reduces  $\overline{C_{s,u}^*}$  in the low intensity regime  $I < 100 \text{ MW/m}^2$  where the decay from the  $^3\text{E}$  states is much faster than the de-ionization, and the charge state populations remain constant. For the short  $t_l < t_{\text{opt}}(t)$ , the initial contrast  $C_{s,u}^*(0)$  is reduced because there is insufficient time to approach the polarization equilibrium. For the long  $t_l > t_{\text{opt}}(t)$ , measurement time is used inefficiently after repolarization is nearly completed.

In Fig. 6, we show a map of  $\overline{C_{s,u}^*}$  over both the low and high intensity regimes and the relevant range of  $t_l$ . In the low intensity regime, the same maximal  $\overline{C_{s,u}^*}$  can be reached independent of  $I$  as long as  $t_l = t_{\text{opt}}(I)$ . In the high intensity regime, a global maximum of  $\overline{C_{s,u}^*}$  is reached for a particular  $I$  due to charge state dynamics. This maximum occurs at  $230 \text{ MW/m}^2$  in our simulation, which assumes the absorption cross section  $\sigma_g$  to be  $3.1 \times 10^{-21} \text{ m}^{-2}$  as estimated in [27].

Finally, in Fig. 7, we show a comparison between a simulated ensemble optically excited by a beam with a flat intensity profile and one with a gaussian intensity profile in the range of  $I$  and  $t_l$  near the global maxima. This result predicts that the best ensemble mean ODMR contrast  $\overline{C_{s,u}^*}$  achievable with an ideal flat beam profile is 26% greater than that achievable with a gaussian beam profile.

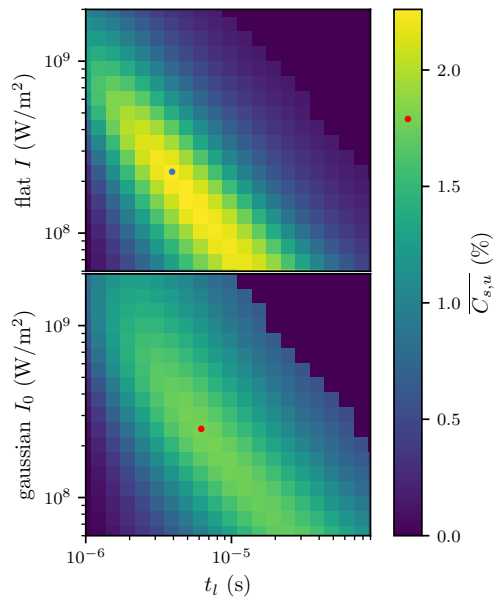


FIG. 7. Simulated mean contrast over a parameter space of intensity and pulse duration near the optima for ensembles optically excited by a flat shaped beam or a gaussian beam. The intensity specified by  $I_0$  is the peak intensity in the center of the beam profile. The red dot indicates the maximum  $\overline{C_{s,u}^*}$  of the gaussian-excited ensemble.

### C. ODMR contrast measurements

We measured the ensemble mean fractional ODMR contrast  $\overline{C_{m,u}}$  of an NV center ensemble addressed by a beam with a gaussian intensity profile with 500 mW of optical power. To vary the intensity, we moved the focusing lens by its translation stage to increase the spot size in the  $25 \mu\text{m}$  thick NV center layer. In Fig. 8, we show  $\overline{C_{m,u}}$  measured over a parameter space of intensity  $I_0$  and pulse duration  $t_l$  near the global optima. The peak intensity  $I_0$  in the center of the gaussian beam profile was estimated for each lens position by fitting the gaussian beam waist in images of the ensemble fluorescence.

The flat-top beam shaper only produces the appropriate intensity distribution in the image plane of the focusing lens, so the spot size could not be dynamically adjusted for the flat beam profile as it was for the gaussian beam profile. In Fig. 9(a), we show  $\overline{C_{m,u}}$  of an NV center ensemble addressed by a beam with the flat shaped profile over a parameter space of  $I$  and  $t_l$ , where  $I$  was adjusted by changing the total laser power. The maximal  $\overline{C_{m,u}}$  is found near the maximal optical excitation power of 500 mW, validating that the spot size resulting from the chosen focal length is appropriate for the avail-

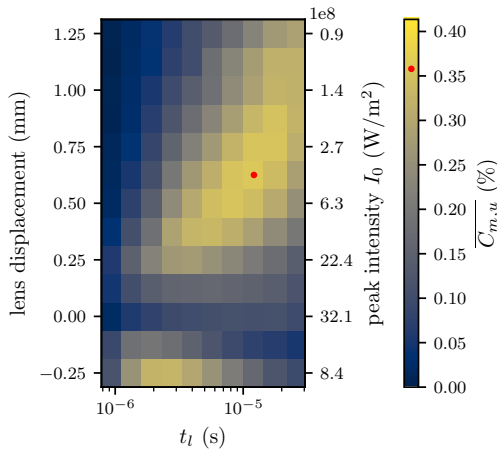


FIG. 8. Mean fractional contrast measured over a range of intensity values by maintaining maximum optical power (500 mW) and displacing the focusing lens from the in-focus position, broadening the gaussian beam’s spot size in the diamond NV layer. Plotted on the same colorbar scale as Fig. 9 with the red dot indicating the maximal  $\overline{C_{m,u}}$ .

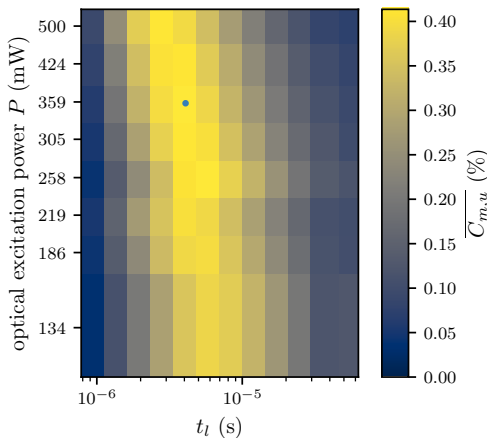


FIG. 9. Mean fractional contrast measured over the parameter space of optical power and pulse duration with the ensemble addressed by the flat shaped beam.

able laser power. The globally maximal ensemble mean ODMR contrast obtained using the flat shaped beam for optical excitation is 13 % greater than that obtained using the gaussian beam, which is made visible by both Figs. 8 and 9 having the same colorbar scale.

#### IV. CONCLUSION

The signal to noise ratio of the spin readout of a large ensemble of NV centers is limited by the available optical excitation power. It is optimized by using an optical intensity near the boundary of the optical saturation regime with a corresponding pulse duration. With a gaussian laser beam, the intensity is inhomogeneous throughout the ensemble, and the optimal pulse duration for the ensemble is inappropriate for the NV centers in the extrema of the intensity distribution, reducing the SNR. Our simulations predict a 26 % improvement with an ideal flat shaped beam compared to a gaussian beam, and empirically we measured a 13 % improvement with a simple flat-top beam shaper.

The optimal ensemble size is defined such that the available laser power is distributed over an area that results in the optimal intensity being applied. We found that the optimal ensemble size was larger for the gaussian beam than for the flat shaped beam by a factor of  $\sim 2.5$  in area.

Because it follows from optical spin repolarization dynamics, this result is generalizable to pulsed sensing schemes with other state preparation steps, such as Ramsey, Hahn-echo or other control pulse sequences applied to large ensembles where total available optical power is the limiting resource.

#### A. LABELED CONTRAST QUANTITIES

$C_{x,f}$	Fluorescence contrast	(V)
$C_{x,s}$	Shot noise-scaled contrast	( $\sqrt{V}$ )
$C_{x,u}$	Unitless (fractional) contrast	(%)
$C_{m,y}$	Measured contrast	
$C_{s,y}$	Simulated contrast	
$C_{x,y}^*$	Individual NV center contrast	
$\overline{C_{x,y}}$	mean contrast	$\frac{1}{t_l} \int_0^{t_l} C_{x,y} dt$

- [1] Marcus W. Doherty, Neil B. Manson, Paul Delaney, Fedor Jelezko, Jörg Wrachtrup, and Lloyd C.L. Hollenberg. The nitrogen-vacancy colour centre in diamond. *Physics Reports*, 528(1):1–45, jul 2013.
- [2] T. Schröder, S. L. Mouradian, J. Zheng, M. E. Trusheim,

- M. Walsh, E. H. Chen, L. Li, I. Bayn, and D. Englund. Quantum nanophotonics in diamond. *J. Opt. Soc. Am. B*, 33(4):B65–B83, 2016.
- [3] Marcus W. Doherty, Victor M. Acosta, Andrey Jarmola, Michael S. J. Barson, Neil B. Manson, Dmitry Budker,

- and Lloyd C. L. Hollenberg. The temperature shifts of the resonances of the NV- center in diamond. *Physical Review B*, 90(4), 2014.
- [4] P. Neumann, I. Jakobi, F. Dolde, C. Burk, R. Reuter, G. Waldherr, J. Honert, T. Wolf, A. Brunner, J. H. Shim, D. Suter, H. Sumiya, J. Isoya, and J. Wrachtrup. High-precision nanoscale temperature sensing using single defects in diamond. *Nano Letters*, 13(6):2738–2742, jun 2013.
- [5] A. M. Wojciechowski, M. Karadas, C. Osterkamp, S. Jankuhn, J. Meijer, F. Jelezko, A. Huck, and U. L. Andersen. Precision temperature sensing in the presence of magnetic field noise and vice-versa using nitrogen-vacancy centers in diamond. *Appl. Phys. Lett.*, 113(1):013502, 2018.
- [6] Marcus W. Doherty, Viktor V. Struzhkin, David A. Simpson, Liam P. McGuinness, Yufei Meng, Alastair Stacey, Timothy J. Karle, Russell J. Hemley, Neil B. Manson, Lloyd C. L. Hollenberg, and Steven Praver. Electronic properties and metrology applications of the diamond  $nv^-$  center under pressure. *Phys. Rev. Lett.*, 112:047601, Jan 2014.
- [7] F. Dolde, H. Fedder, M. W. Doherty, T. Nöbauer, F. Rempp, G. Balasubramanian, T. Wolf, F. Reinhard, L. C. L. Hollenberg, F. Jelezko, and J. Wrachtrup. Electric-field sensing using single diamond spins. *Nature Physics*, 7(6):459–463, apr 2011.
- [8] J H N Loubser and J A van Wyk. Electron spin resonance in the study of diamond. *Reports on Progress in Physics*, 41(8):1201–1248, 1978.
- [9] J. M. Taylor, P. Cappellaro, L. Childress, L. Jiang, D. Budker, P. R. Hemmer, A. Yacoby, R. Walsworth, and M. D. Lukin. High-sensitivity diamond magnetometer with nanoscale resolution. *Nat. Phys.*, 4(10):810–816, 2008.
- [10] J. L. Webb, J. D. Clement, L. Troise, S. Ahmadi, G. J. Johansen, A. Huck, and U. L. Andersen. Nanotesla sensitivity magnetic field sensing using a compact diamond nitrogen-vacancy magnetometer. *Appl. Phys. Lett.*, 114(23):231103, 2019.
- [11] J. L. Webb et al. Optimization of a diamond nitrogen vacancy centre magnetometer for sensing of biological signals. *Frontiers Phys.*, 8:430, 2020.
- [12] John F. Barry, Matthew J. Turner, Jennifer M. Schloss, David R. Glenn, Yuyu Song, Mikhail D. Lukin, Hongkun Park, and Ronald L. Walsworth. Optical magnetic detection of single-neuron action potentials using quantum defects in diamond. *Proceedings of the National Academy of Sciences*, 113(49):14133–14138, 2016.
- [13] D. Le Sage, K. Arai, D. R. Glenn, S. J. DeVience, L. M. Pham, L. Rahn-Lee, M. D. Lukin, A. Yacoby, A. Komeili, and R. L. Walsworth. Optical magnetic imaging of living cells. *Nature*, 496(7446):486–489, apr 2013.
- [14] F Gorrini, R Giri, CE Avalos, S Tambalo, S Mannucci, L Basso, N Bazzanella, C Dorigoni, M Cazzanelli, P Marzola, et al. Fast and sensitive detection of paramagnetic species using coupled charge and spin dynamics in strongly fluorescent nanodiamonds. *ACS applied materials & interfaces*, 11(27):24412–24422, 2019.
- [15] Romana Schirhagl, Kevin Chang, Michael Loretz, and Christian L. Degen. Nitrogen-Vacancy Centers in Diamond: Nanoscale Sensors for Physics and Biology. *Annual Review of Physical Chemistry*, 65(1):83–105, 2014.
- [16] Lucio Robledo, Hannes Bernien, Toeno Van Der Sar, and Ronald Hanson. Spin dynamics in the optical cycle of single nitrogen-vacancy centres in diamond. *New Journal of Physics*, 13(2):025013, 2011.
- [17] Andreas F. L. Poulsen, Joshua D. Clement, James L. Webb, Rasmus H. Jensen, Kirstine Berg-Sørensen, Alexander Huck, and Ulrik Lund Andersen. Optimal control of a nitrogen-vacancy spin ensemble in diamond for sensing in the pulsed domain. 2021.
- [18] A. Dréau, M. Lesik, L. Rondin, P. Spinicelli, O. Arcizet, J. F. Roch, and V. Jacques. Avoiding power broadening in optically detected magnetic resonance of single NV defects for enhanced dc magnetic field sensitivity. *Phys. Rev. B*, 84(19):1–8, 2011.
- [19] J. F. Barry, J. M. Schloss, E. Bauch, M. J. Turner, C. A. Hart, L. M. Pham, and R. L. Walsworth. Sensitivity Optimization for NV-Diamond Magnetometry. *Rev. Mod. Phys.*, 92(1):015004, 2020.
- [20] Sepehr Ahmadi, Haitham A. R. El-Ella, Adam M. Wojciechowski, Tobias Gehring, Jørn O. B. Hansen, Alexander Huck, and Ulrik L. Andersen. Nitrogen-vacancy ensemble magnetometry based on pump absorption. *Physical Review B*, 97(2), 2018.
- [21] Thomas Wolf, Philipp Neumann, Kazuo Nakamura, Hitoshi Sumiya, Takeshi Ohshima, Junichi Isoya, and Jörg Wrachtrup. Subpicotesla Diamond Magnetometry. *Physical Review X*, 5(4), October 2015.
- [22] Khadijeh Bayat, Jennifer Choy, Mahdi Farrokhi Baroughi, Srujan Meesala, and Marko Loncar. Efficient, Uniform, and Large Area Microwave Magnetic Coupling to NV Centers in Diamond Using Double Split-Ring Resonators. *Nano Letters*, 14(3):1208–1213, 2014.
- [23] Y. Dumeige et al. Infrared laser magnetometry with a NV doped diamond intracavity etalon. *Opt. Express*, 27(2):1706, 2019.
- [24] I. Meirzada, Y. Hovav, S. A. Wolf, and N. Bar-Gill. Negative charge enhancement of near-surface nitrogen vacancy centers by multicolor excitation. *Physical Review B*, 98(24), dec 2018.
- [25] VM Acosta, E Bauch, A Jarmola, LJ Zipp, MP Ledbetter, and D Budker. Broadband magnetometry by infrared-absorption detection of nitrogen-vacancy ensembles in diamond. *Applied Physics Letters*, 97(17):174104, 2010.
- [26] JP Tetienne, L Rondin, P Spinicelli, M Chipaux, T Debuisschert, JF Roch, and V Jacques. Magnetic-field-dependent photodynamics of single nv defects in diamond: an application to qualitative all-optical magnetic imaging. *New Journal of Physics*, 14(10):103033, 2012.
- [27] T.-L. Wee, Y.-K. Tzeng, C.-C. Han, H.-C. Chang, W. Fann, J.-H. Hsu, K.-M. Chen, and Y.-C. Yu. Two-photon excited fluorescence of nitrogen-vacancy centers in proton-irradiated type Ib diamond. *The Journal of Physical Chemistry A*, 111(38):9379–9386, 2007.
- [28] N Aslam, G Waldherr, P Neumann, F Jelezko, and J Wrachtrup. Photo-induced ionization dynamics of the nitrogen vacancy defect in diamond investigated by single-shot charge state detection. *New Journal of Physics*, 2013.
- [29] G Waldherr, J Beck, M Steiner, P Neumann, A Gali, Th Frauenheim, F Jelezko, and J Wrachtrup. Dark states of single nitrogen-vacancy centers in diamond unraveled by single shot nmr. *Physical review letters*, 106(15):157601, 2011.

- [30] David A. Hopper, Henry J. Shulevitz, and Lee C. Bassett. Spin readout techniques of the nitrogen-vacancy center in diamond. *Micromachines*, 9(9), 2018.

## 6.3 Supplementary Information

## I. SIMULATION

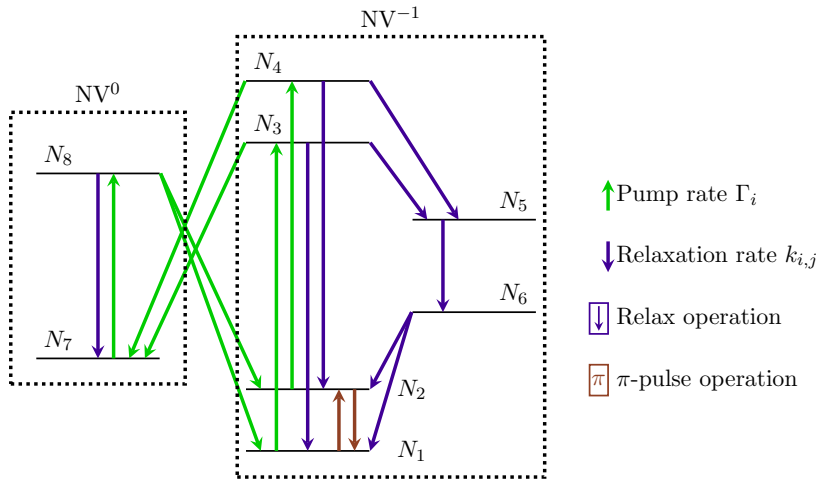


FIG. 1. Full 8-level model used in simulations. The ODE solver considering the time evolution of the state under a pump field models the pumped transitions, shown in green, and the relaxation transitions shown in purple. The relaxation operation instantaneously transfers all of the population from the excited states ( $N_3, N_4, N_5, N_6, N_8$ ) to their destinations. The  $\pi$ -pulse operation instantaneously transfers population between  $N_1$ , and  $N_2$ .

The 8-level model used in simulations of the NV center repolarization and readout is depicted in Fig 1. Only the state populations (i.e. no phase) are considered, because the green optical excitation is nonresonant, and the dynamics of the coherent MW drive by which the  $\pi$ -pulse is implemented are unimportant for the inquiry at hand. Therefore, the state of the NV center at any time is expressed in a real-valued vector of level populations  $\mathcal{N} \equiv [N_1, N_2, \dots, N_8]^T$ .

States  $N_1$  and  $N_2$  represent the  $m_s=0$  and  $m_s=-1$  levels of the optical ground state  ${}^3A_2$ .  $N_3$  and  $N_4$  are the  $m_s=0$  and  $m_s=-1$  optical excited  ${}^3E$  states.  $N_5$  is the short-lived  ${}^1A$  state which decays to the metastable shelving state  $N_6$ .  $N_7$  and  $N_8$  are the optical ground and excited states of the neutral charge  $NV^0$ .

Relax	rate	Relax	rate	Pump	$I$ -scaled rate
$k_{3,1}$	66 MHz	$k_{5,6}$	1 GHz	$\Gamma_g$	$I \times 8.06 \times 10^{-3} \text{ m}^2/\text{W}$
$k_{4,2}$	65 MHz	$k_{6,1}$	1 MHz	$\Gamma_{g0}$	$I \times 14.51 \times 10^{-3} \text{ m}^2/\text{W}$
$k_{3,5}$	7.9 MHz	$k_{6,2}$	0.7 MHz	$\Gamma_i$	$I \times 25.53 \times 10^{-3} \text{ m}^2/\text{W}$
$k_{4,5}$	53 MHz	$k_{8,7}$	53 MHz	$\Gamma_l$	$I \times 26.34 \times 10^{-3} \text{ m}^2/\text{W}$

TABLE I. Rates used in simulation

### A. Implementation

The evolution of the NV level populations from  $t = 0$  to  $t = t_l$  of an optical pulse is solved with an ordinary differential equation solver using linear rate equations that represent excitation and relaxation processes. The rates used are shown in Table I.

Each update step of the ODE calculates the derivatives of the NV level populations as

$$\begin{bmatrix} N_1 \\ N_2 \\ N_3 \\ N_4 \\ N_5 \\ N_6 \\ N_7 \\ N_8 \end{bmatrix}' = \begin{bmatrix} -W_g & 0 & k_{3,1} & 0 & 0 & k_{6,1} & 0 & W_r/2 \\ 0 & -W_g & 0 & k_{4,2} & 0 & k_{6,2} & 0 & W_r/2 \\ W_g & 0 & -k_{N3} & 0 & 0 & 0 & 0 & 0 \\ 0 & W_g & 0 & -k_{N4} & 0 & 0 & 0 & 0 \\ 0 & 0 & k_{3,5} & k_{4,5} & -k_{5,6} & 0 & 0 & 0 \\ 0 & 0 & 0 & 0 & k_{5,6} & -k_{N6} & 0 & 0 \\ 0 & 0 & W_i & W_i & 0 & 0 & -W_{g0} & k_{8,7} \\ 0 & 0 & 0 & 0 & 0 & 0 & W_g & -k_{N8} \end{bmatrix} \begin{bmatrix} N_1 \\ N_2 \\ N_3 \\ N_4 \\ N_5 \\ N_6 \\ N_7 \\ N_8 \end{bmatrix} \quad (1)$$

with  $k_{N3} = k_{3,1} + k_{3,5} + W_i$ ,  $k_{N4} = k_{4,2} + k_{4,5} + W_i$ ,  $k_{N6} = k_{6,1} - k_{6,2}$ , and  $k_{N8} = k_{8,7} + W_r$ .

The relax operator is implemented as

$$N_{1f} = N1 + \frac{N_3(k_{3,1} + k_{3,5}k_{6,1}/k_{N6})}{k_{N3}} + \frac{N_4k_{4,5}k_{6,1}}{k_{N4}k_{N6}} \quad (2)$$

$$N_{2f} = N2 + \frac{N_3k_{3,5}k_{6,1}}{k_{N3}k_{N6}} + \frac{N_4(k_{4,2} + k_{4,5}k_{6,1}/k_{N6})}{k_{N4}} \quad (3)$$

$$N_{7f} = N_7 + N_8 \quad (4)$$

$$N_{3f}, N_{4f}, N_{5f}, N_{6f}, N_{8f} = 0 \quad (5)$$

and the  $\pi$ -pulse with fidelity  $F$  as

$$\begin{bmatrix} N_1 \\ N_2 \end{bmatrix}_f = \begin{bmatrix} 1 - F & F \\ F & 1 - F \end{bmatrix} \begin{bmatrix} N_1 \\ N_2 \end{bmatrix} \quad (6)$$

The fluorescence  $\mathcal{F}(t)$  is calculated from  $\mathcal{N}(t)$  via the fluorescing excited state populations and their fluorescence rates

$$\mathcal{F}(t) \equiv k_{3,1}N_3 + k_{4,2}N_4 \quad (7)$$

Note that though the  $N_3$  and  $N_4$  states fluoresce at similar rates ( $k_{3,1} \approx k_{4,2}$ ), the greater chance of nonradiative decay of the  $N_4$  state ( $k_{4,5} > k_{3,5}$ ) causes it to be dark by depleting its population more quickly.

### B. High intensity regime

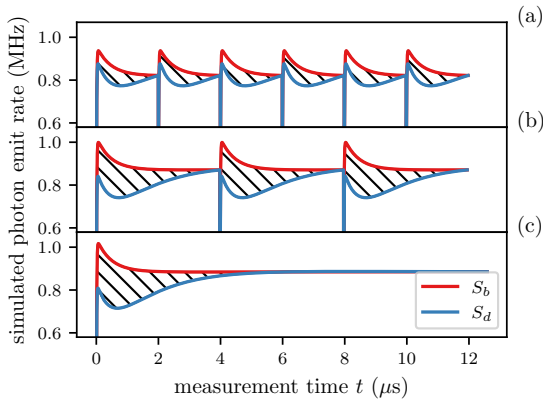


FIG. 2. Simulated single-NV fluorescence  $S_b(t)$  and  $S_d(t)$  with  $C_{s,f}(t)$  shaded in black using the intensity  $I$  that yields the greatest mean contrast  $\overline{C_{s,u}}$  with a (a) short, (b) optimal, and (c) long  $t_l$ . In this intensity regime, charge state dynamics have a strong impact on the shape of the fluorescence curve and increase the maximal  $\overline{C_{s,u}}$  compared to the low intensity regime. The tradeoff between loss of  $C_{s,u}(0)$  and the inefficient long tail as a function of  $t_l$  plays the same role in this intensity regime as in the low intensity regime.

## II. DETAILED SETUP DESCRIPTION

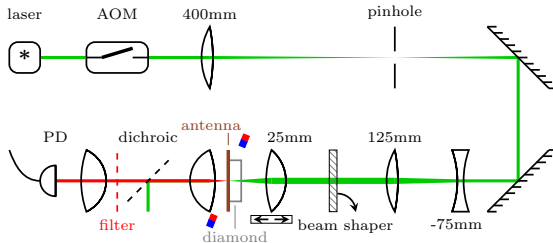


FIG. 3. Optical setup with lenses labeled by focal length. The first-order AOM mode is selected, expanded to a 4mm waist diameter, collimated, passed through the flat-top beam shaper, and focused onto the antenna-mounted diamond by the 25mm focal length lens mounted on a translation stage. The fluorescence from the back side of the diamond is collimated, separated from the pump light, and focused onto the detector.

### III. SUPPLEMENTAL MEASUREMENTS

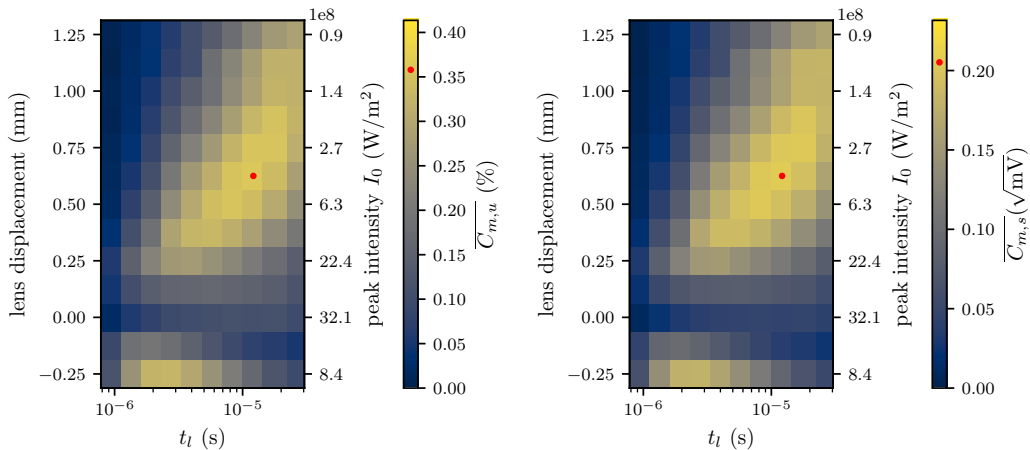


FIG. 4. (left) Mean unitless contrast  $\overline{C_{m,u}}$  and (right) mean shot noise-scaled contrast  $\overline{C_{m,s}}$  measured over a range of intensity values by maintaining maximum pump power (500 mW) and displacing the focusing lens from the focus, broadening the gaussian beam's spot size. Because the total power used is constant,  $\overline{C_{m,u}}$  is a very good linear approximate of  $\overline{C_{m,s}}$ .

### A. Ensemble area definition

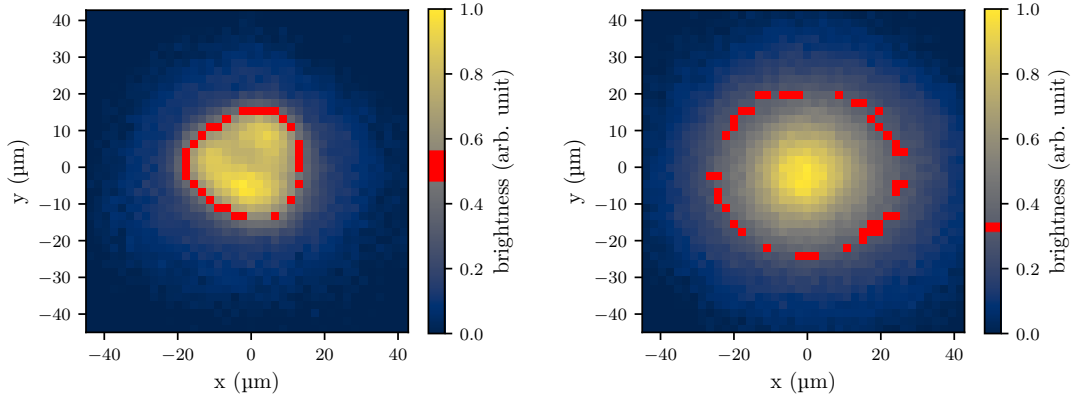


FIG. 5. Enlarged fluorescence images from main text Fig. 4 for the ensemble addressed by (left) the flat beam and (right) the gaussian beam. The intensity values marked in red indicate the boundary between the NV centers included in the ensemble and those outside of it.

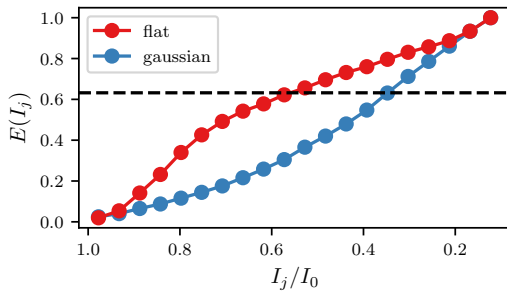


FIG. 6. Simulated cumulative  $\overline{C_{s,f}^*}$  contrast signal  $E(I_j)$  over the beam profile intensity bins from the peak intensity ( $I_i = I_0$ ) out towards the periphery ( $I_i = I_{n-1}$ ) for the  $n$  intensity bins depicted in main text Fig. 4. The threshold  $T$  is shown by the black, dashed line.

We simulated the ODMR contrast of representative ensembles optically excited by the flat shaped and gaussian beam intensity distributions shown in the main text Fig. 4. The representative ensemble consisted of one NV center per intensity bin  $I_i$ , and the ensemble

fluorescence  $S_{(b,d)}(t)$  was the sum of the fluorescence from each NV center weighted by the image area  $A(I_i)$ . We performed the simulation for a range of pulse durations  $t_l$  and selected the  $t_l$  which yielded the greatest mean ensemble contrast  $\overline{C_{s,u}}$ . For that  $t_l$ , we considered what fraction of the total contrast signal  $\overline{C_{s,f}} = \sum_{i=0}^{n-1} \overline{C_{s,f}^*(I_i)} A(I_i)$  was reached by summing over the  $i$  most intense bins. We defined the ensemble fluorescence contrast fraction  $E(I_i)$  as

$$E(I_j) \equiv \frac{\sum_{i=0}^j \overline{C_{s,f}^*(I_i)} A(I_i)}{\overline{C_{s,f}}} \quad (8)$$

and show this as a function of  $I_j$  in Fig. 6.

The ensemble size is defined as that area which is necessary to include in order to reach  $E(I_j) > T$  for an arbitrary threshold  $T$ . Having chosen  $T = 1 - e^{-1}$  for both beam shapes, we found that the ensemble included intensity down to  $I_j/I_0 = 57\%$  for the flat shaped beam and down to  $I_j/I_0 = 35\%$  for the gaussian beam. The flat shaped beam has greater uniformity of intensity within the ensemble (i.e. a higher cutoff intensity) for any value of  $T$ .

# Conclusion

---

In this project, some of the key challenges related to using large ensembles of NV centers for magnetometry in biophysical research settings have been addressed. In Chapter 4, it was shown that a high-sensitivity magnetometry setup can be made compact and manipulable. The subsequent work in Chapters 5 and 6 are just as suitable for inclusion in such a compact sensing device.

The optimal control technique explored in Chapter 5 and the beam shaping for more homogeneous readout and repolarization explored in Chapter 6 address both of the physical difficulties related to the scaling of per-volume sensitivity, namely how MW and optical fields are distributed throughout the volume.

In Chapter 6, we showed that there is an optimal optical intensity for maximizing the SNR of the ODMR contrast readout due to the shape of the fluorescence signal during repolarization with charge state dynamics in the high intensity regime. With finite total laser power, this means that there is an optimal NV ensemble area, which for the 500 mW laser beam we used was  $630 \mu\text{m}^2$ . The total number of NV centers that could be addressed with this approach would be limited by the thickness of the NV center layer, which would need to be thin enough to avoid inhomogeneous intensity due to absorption loss, and the NV density, which may need to be kept in the  $\lesssim 10$  ppm regime [71] where our model assumptions may not be valid.

For the optimal control methods explored in Chapter 5, we used a large MW antenna meant to deliver power evenly in a  $\sim 0.2 \text{mm}^2$  area, which is  $\sim 100\times$  larger than the optimal ensemble area for the magnitude of green laser power that is typically available. The main limitation of our optimal control protocol was our low Rabi frequency  $\Omega = 3.4 \text{MHz}$  compared to the 10-30 MHz commonly reported with wire loop MW antennas [26, 72, 73] due to the larger area over which the available MW power was distributed. With the greater  $\Omega$  that follows from more MW intensity (the same power over a smaller area), it would be possible to correct for a larger range of inhomogeneities in MW intensity and in resonance frequency with a much shorter MW pulse duration.

Besides the inhomogeneity of MW and laser intensity, the main limitation in using pulsed NV sensing schemes for large ensembles is the measurement overhead [43]. The best achievable per-NV DC sensitivity in the ideal case is with a Ramsey magnetometry sequence, where the sensitivity scales with  $1/T_2^*$ , but if  $T_2^*$  is short compared to the time spent applying MW and laser pulses, then only a minor fraction of the measurement time is spent accumulating phase from the magnetic field. One

of our findings in the work in Chapter 6 is that with the green laser intensity that maximizes the shot noise-limited SNR of the optical spin readout, the appropriate laser pulse duration is  $\sim 4 \mu\text{s}$ . This is much less than the  $T_2^* = 29 \mu\text{s}$  demonstrated in [5] in a diamond with fairly high 750 ppb NV density, which puts it in the low-overhead regime where Ramsey magnetometry is beneficial.

With laser beam shaping and MW optimal control, the regime of ensemble area for which pulsed sensing is viable (as opposed to continuous wave methods) can be extended to  $\sim 630 \mu\text{m}^2$  for green laser power commonly used in NV ensemble experiments. This is larger than the ensemble areas reported in [5] and comparable to the ensemble area in [42], while they both reported using significantly longer repolarization times. This is a smaller ensemble area than that used in larger CW-driven ensembles as in [74], but recent successes with ferrite flux concentrators [75, 76] could be a better way to gain sensitivity at the expense of spatial resolution for biophysical measurements. For such setups, the techniques explored in this work are useful tools to maximize the shot noise-limited SNR with the available laser power.

# Appendices



# APPENDIX A

## Rabi oscillation animation

---

To help the student or lay reader to visualize how a microwave pulse rotates the spin state on the Bloch sphere, I made a video illustration which is viewable at <https://sciencedata.dk/shared/9402b213c297fb2f77a50f211e727b9e>. It is also mirrored on IPFS with the hash QmSXfECg2Qaj2P4K95rymDrLNmJEiUUvv7RXGE1TJi49QK. It was made with the QuTiP package [77].

In the animation, the spin state (black arrow) is being controlled by the magnetic component of the MW field (brown arrow) with constant phase and amplitude. For the resonant case, where  $\Delta = 0$ , the spin's precession remains in phase with the MW drive frequency, and the spin is rotated all the way from the bright state  $|0\rangle$  to the dark state  $|-1\rangle$ .

For the nonresonant case  $\Delta \neq 0$ , the spin drifts out of phase and never reaches a full population transfer into the dark state. The simulated MW field amplitude is identical, so it drives the spin at the same rate, but the spin state returns to  $|0\rangle$  sooner than in the resonant case because it has less distance to cover on the Bloch sphere in the rotating frame.

In this video, the Rabi frequency is unrealistically high compared to the MW drive frequency. In our experiments, the MW drive frequency is  $\sim 1000\times$  faster than the Rabi frequency, meaning  $\sim 1000$  oscillations of the MW field elapse before the spin state would make a full rotation around the Bloch sphere.

This depicts the simplest case of an unshaped MW control pulse. In terms of IQ modulation which we use to describe our optimal control pulse in Chapter 5, this can be described as  $I(t) = C, Q(t) = 0$ . Throughout the video, it rotates the spin state in the same direction around the  $\hat{x}$  axis at a constant rate. The shaped pulses with varying IQ modulation components make varying rotations about the  $\hat{x}$  and  $\hat{y}$  axes throughout the pulse duration.



# Bibliography

---

- [1] J. Achard, V. Jacques, and A. Tallaire, “Chemical vapour deposition diamond single crystals with nitrogen-vacancy centres: a review of material synthesis and technology for quantum sensing applications,” *Journal of Physics D: Applied Physics*, vol. 53, p. 313001, may 2020.
- [2] J. M. Schloss, J. F. Barry, M. J. Turner, and R. L. Walsworth, “Simultaneous Broadband Vector Magnetometry Using Solid-State Spins,” *Physical Review Applied*, vol. 10, Sept. 2018.
- [3] V. M. Acosta, E. Bauch, M. P. Ledbetter, C. Santori, K.-M. C. Fu, P. E. Barclay, R. G. Beausoleil, H. Linget, J. F. Roch, F. Treussart, S. Chemerisov, W. Gawlik, and D. Budker, “Diamonds with a high density of nitrogen-vacancy centers for magnetometry applications,” *Physical Review B*, vol. 80, sep 2009.
- [4] N. Mizuochi, P. Neumann, F. Rempp, J. Beck, V. Jacques, P. Siyushev, K. Nakamura, D. J. Twitchen, H. Watanabe, S. Yamasaki, F. Jelezko, and J. Wrachtrup, “Coherence of single spins coupled to a nuclear spin bath of varying density,” *Physical Review B*, vol. 80, jul 2009.
- [5] E. Bauch, C. A. Hart, J. M. Schloss, M. J. Turner, J. F. Barry, P. Kehayias, S. Singh, and R. L. Walsworth, “Ultralong Dephasing Times in Solid-State Spin Ensembles via Quantum Control,” *Physical Review X*, vol. 8, July 2018.
- [6] E. E. Kleinsasser, M. Stanfield, J. K. Q. Banks, Z. Zhu, W.-D. Li, V. Acosta, H. Watanabe, K. Itoh, and K. Fu, “High density nitrogen-vacancy sensing surface created via he+ ion implantation of 12c diamond,” *Applied Physics Letters*, vol. 108, p. 202401, 2016.
- [7] A. Gali, M. Fyta, and E. Kaxiras, “Ab initio supercell calculations on nitrogen-vacancy center in diamond: Electronic structure and hyperfine tensors,” *Physical Review B*, vol. 77, apr 2008.
- [8] V. M. Acosta, A. Jarmola, E. Bauch, and D. Budker, “Optical properties of the nitrogen-vacancy singlet levels in diamond,” *Physical Review B*, vol. 82, Nov. 2010.

- [9] C. Kurtsiefer, S. Mayer, P. Zarda, and H. Weinfurter, “Stable solid-state source of single photons,” *Physical Review Letters*, no. molecules, 2000.
- [10] Á. Gali, “Ab initio theory of the nitrogen-vacancy center in diamond,” *Nanophotonics*, vol. 8, pp. 1907–1943, sep 2019.
- [11] J. R. Maze, A. Gali, E. Togan, Y. Chu, A. Trifonov, E. Kaxiras, and M. D. Lukin, “Properties of nitrogen-vacancy centers in diamond: the group theoretic approach,” *New Journal of Physics*, vol. 13, no. 2, p. 025025, 2011.
- [12] M. W. Doherty, N. B. Manson, P. Delaney, F. Jelezko, J. Wrachtrup, and L. C. Hollenberg, “The nitrogen-vacancy colour centre in diamond,” *Physics Reports*, vol. 528, pp. 1–45, jul 2013.
- [13] L. Robledo, H. Bernien, T. Van Der Sar, and R. Hanson, “Spin dynamics in the optical cycle of single nitrogen-vacancy centres in diamond,” *New Journal of Physics*, vol. 13, no. 2, p. 025013, 2011.
- [14] G. Thiering and A. Gali, “Theory of the optical spin-polarization loop of the nitrogen-vacancy center in diamond,” *Physical Review B*, vol. 98, no. 8, p. 085207, 2018.
- [15] R. U. A. Khan, P. M. Martineau, B. L. Cann, M. E. Newton, and D. J. Twitchen, “Charge transfer effects, thermo and photochromism in single crystal CVD synthetic diamond,” *Journal of Physics: Condensed Matter*, vol. 21, p. 364214, aug 2009.
- [16] G. Kucsko, P. C. Maurer, N. Y. Yao, M. Kubo, H. J. Noh, P. K. Lo, H. Park, and M. D. Lukin, “Nanometre-scale thermometry in a living cell,” *Nature*, vol. 500, no. 7460, pp. 54–58, 2013.
- [17] M. W. Doherty, V. M. Acosta, A. Jarmola, M. S. J. Barson, N. B. Manson, D. Budker, and L. C. L. Hollenberg, “The temperature shifts of the resonances of the NV<sup>-</sup> center in diamond,” *Physical Review B*, vol. 90, July 2014.
- [18] M. W. Doherty, V. V. Struzhkin, D. A. Simpson, L. P. McGuinness, Y. Meng, A. Stacey, T. J. Karle, R. J. Hemley, N. B. Manson, L. C. L. Hollenberg, and S. Prawer, “Electronic properties and metrology applications of the diamond nv<sup>-</sup> center under pressure,” *Phys. Rev. Lett.*, vol. 112, p. 047601, Jan 2014.
- [19] J. H. N. Loubser and J. A. van Wyk, “Electron spin resonance in the study of diamond,” *Reports on Progress in Physics*, vol. 41, pp. 1201–1248, Aug. 1978.
- [20] H. A. R. El-Ella, S. Ahmadi, A. M. Wojciechowski, A. Huck, and U. L. Andersen, “Optimised frequency modulation for continuous-wave optical magnetic resonance sensing using nitrogen-vacancy ensembles,” *Optics Express*, vol. 25, p. 14809, June 2017.

- [21] R. Schirhagl, K. Chang, M. Loretz, and C. L. Degen, “Nitrogen-Vacancy Centers in Diamond: Nanoscale Sensors for Physics and Biology,” *Annual Review of Physical Chemistry*, vol. 65, pp. 83–105, Apr. 2014.
- [22] M. L. Goldman, A. Sipahigil, M. Doherty, N. Y. Yao, S. Bennett, M. Markham, D. Twitchen, N. Manson, A. Kubanek, and M. D. Lukin, “Phonon-induced population dynamics and intersystem crossing in nitrogen-vacancy centers,” *Physical review letters*, vol. 114, no. 14, p. 145502, 2015.
- [23] A. Gruber, A. Dräbenstedt, C. Tietz, L. Fleury, J. Wrachtrup, and C. von Borczyskowski, “Scanning confocal optical microscopy and magnetic resonance on single defect centers,” *Science*, vol. 276, no. 5321, pp. 2012–2014, 1997.
- [24] C. Gerry and P. Knight, *Introductory Quantum Optics*. Cambridge University Press, 2004.
- [25] L. E. Ballentine, *Quantum Mechanics, A Modern Development*. World Scientific Publishing, 1998.
- [26] T. Nöbauer, A. Angerer, B. Bartels, M. Trupke, S. Rotter, J. Schmiedmayer, F. Mintert, and J. Majer, “Smooth Optimal Quantum Control for Robust Solid-State Spin Magnetometry,” *Physical Review Letters*, vol. 115, p. 190801, Nov. 2015.
- [27] J.-P. Tetienne, T. Hingant, L. Rondin, A. Cavallès, L. Mayer, G. Dantelle, T. Gacoin, J. Wrachtrup, J.-F. Roch, and V. Jacques, “Spin relaxometry of single nitrogen-vacancy defects in diamond nanocrystals for magnetic noise sensing,” *Physical Review B*, vol. 87, no. 23, p. 235436, 2013.
- [28] S. Steinert, F. Ziem, L. T. Hall, A. Zappe, M. Schweikert, N. Götz, A. Aird, G. Balasubramanian, L. Hollenberg, and J. Wrachtrup, “Magnetic spin imaging under ambient conditions with sub-cellular resolution,” *Nature Communications*, vol. 4, mar 2013.
- [29] N. Bar-Gill, L. Pham, A. Jarmola, D. Budker, and R. Walsworth, “Solid-state electronic spin coherence time approaching one second,” *Nature Communications*, vol. 4, p. 1743, June 2013.
- [30] L. M. Pham, N. Bar-Gill, C. Belthangady, D. Le Sage, P. Cappellaro, M. D. Lukin, A. Yacoby, and R. L. Walsworth, “Enhanced solid-state multispin metrology using dynamical decoupling,” *Physical Review B*, vol. 86, no. 4, p. 045214, 2012.
- [31] E. Bauch, S. Singh, J. Lee, C. A. Hart, J. M. Schloss, M. J. Turner, J. F. Barry, L. M. Pham, N. Bar-Gill, S. F. Yelin, and et al., “Decoherence of ensembles of nitrogen-vacancy centers in diamond,” *Physical Review B*, vol. 102, Oct 2020.

- [32] E. D. Herbschleb, H. Kato, Y. Maruyama, T. Danjo, T. Makino, S. Yamasaki, I. Ohki, K. Hayashi, H. Morishita, M. Fujiwara, and N. Mizuochi, “Ultra-long coherence times amongst room-temperature solid-state spins,” *Nature Communications*, vol. 10, p. 3766, Aug 2019.
- [33] C. Zhang, F. Shagieva, M. Widmann, M. Kübler, V. Vorobyov, P. Kapitanova, E. Nenasheva, R. Corkill, O. Rhrle, K. Nakamura, H. Sumiya, S. Onoda, J. Isoya, and J. Wrachtrup, “Diamond magnetometry and gradiometry towards subpicotesla dc field measurement,” *Phys. Rev. Applied*, vol. 15, p. 064075, Jun 2021.
- [34] B. J. Shields, Q. P. Unterreithmeier, N. P. de Leon, H. Park, and M. D. Lukin, “Efficient readout of a single spin state in diamond via spin-to-charge conversion,” *Physical review letters*, vol. 114, no. 13, p. 136402, 2015.
- [35] D. A. Hopper, H. J. Shulevitz, and L. C. Bassett, “Spin readout techniques of the nitrogen-vacancy center in diamond,” *Micromachines*, vol. 9, no. 9, 2018.
- [36] J. M. Taylor, P. Cappellaro, L. Childress, L. Jiang, D. Budker, P. R. Hemmer, A. Yacoby, R. Walsworth, and M. D. Lukin, “High-sensitivity diamond magnetometer with nanoscale resolution,” *Nature Physics*, vol. 4, pp. 810–816, Oct. 2008.
- [37] A. Dréau, M. Lesik, L. Rondin, P. Spinicelli, O. Arcizet, J.-F. Roch, and V. Jacques, “Avoiding power broadening in optically detected magnetic resonance of single NV defects for enhanced DC-magnetic field sensitivity,” *Physical Review B*, vol. 84, Nov. 2011.
- [38] N. F. Ramsey, “A molecular beam resonance method with separated oscillating fields,” *Phys. Rev.*, vol. 78, pp. 695–699, Jun 1950.
- [39] L. M. Vandersypen and I. L. Chuang, “Nmr techniques for quantum control and computation,” *Reviews of modern physics*, vol. 76, no. 4, p. 1037, 2005.
- [40] E. L. Hahn, “Spin echoes,” *Physical review*, vol. 80, no. 4, p. 580, 1950.
- [41] J. R. Maze, P. L. Stanwix, J. S. Hodges, S. Hong, J. M. Taylor, P. Cappellaro, L. Jiang, M. V. G. Dutt, E. Togan, A. S. Zibrov, A. Yacoby, R. L. Walsworth, and M. D. Lukin, “Nanoscale magnetic sensing with an individual electronic spin in diamond,” *Nature*, vol. 455, pp. 644–647, Oct. 2008.
- [42] T. Wolf, P. Neumann, K. Nakamura, H. Sumiya, T. Ohshima, J. Isoya, and J. Wrachtrup, “Subpicotesla Diamond Magnetometry,” *Physical Review X*, vol. 5, Oct. 2015.
- [43] J. F. Barry, J. M. Schloss, E. Bauch, M. J. Turner, C. A. Hart, L. M. Pham, and R. L. Walsworth, “Sensitivity optimization for nv-diamond magnetometry,” *Reviews of Modern Physics*, vol. 92, no. 1, p. 015004, 2020.

- [44] S. Ahmadi, H. A. R. El-Ella, A. M. Wojciechowski, T. Gehring, J. O. B. Hansen, A. Huck, and U. L. Andersen, "Nitrogen-vacancy ensemble magnetometry based on pump absorption," *Physical Review B*, vol. 97, Jan. 2018.
- [45] J. L. Webb, L. Troise, N. W. Hansen, C. Olsson, A. M. Wojciechowski, J. Achard, O. Brinza, R. Staacke, M. Kieschnick, J. Meijer, A. Thielscher, J.-F. Perrier, K. Berg-Sørensen, A. Huck, and U. L. Andersen, "Detection of biological signals from a live mammalian muscle using an early stage diamond quantum sensor," *Scientific Reports*, vol. 11, Jan. 2021.
- [46] "Microsoft word - pnas neuron manuscript arxiv v9 no refs.docx."
- [47] K. Jensen, V. M. Acosta, A. Jarmola, and D. Budker, "Light narrowing of magnetic resonances in ensembles of nitrogen-vacancy centers in diamond," *Physical Review B*, vol. 87, Jan. 2013.
- [48] D. P. Blair and P. H. Sydenham, "Phase sensitive detection as a means to recover signals buried in noise," *Journal of Physics E: Scientific Instruments*, vol. 8, pp. 621–627, Aug. 1975.
- [49] I. Meirzada, Y. Hovav, S. A. Wolf, and N. Bar-Gill, "Negative charge enhancement of near-surface nitrogen vacancy centers by multicolor excitation," *Physical Review B*, vol. 98, Dec. 2018.
- [50] T.-L. Wee, Y.-K. Tzeng, C.-C. Han, H.-C. Chang, W. Fann, J.-H. Hsu, K.-M. Chen, and Y.-C. Yu, "Two-photon excited fluorescence of nitrogen-vacancy centers in proton-irradiated type Ib diamond," *The Journal of Physical Chemistry A*, vol. 111, no. 38, pp. 9379–9386, 2007.
- [51] B. Saleh and M. Teich, *Fundamentals of Photonics*. Wiley, third ed., 2019.
- [52] A. M. Wojciechowski, M. Karadas, C. Osterkamp, S. Jankuhn, J. Meijer, F. Jelezko, A. Huck, and U. L. Andersen, "Precision temperature sensing in the presence of magnetic field noise and *vice-versa* using nitrogen-vacancy centers in diamond," *Applied Physics Letters*, vol. 113, p. 013502, July 2018.
- [53] J. Tetienne, L. Rondin, P. Spinicelli, M. Chipaux, T. Debuisschert, J. Roch, and V. Jacques, "Magnetic-field-dependent photodynamics of single NV defects in diamond: an application to qualitative all-optical magnetic imaging," *New Journal of Physics*, vol. 14, no. 10, p. 103033, 2012.
- [54] R. Jaklevic, J. Lambe, A. Silver, and J. Mercereau, "Quantum interference effects in Josephson tunneling," *Physical Review Letters*, vol. 12, no. 7, p. 159, 1964.
- [55] J. Clarke and A. I. Braginski, eds., *The SQUID Handbook*. Weinheim: Wiley-VCH, 2004.

- [56] J. Clarke, Y.-H. Lee, and J. Schneiderman, “Focus on squids in biomagnetism,” *Supercond. Sci. Technol.*, vol. 31, p. 080201, 2018.
- [57] D. Budker and M. Romalis, “Optical magnetometry,” *Nature Physics*, vol. 3, pp. 227–234, Apr 2007.
- [58] I. Kominis, T. Kornack, J. Allred, and M. V. Romalis, “A subfemtotesla multi-channel atomic magnetometer,” *Nature*, vol. 422, no. 6932, pp. 596–599, 2003.
- [59] V. Schultze, B. Schillig, R. IJsselsteijn, T. Scholtes, S. Woetzel, and R. Stolz, “An optically pumped magnetometer working in the light-shift dispersed mz mode,” *Sensors*, vol. 17, no. 3, p. 561, 2017.
- [60] S. Ahmadi, “Continuous-Wave Magnetic Field Sensing with Nitrogen-Vacancy Centers in Diamond,” p. 111, 2018.
- [61] G. J. Johansen, A. Huck, U. L. Andersen, and S. Ahmadi, “Handheld Diamond Magnetic Field Sensor,” p. 72, 2018.
- [62] F. M. Stürner, A. Brenneis, J. Kassel, U. Wostradowski, R. Rölver, T. Fuchs, K. Nakamura, H. Sumiya, S. Onoda, J. Isoya, and F. Jelezko, “Compact integrated magnetometer based on nitrogen-vacancy centres in diamond,” *Diamond and Related Materials*, vol. 93, pp. 59–65, Mar. 2019.
- [63] R. Patel, L. Zhou, A. Frangeskou, G. Stimpson, B. Breeze, A. Nikitin, M. Dale, E. Nichols, W. Thornley, B. Green, *et al.*, “Subnanotesla magnetometry with a fiber-coupled diamond sensor,” *Physical Review Applied*, vol. 14, no. 4, p. 044058, 2020.
- [64] G. Chatzidrosos, J. S. Rebeirro, H. Zheng, M. Omar, A. Brenneis, F. M. Stürner, T. Fuchs, T. Buck, R. Rölver, T. Schneemann, P. Blümler, D. Budker, and A. Wickenbrock, “Fiberized diamond-based vector magnetometers,” *Frontiers in Photonics*, vol. 2, p. 4, 2021.
- [65] S. Ahmadi, H. A. R. El-Ella, J. O. B. Hansen, A. Huck, and U. L. Andersen, “Pump-Enhanced Continuous-Wave Magnetometry Using Nitrogen-Vacancy Ensembles,” *Physical Review Applied*, vol. 8, Sept. 2017.
- [66] M. Hoshiyama, R. Kakigi, and O. Nagata, “Peripheral nerve conduction recorded by a micro gradiometer system (micro-SQUID) in humans,” *Neuroscience Letters*, vol. 272, pp. 199–202, Sept. 1999.
- [67] H. J. Mamin, M. H. Sherwood, M. Kim, C. T. Rettner, K. Ohno, D. D. Awschalom, and D. Rugar, “Multipulse Double-Quantum Magnetometry with Near-Surface Nitrogen-Vacancy Centers,” *Physical Review Letters*, vol. 113, July 2014.

- [68] P. Rembold, N. Oshnik, M. M. Müller, S. Montangero, T. Calarco, and E. Neu, “Introduction to quantum optimal control for quantum sensing with nitrogen-vacancy centers in diamond,” *AVS Quantum Science*, vol. 2, no. 2, p. 024701, 2020.
- [69] B. Bartels and F. Mintert, “Smooth optimal control with floquet theory,” *Physical Review A*, vol. 88, Nov 2013.
- [70] J. L. Webb, L. Troise, N. W. Hansen, J. Achard, O. Brinza, R. Staacke, M. Kischnick, J. Meijer, J.-F. Perrier, K. Berg-Sørensen, A. Huck, and U. L. Andersen, “Optimization of a diamond nitrogen vacancy centre magnetometer for sensing of biological signals,” *Frontiers in Physics*, vol. 8, p. 430, 2020.
- [71] R. Giri, F. Gorrini, C. Dorigoni, C. E. Avalos, M. Cazzanelli, S. Tambalo, and A. Bifone, “Coupled charge and spin dynamics in high-density ensembles of nitrogen-vacancy centers in diamond,” *Physical Review B*, vol. 98, p. 045401, July 2018.
- [72] J. Scheuer, X. Kong, R. S. Said, J. Chen, A. Kurz, L. Marseglia, J. Du, P. R. Hemmer, S. Montangero, T. Calarco, B. Naydenov, and F. Jelezko, “Precise ultra fast single qubit control using optimal control pulses,” *New Journal of Physics*, vol. 16, p. 093022, Sept. 2014.
- [73] G. T. Genov, Y. Ben-Shalom, F. Jelezko, A. Retzker, and N. Bar-Gill, “Efficient and robust signal sensing by sequences of adiabatic chirped pulses,” *Physical Review Research*, vol. 2, aug 2020.
- [74] J. F. Barry, M. J. Turner, J. M. Schloss, D. R. Glenn, Y. Song, M. D. Lukin, H. Park, and R. L. Walsworth, “Optical magnetic detection of single-neuron action potentials using quantum defects in diamond,” *Proceedings of the National Academy of Sciences*, vol. 113, pp. 14133–14138, Dec. 2016.
- [75] I. Fescenko, A. Jarmola, I. Savukov, P. Kehayias, J. Smits, J. Damron, N. Ristoff, N. Mosavian, and V. M. Acosta, “Diamond magnetometer enhanced by ferrite flux concentrators,” *Physical Review Research*, vol. 2, jun 2020.
- [76] Y. Xie, H. Yu, Y. Zhu, X. Qin, X. Rong, C.-K. Duan, and J. Du, “A hybrid magnetometer towards femtotesla sensitivity under ambient conditions,” *Science Bulletin*, vol. 66, pp. 127–132, jan 2021.
- [77] J. Johansson, P. Nation, and F. Nori, “QuTiP 2: A Python framework for the dynamics of open quantum systems,” *Computer Physics Communications*, vol. 184, pp. 1234–1240, Apr. 2013.

